Sound velocity cell for gas characterization

Petter Norli

Dissertation for the degree philosophiae doctor (PhD)

University of Bergen

August 2007

Preface

The present thesis is devoted to an experimental and theoretical investigation of ultrasonic measurement methods suggested for a precision sound velocity cell for pressurized natural gas.

The work has been carried out at Christian Michelsen Research AS (CMR), Bergen, Norway, in cooperation with the University of Bergen (UoB), Department of Physics and Technology, Bergen, Norway, as part of the 4-year strategic institute programme (SIP) *Ultrasonic technology for improved exploitation of oil and gas resources* (2003-2006), supported by the Research Council of Norway (NFR), Statoil ASA and Gassco AS.

I am very grateful to my supervisors, associate professor Magne Vestrheim, UoB, and senior scientist Dr. Per Lunde, CMR, for fruitful discussions and input throughout the work.

The staff at CMR have been most kind and helpful during the work. In particular Stig Heggstad and Reidar Bø are acknowledged for designing the main parts of the experimental setups; Remi A. Kippersund and Kjetil Daae Lohne are acknowledged for valuable advice and assistance on operation of the FEMP model, besides experimental measurements of transducer properties in air. I also wish to express my gratitude to Kjell-Eivind Frøysa for assistance on the Timres simulation program and various analyses.

The staff at the Mechanical Shop at UoB, especially Kåre Slettebakken, are highly acknowledged for manufacturing several parts of the experimental setups.

Finally I would like to thank my family and friends, in particular Audun Pedersen, Bjørn Einar Bjartnes, Per Gunnar Lunde and Jens Petter Stang for their genuine support throughout the work.

August 1, 2007, Petter Norli

List of papers

Papers A – D below constitute together with Chapters 1 – 5 the present PhD thesis. Additional papers written as part of the PhD work, but not included herein, are also listed in the following.

Paper A (PPA)

P. Norli, P. Lunde and M. Vestrheim, *Investigation of precision sound velocity measurement methods as reference for ultrasonic gas flow meters*, reformatted version of the paper originally published in: Proceedings of the 2005 IEEE Ultrasonics Symposium, Rotterdam, The Netherlands, September 18 – 21, 2005, pp. 1443 – 1447.

Paper B (PPB)

P. Norli and P. Lunde, *Diffraction correction for a piezoelectric ultrasonic gas transducer using finite element modelling*, reformatted version of the paper submitted, as of April 12 2007, to: IEEE Transactions on Ultrasonics, Ferroelectrics, and Frequency control.

Paper C (PPC)

P. Norli, *A two-way pulse echo method for a precision sound velocity measurement cell*, reformatted version of the paper submitted to: Applied acoustics. Accepted for publication, given some minor revisions, as of June 27, 2007.

Paper D (PPD)

P. Norli and P. Lunde, *A three-way pulse method for a precision sound velocity measurement cell*, reformatted version of the paper originally published in: Proceedings of the 2006 IEEE Ultrasonics Symposium, Vancouver, Canada, October 3 – 6, 2006, pp. 884 – 889.

P. Norli, P. Lunde and M. Vestrheim, *Methods for precision sound velocity measurements in pressure cells for gas characterization*, in Proceedings of the 27$^{\text{th}}$ Scandinavian Symposium on Physical Acoustics, Ustaoset, Norway, January 25 – 28, 2004.

P. Norli, *Comparison of three methods for precision sound velocity measurement of gases*, in Proceedings of the 28$^{\text{th}}$ Scandinavian Symposium on Physical Acoustics, Ustaoset, Norway, January 23 – 26, 2005.

P. Lunde, P. Norli, M. Vestrheim and R. A. Kippersund, *Precision sound velocity cell as reference for gas quality measurement in ultrasonic flow meters*, in Proceedings of the 30$^{\text{th}}$ Scandinavian Symposium on Physical Acoustics, Geilo, Norway, January 28 – 31, 2007.

Contents

List of Figures

List of Tables

Chapter 1

Introduction

1.1 Objective

The primary objective of this doctoral work is to establish a scientific basis for developing a high precision sound velocity cell for natural gases under high pressures. A candidate measurement method for such a cell, proposed in [61], should be investigated theoretically and experimentally, possibly alongside alternative candidate methods.

1.2 Background

The present background is based on [72]. Measurement of sound velocity in gases has been a field of considerable effort over several decades, with numerous applications in physics, metrology and industrial instrumentation. Examples can be found in e.g. [88, 30].

Sound velocity measurement has important perspectives in relation to international trading of natural gas. In many european countries, natural gas is sold on basis of energy content. The energy flow rate (the product of the gross calorific value (GCV) and the standard volume flow of the gas) is thus an important parameter in selling and buying gas. Although gas is sold on basis of mass [73, 74] in Norway (the product of the density and the actual volume flow of the gas), Norwegian companies have to address energy

measurements as well, as they trade with customers who count in terms of energy flow.

Energy and mass flow measurement of gas are today made using a volumetric flow meter (e.g. turbine, orifice plate or ultrasonic meter), combined with a separate measurement of the GCV and/or the density, respectively. The GCV can be measured in several ways, of which two common methods are: (1) use of one or several on line gas chromatographs (GC) combined with an equation of state (e.g. the AGA-8 equation [84]), or (2) use of a calorimeter. The density can also be measured in several ways. Two common methods are: (1) use of one or several on line gas chromatographs combined with an equation of state, (2) use of one or several densitometers.

The use and maintenance of GCs is work demanding and costly, and reducing the number of GCs in metering stations is a highly addressed topic these days, in relation to condition based maintenance. Other aspects of importance is the ability to detect drift in GC instruments, and operation outside of GC specifications.

Ultrasonic gas flow meters (USMs) offer a potential to further reduce the cost of energy and mass flow measurement, which may be of particular interest for monitoring and regulation purposes associated with gas commingling for export, for allocation metering, and as backup to GC analysis. Up to now, USMs have been used as volumetric flow meters.

However, such meters also provide measurement of the sound velocity of the gas. Research in recent years has shown that a measurement of the sound velocity in combination with other quantities, such as the temperature and pressure, can be used to calculate the GCV and density of high-pressure natural gas. Internationally, several companies and research groups have addressed these topics, cf. [55, 19, 20, 21] for an overview.

1.3 Motivation and problem statement

In order to use the USM as a mass and energy flow meter, documentation and traceability to national and international standards is needed for the uncertainty of the sound velocity measurement made by the USM, obtained by an independent and accurate method. This uncertainty is not known today, and no reference measurement methods are available to establish it. It has been shown that the uncertainty of the sound velocity measurement may be a significant contributor to the GCV and density measurement uncertainty [55, 20, 21].

There is thus need for a high-precision sound velocity measurement cell with known uncertainty, which can be used together with the USM in a laboratory measurement setup (for the same natural gas sample, at the same pressure, temperature, etc.), to check the accuracy of the sound velocity measured by the USM. To minimize uncertainty contributions due to possible dispersion effects in the gas, the sound velocity cell should operate in the frequency band of current USMs, 100 – 200 kHz. Tentative technical specifications have been outlined for the sound velocity cell in a feasibility study [61]; the measurement uncertainty of the sound velocity should be within $\pm(0.05 - 0.1)$ m/s $\rightarrow$ 100 – 200 ppm (at a 95% confidence level), over the pressure range 0 – 250 barg, and the temperature range 0 – 60 °C. The cell should preferably not involve any moving parts [61].

Such a measurement cell may also have other useful applications. One is the sound velocity correction in vibrating element densitometers, which are extensively used by oil and gas industry [61]. Another application may be related to improving the natural gas equation of state, virial coefficients etc. [61].

1.4 Thesis outline

Chapter 2 gives a brief account of existing sound velocity measurement cell methods, primarily based on literature surveys performed in a feasibility study for the precision

sound velocity cell [61], and paper [72] written as part of this doctoral work. More recent references are also included.

Chapter 3 is supplementing the theory briefly treated in papers A – D, and providing more information on some of the assumptions inherent in the work described in these papers. Three sound velocity measurement methods for gases have been investigated in this work, of which two are considered candidates for the precision sound velocity cell, the one proposed in [61] and one identified during the present work. Hence, emphasize is put on these two methods throughout Chapters 3 to 5.

The development process, from initial to final design, of a prototype sound velocity cell for the candidate methods is briefly outlined in Chapter 4. Included are experimental details and challenges faced en route, which needed be resolved to get the candidate measurement methods working properly.

Concluding remarks on the results as a whole are given in Chapter 5. In addition, measurement results for the prototype sound velocity cell obtained beyond this work are briefly reported. In these, argon was used as test gas, for which a much more accurate sound velocity model exists for comparison purposes.

Paper A, hereinafter referred to as 'PPA', concerns the two-distance method (2DM), which was used in the initial phase of this work to gain experience on transient methods for sound velocity measurements. Also, some common aspects with the two proposed candidate methods [PPC, PPD] were investigated.

Due to the high impact diffraction correction has on the measurement uncertainty of the the two candidate methods, transducer diffraction effects were investigated by a finite element model (FEM) for non-uniformly vibrating transducers [56, 58, 47, 48, 49], such as those employed in this work. The effort is described in Paper B, which will be referred

to as 'PPB'.

Paper C, referred to as 'PPC', concerns one of the two candidate measurement methods, namely the two-way pulse echo method. The method is described, including theory, experimental realization and associated sound velocity measurement results. These were obtained using atmospheric air at room temperature as test gas.

The other candidate method, the three-way pulse method, is described in Paper D, abbreviated 'PPD'. The paper features modelling and experimental realization of the method, and associated sound velocity measurement results, obtained using atmospheric air at room temperature as test gas.

Chapter 2

Measurement methods

The scope of this chapter is to give a brief account of the existing sound velocity measurement methods that have been considered possible candidates for the precision sound velocity cell for natural gas under pressure. The overview is confined to methods intended for gas under pressure (or in some cases liquids), contained in a closed volume/cavity. The methods included have been selected as they were considered more relevant for the technical cell specifications (Sec. 1.3) than those excluded.

Ongoing work at CMR [61, 72] and elsewhere [42, 13] aims to develop a high-precision sound velocity measurement cell for gas under pressure. A feasibility study for this purpose was carried out at CMR in 1998 [61], including a review of available literature on existing methods with respect to their potentials for use in the present application. The literature on the topic appeared to be rather extensive. As an update of the literature survey in [61], a more recent survey was executed in this work [72]. The following overview represents a synthesis of [61] and [72], but more recent references are also included. Focus is put on the methods with most promising potential for performing according to the cell specifications stated in Sec. 1.3.

2.1 Classification of methods

Sound velocity measurement methods for gases may be divided in two categories [88]: *resonator methods* and *transient methods*, comprising the sub-categories below [61]

1. Resonator methods
    - Cylindrical resonators
        - Variable length
        - Fixed length
            - High-frequency / low-frequency
            - Single transducer / 2 transducers
    - Spherical resonators
    - Annular resonators
2. Transient methods
    - Single-pulse methods
        - Direct propagation, fixed length
        - Direct propagation or pulse echo, variable length
        - Pulse echo, fixed length
        - Direct propagation & reflection, fixed length
    - Double-pulse methods
        - Pulse echo with 2 reflectors, fixed length

2.2 Resonator methods

Resonator methods date back to 1925, when Pierce [76] invented a variable length cylindrical resonator, and used it with air and CO_2 at atmospheric pressure and 0 °C. The cell was operated in the frequency range 1 kHz – 1.5 MHz, and a measurement uncertainty of 300 – 900 ppm was claimed [76]. Resonator methods are sometimes referred to

as *steady-state methods* [88], as they involve a constant wave source to excite standing waves inside the cavity. Their measurement principle can be described, very simplified, as follows: Standing waves occur in a cavity whenever an integer number of half the acoustic wavelength, $\lambda/2$, equals some dimension of the enclosure, e.g. the length if the cavity is cylindrical, and the gas-wall interface reflection coefficient is nearly unity. Now at a known resonance frequency f, the sound velocity may be obtained from $c = f\lambda$ at the fundamental mode of resonance. The resonator cavities are usually cylindrical or spherical, but also annular cavities have been used [61].

Such methods perform best when the walls of the cavity reflect the sound efficiently [88, p. 179], which is often the case when the measurement medium is a gas at low or moderate pressure. In this range they have successfully been used for gases, cf. e.g. [67, 78]. At elevated pressures however, say beyond 100 bar [88], the characteristic acoustic impedance of the gas may become a significant fraction of that of the wall, which increases the coupling of the gas and shell motion, and the performance deteriorates accordingly. Confer [88, p. 179] for details on the different working principles of the various resonator methods.

2.2.1 Cylindrical resonators

Cylindrical resonators of variable length

Some 40 literature references have been identified in this category [61, 72], and selected ones are given in Table 2.1. Measurement principle examples of such resonator methods may be found for the low-frequency and high-frequency range in [78, 72] and [22, 23], respectively.

Variable length cylindrical resonators have proved high measurement accuracy; Quinn et al. (1976) [78] quoted a measurement uncertainty of ±15 ppm using argon at 0.3 – 2 bar and 0 °C as measurement medium. The cell was however operated in the low-frequency range, i.e. at 5.6 kHz, which is well below the currently specified frequency range, 100 – 200 kHz. Zhang et al. (2001) [102], Duan et al. (1997) [14], Sun et al. (1997) [85] and Zhu

Table 2.1: Selected literature references on variable length resonators.

Reference	Year	Pressure-range [bar]	Temp.-range [°C]	Frequency [kHz]	Claimed-uncertainty [ppm]
Duan et al. [14]	1997	0.6 – 2.8	0 – 60	156	±100
Sivaraman et al. [80]	1986	14 – 275	-80 – 150	500 – 2500	100
Quinn et al. [78]	1976	0.3 – 2	0	5.6	±15
Blend [8]	1969	1.013	-20 – 60	1 – 1000	100
Lestz [53]	1963	1.013	room temp.	2.4 – 4.3	< 500
Van Itterbeek et al. [90]	1959	0.3 – 2	-	500	±500
Greenspan et al. [28]	1953	0.088	31	11000	-
Hubbard [33]	1932	1.013	22 – 24	400 – 700	-
Pierce [76]	1925	1.013	0	1 – 1500	300 – 900

et al. (1993) [103] operated within our specified frequency range, i.e. at 156 kHz, however claiming a measurement uncertainty of ±500 ppm [102], which is more than twofold the tentative specified measurement uncertainty (Sec. 1.3).

In the feasibility study [61], it was pointed out that the measurement cell should preferably not involve moving parts; therefore, a variable length resonator was considered a less relevant method for the present application than some of those listed below [61].

Cylindrical resonators of fixed length

Some 30 references have been identified in this category [61, 72], of which the most relevant are listed in Table 2.2. Examples of measurement principles for such methods may be found in e.g. [101] and [88, p. 206].

Table 2.2: Selected literature references on cylindrical fixed length resonators.

Reference	Year	Pressure-range [bar]	Temp.-range [°C]	Frequency [kHz]	Claimed-uncertainty [ppm]
Hurly [36]	2003	<16	-73.15 – 186.85	1 – 8	±100
Hurly [35]	2002	15	-73 – 152	-	±200
Benedetto et al. [7]	1996	0.005 – 5	0.01	0.1 – 15	100
Giacobbe [24]	1993	1	0 & 25	≤20	±1500
Younglove et al. [100]	1992	<140	-163 – 27	10 – 70	<500
Younglove et al. [101]	1980	0.3 – 15	-193 – 77	16 – 19	300
El-Hakeem [15]	1965	170	0 & 21	2.8 – 4.5	±200
Smith et al. [81]	1963	1.013	31	0.09 – 1.5	100
Hubbard et al. [34]	1939	-	-	-	-

A fixed length resonator, promising for our purpose appeared to be [72, 61] the one used by Younglove and coworkers [101], which was operated below 70 kHz, with a quoted experimental uncertainty in the range 200 – 500 ppm. Hence, significant further development would be necessary to achieve a measurement uncertainty below 200 ppm, as specified. Also, it was concluded [61] that a more solid documentation of the claimed measurement uncertainty would be needed to pursue the development of a such method for the sound velocity cell. Partly for these reasons, this method was not proposed as a candidate method [61].

As seen from Table 2.2, Hurly [36, 35] reported a measurement uncertainty that meets the tentative technical specifications, which however applies at considerably lower pressures than needed. The degraded performance of the cell used by Younglove et al., when going from about 15 bar to 140 bar [101, 100] may indicate that a significantly poorer measurement accuracy be expected for such methods at elevated pressures up to 250 bar. Since no references were identified that could demonstrate measurement uncertainty near our requirements, such methods were not recognized to be among the most promising candidates for the sound velocity cell.

2.2.2 Spherical resonators

More than 60 literature references were identified on spherical resonators, and selected ones are given in Table 2.3. Obviously, very high measurement accuracy may be achieved using such methods (Table 2.3, column 6). For example, Moldover and his coworkers [67] achieved (1988) an impressive measurement uncertainty of about 1 ppm over the pressure range 0.025 – 5 bar, operating in the frequency range 2.5 – 9.5 kHz. Confer [67] for a description of the measurement principle of such methods.

To achieve such an outstanding measurement accuracy, a number of effects need be corrected [67, 66], such as

1. frequency shift caused by thermal losses in a boundary layer near the resonator wall;

2. frequency shift due to the coupling of the elastic shell motion and gas motion;

3. frequency shift due to imperfect resonator geometry;

4. frequency shift due to viscous and thermal attenuation in the gas volume, etc.

Spherical resonator methods perform best at sound velocity measurements in the low-frequency region, because here the normal modes of the cavity are resolved from each other [88, p. 197]. Also, wide-bandwidth transducers are available for excitation and detection of such modes.

For our application, the cell used by Goodwin et al. [27] (cf. Table 2.3) seems very promising, yielding a measurement uncertainty of 20 ppm up to pressures of 420 bar over the temperature range -73 – 177 °C. It is however suspected that the cell was operated in the audio frequency range; if designing such a cell for the relevant frequency range (100 – 200 kHz) for the 5 lower radial modes, which is common when high measurement accuracy is aimed at, the inner diameter would be about 1.1 cm [61]. This would lead to major difficulties regarding the transducer design and corrections [67] necessary to obtaining such high measurement accuracy [61]. Therefore, such methods does not seem to be among the most promising for the application in question.

Table 2.3: Selected literature references on spherical resonators.

Reference	**Year**	**Pressure-range [bar]**	**Temp.-range [°C]**	**Frequency [kHz]**	**Claimed-uncertainty [ppm]**
He et al. [29]	2002	<2	$20-50$	-	± 37
Estela-Uribe et al. [16]	2000	$0.25-14.2$	$-103-127$	-	± 5
Estrada-Alexanders et al. [17]	1995	190	$-163-177$	-	$\pm(10-70)$
Goodwin et al. [27]	1995	<420	$-73-177$	-	20
Trusler et al. [89]	1992	<100	$2-102$	$7.5-22$	20
Colgate [10]	1992	$0.5-6$	$25-175$	-	$\pm(2-50)$
Moldover et al. [67]	1988	$0.025-5$	0	$2.5-9.5$	1
Mehl et al. [64]	1981	$1-10$	$0-100$	$4-13$	± 30
Keolian et al. [43]	1978	-	-	-	-

2.2.3 Annular resonators

The identified literature on such methods seems to be rather sparse, as only two were identified in [61]. Jarvis et al. [40] employed in 1996 an annular cell pressurized from 1 to 50 bar, operating in the frequency range 1 – 10 kHz, and achieved a measurement uncertainty of 500 ppm. Such methods work best at relatively low frequencies, and moreover, their relatively low volume to surface ratio (compared to cylindrical and spherical resonators), which should be as high as possible, led to a rejection of such methods as candidates for the sound velocity cell [72].

2.3 Transient methods

Some twenty references were identified on transient methods, and selected ones, especially relevant for our application, are given in Table 2.4. Transient methods employ, as the name implies, a transient sound field as means to characterize the gas medium. The sound velocity is basically determined from the measurement of a pulse transit time, which may be measured with high precision, over a known distance in the medium [88, p. 215]. Such methods are quite versatile with respect to frequency and pressure, but perform best for dense fluids such as liquids. Consider Table 2.4 that outlines some selected literature references on such methods, indicating the elevated pressures and frequencies used. The reported experimental uncertainty typically exceeds 1000 ppm, which is well beyond the target measurement uncertainty of 100 – 200 ppm.

Table 2.4: Selected literature references on transient methods.

Reference	Year	Pressure-range [bar]	Temp.-range [°C]	Frequency [MHz]	Claimed-uncertainty [ppm]
Ball et al. [3]	2002	<700	62 – 129	5	-
Suzuki et al. [86]	2000	-	-	-	-
Lunde et al. [61]	1998	-	-	-	-
Barreau et al. [4]	1997	400 – 1000	20 – 100	3	±500
Daridon et al. [12]	1994	<1000	-	1 – 10	<2000
Dorr [13]	1990	-	-	-	-
Kortbeek et al. [50]	1986	<10000	-125 – 25	9.5 – 10.5	200
Liebenberg et al. [54]	1974	700 – 13000	25	10 – 30	2000 – 3000
Voronov et al. [94]	1969	<4000	25 – 175	1 – 10	3000

Kortbeek et al. [50] were the only identified reference claiming a measurement uncertainty in line with our target specifications, cf. Table 2.4. The method was briefly evaluated in the feasibility study [61], where a direct dimensional scaling by a factor 75 was considered to reach an operating frequency of 150 kHz. This would lead to inner cell dimensions (diameter x length) of 1.2 x 3.75 m, if the same proportions were to be used, giving an unrealistically large cell. Using a smaller cell could be an option, but then it would be necessary to investigate how the measurement uncertainty would be affected. Also, a more solid documentation on the measurement uncertainty than provided in [50] would be needed.

A candidate measurement method for the precision sound velocity cell was proposed by Lunde and Vestrheim in the feasibility study [61], here referred to as the *three-way pulse method* (3PM). The method may be classified as a "single-pulse direct propagation and reflection, fixed length", with similarities to a method that has been applied for solids [96, 79]. The 3PM has—to the author's knowledge—never been investigated experimentally prior to this PhD work, except for some undocumented work by the CMR group. A theoretical analysis of the 3PM [61] indicated a promising potential with respect to the tentative technical specifications (Sec. 1.3). Therefore, the method has in the present work been investigated as a candidate for the precision sound velocity cell [71].

Another possible candidate method for the precision sound velocity cell was identified in a patent article [86]. Literature surveys have been performed to check if the method has been realized experimentally, and whether measurement results exist that may indicate the measurement accuracy potential. The search did not identify any such. This method [86] may be classified as a "double-pulse method, pulse echo with two reflectors, fixed length". A bi-directional measurement configuration is used, where a pair of acoustic transducers both act as transmitter and receiver. The method described in [86] has in this work been significantly modified, and shall be referred to as the *two-way pulse echo method* (2PEM). As will emerge in this thesis, the method has several similarities with

the 3PM. A theoretical investigation of the 2PEM indicated that it was as promising as the 3PM for the precision sound velocity cell. It was thus decided to further investigate its potential.

From the above considerations, the 3PM and 2PEM both seemed promising for realization in a precision sound velocity cell for gas under pressure. As the same measurement setup presumably could be used for both methods (except for the electronic circuitry), it was decided to further investigate the potential for realizing the two methods in a precision sound velocity cell, theoretically and experimentally.

Chapter 3

Theory

The present chapter is devoted to supplement the sometimes brief theory in papers A – D, and provide the reader with a backdrop and basis for the remaining chapters. Emphasize is put on the candidate sound velocity measurement methods, as these are intended for the sound velocity cell. Section 3.1 defines a few basic sound velocity concepts. The three sound velocity measurement methods used in the current work are briefly treated in Secs. 3.2 – 3.4 (as they are more thoroughly treated in papers A, C and D). Section 3.5 concerns the evaluation of the time precision of the zero crossing time detection method used throughout the work. In Sec. 3.6, the correction terms considered relevant for the candidate methods are treated. Note that 'Δt' and 't^{corr}' are common notations for transit time difference and correction terms, respectively, in the three sound velocity measurement methods, but their content differs between the methods. Section 3.7 describes the sound velocity model for humid air, used for comparison with the measurement results throughout the work.

3.1 Sound velocity concepts

In the present context, we must distinguish three different concepts of sound velocity

1. The signal velocity, c', which is the velocity of the leading edge of a pulse [88, p. 220];

2. The phase velocity, c, which is the velocity at which points of equal phase in a mono frequency wave propagates [69, p. 477];

3. The group velocity, c_g, which is the propagation velocity of the "centre of gravity" for a group of waves with somewhat different frequencies [69, p. 477]. Under certain conditions it is related to the phase velocity by $c_g = c + \omega_0(\partial c/\partial\omega)_{\omega_0}$ [88], where ω and ω_0 are the angular frequency and carrier angular frequency, respectively.

To get a good measure of the phase velocity c, the measurement subject in this work, corresponding periods in the centre part of the received pulse should be matched to the transmitted pulse [88], which hence was done.

3.2 The two-distance method

The two-distance method (2DM) is a widely used method, cf. e.g. [26, 9, 87], with potential of high measurement accuracy. As it involves moving parts, however, it was not considered a candidate for the precision sound velocity cell, cf. Sec. 1.3. The theory of the 2DM is described in [PPA], but the measurement principle will for convenience be summarized here.

Confer Fig. 3.1 which illustrates the measurement configuration. A pair of coaxial acoustic transducers, separated by the distance L_1, are aligned with parallel front faces. The function generator emits an electrical RF burst pulse, which is converted into mechanical vibrations by the source transducer. A resulting acoustical pulse ① is then transmitted through a flow free gas medium—exciting mechanical vibrations in the receiving transducer. The receiver converts these vibrations to an electrical signal, which is amplified, filtered and stored in an oscilloscope. The transit time of ① from generator to oscilloscope, denoted t_1, is measured in an appropriate way [PPA].

The transducer separation is within about five seconds increased by a precision positioning stage, so that the similar measurement process can be repeated at distance L_2, so as

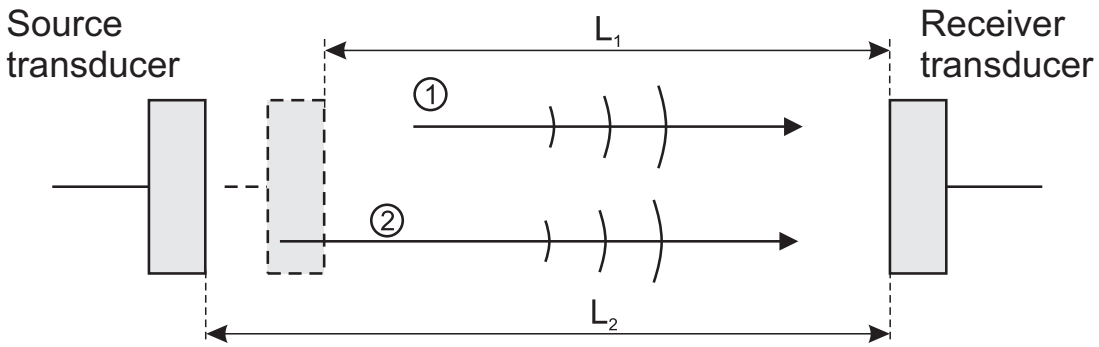

Figure 3.1: Sketch of the measurement principle of the two-distance method, where ① and ② denote transmitted acoustic pulses at distances L_1 and L_2, respectively.

to obtain the transit time associated with ②, t_2.

It can be shown [PPA] that the sound velocity c is given as

$$c = \frac{\Delta L}{\Delta t - t^{corr}}, \tag{3.1}$$

where

$$\Delta L \equiv L_2 - L_1, \tag{3.2}$$

$$\Delta t \equiv t_2 - t_1, \tag{3.3}$$

and

$$t^{corr} \equiv t_2^{corr} - t_1^{corr}. \tag{3.4}$$

The quantities t_1^{corr} and t_2^{corr}, are due to corrections associated with the propagation of ① and ②, respectively. In the present work these were confined to account for transducer diffraction effects [PPA]. The value of ΔL was set at and controlled by the positioning stage, and Δt was measured using zero crossing time detection, cf. Sec. 3.5.

A major advantage with this method is the cancelling of the transmitting and receiving delay time of the electronics and transducers [PPA], given that the measurement system is stationary throughout the measurement. Another advantage is that the distance measure-

ment ΔL is relative, which typically may be performed with high accuracy [61]. In this context, the presence of moving parts is however considered a disadvantage, and should preferably be avoided in the sound velocity cell [61]. The sound velocity measurement results using the 2DM are reported in [PPA].

3.3 The two-way pulse echo method

The 2PEM, based on the method described in [86], is one of the two candidate measurement methods, primarily described in [PPC]. For convenience, the measurement principle is briefly anticipated here.

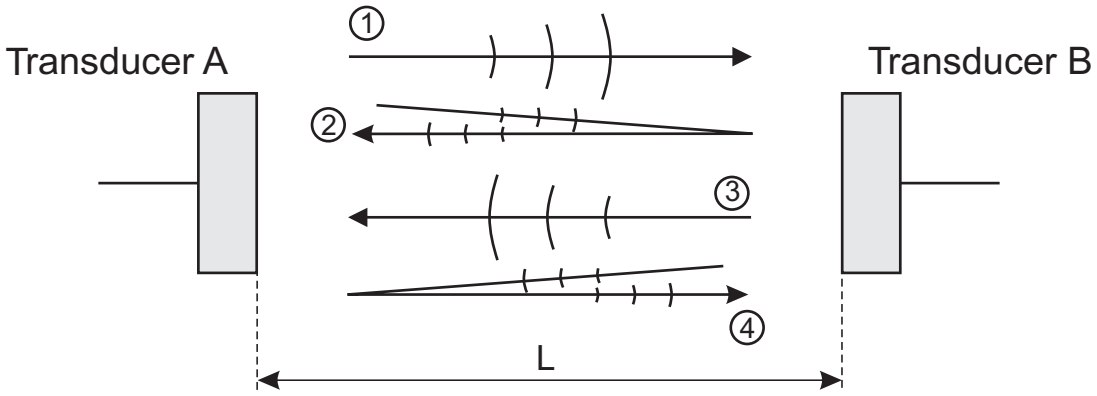

Figure 3.2: The measurement principle of the *two-way pulse echo method*, where ① and ③ denote the pulses, and ② and ④ denote the echoes utilized for transit time measurement.

Confer Fig. 3.2, which illustrates the measurement configuration. A pair of coaxial acoustic transducers A and B, abbreviated TrA and TrB, are separated axially by the distance L in a measurement medium assumed to be gaseous. Now, an electrical RF burst pulse is generated by the function generator and converted to mechanical vibrations by TrA. A resulting acoustical pulse ① is transmitted across distance L, and excites mechanical vibrations in the receiving transducer TrB. The vibrations are converted by TrB to an electrical signal which is amplified, filtered and stored in an oscilloscope. The transit time due to the propagation of pulse ① is measured in some appropriate way [PPC], and is de-

noted t_1. A part of pulse ①, denoted ②, is reflected at the front face of TrB—propagating back to TrA to be received, and the associated transit time t_2 is measured in a suitable manner [PPC].

At the subsequent trig signal, the process is repeated from the opposite side with TrB acting as source, so as to measure the transit times t_3 and t_4 (in the same manner as with t_1 and t_2) from pulse ③ and echo ④, respectively.

The feasibility study for the precision sound velocity cell [61] identified several effects for the 3PM which possibly should be corrected. These are also deemed relevant in the current method: (1) due to the finite source extension, measurement signals ① to ④ will not propagate as plane waves, a phenomenon which may be referred to as transducer diffraction; (2) thermal and viscous boundary layers are set up in thin layers adjacent to the transducer front face when a sound wave impinges on it [88, p. 40].[1] Hence, the fluid properties within this layer change, yielding a phase shift of echoes ② and ④ upon reflection; (3) upon reflection, delayed (and reduced) echoes from the transducer interior will interfere with ② and ④, resulting in an undesired phase shift. The transit time correction term t^{corr} is dedicated to account for these effects.

It may be shown [PPC] that the sound velocity c is given by

$$c = \frac{2K_T L_0}{\Delta t - t^{corr}}, \tag{3.5}$$

where $K_T = L/L_0$ is the thermal expansion coefficient and L_0 is the reference transducer separation (measured at a reference temperature) [PPC]. A linear relationship has been assumed for K_T [61], i.e.

$$K_T = 1 + \alpha(\overline{T} - T_0), \tag{3.6}$$

where α is the coefficient of thermal expansion for the material in question, and $\overline{T}$ is

[1] in case of normal incidence to the transducer front, only a thermal boundary layer will be generated [88, p. 40].

the temperature average during measurement, defined in Sec. 4.2.2. Pressure expansion/contraction was not considered relevant in this work, as the measurements were carried out in atmospheric air [PPC, PPD]. Furthermore, we have

$$\Delta t \equiv t_2 - t_1 + t_4 - t_3, \tag{3.7}$$

and

$$t^{corr} \equiv t_2^{corr} - t_1^{corr} + t_4^{corr} - t_3^{corr}, \tag{3.8}$$

where subscripts 1 to 4 refer to the respective signals, and the content of t^{corr} is described in [PPC].

Also in this method, the time delays of the electronics and transducers cancel out [PPC], which is a major advantage. A disadvantage compared to the 2DM however is the increased impact of t^{corr} [PPA, PPC], and presumably a higher sensitivity to angular misalignment of the transducer fronts.

3.4 The three-way pulse method

The 3PM is the second of the two candidate measurement methods, proposed for the precision sound velocity cell in [61]. The measurement configuration is illustrated in Fig. 3.3, showing two acoustic transducers separated axially by the distance L in a gaseous fluid medium. An electrical RF burst pulse is output from the function generator, then converted to an acoustical pulse ① by source transducer A, abbreviated *TrA*. Pulse ① propagates across the distance L—to the receiving transducer B, abbreviated *TrB*. TrB is as a result set up in mechanical vibrations, which it converts to an electrical signal that is amplified, filtered and stored in an oscilloscope. The transit time elapsing as ① travels from generator to oscilloscope, t_1, is measured in an appropriate manner. In this work, zero crossing time detection was used, cf. [PPD] and Sec. 3.5.

Due to the reflection of ① at the front face of TrB, echo ② arises—traveling back to TrA, upon whose front face it is reflected again—and travels forth to TrB. This converts the mechanical vibrations into an electrical signal that is amplified, filtered and stored in an oscilloscope. The transit time associated with ②, t_2, is measured in the same manner as t_1.

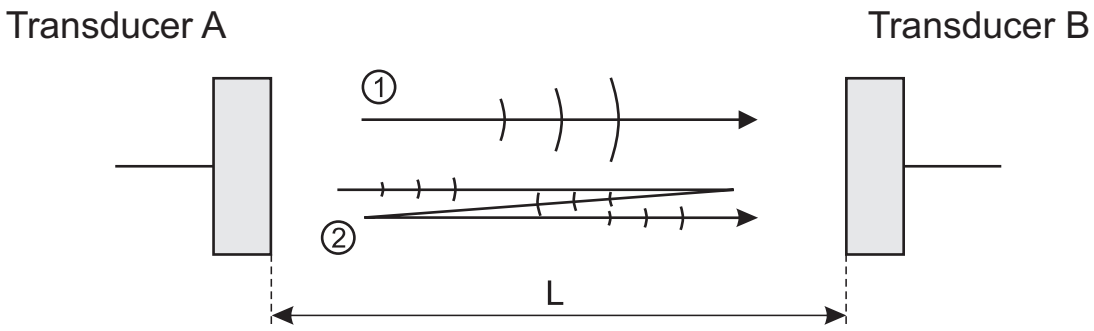

Figure 3.3: The measurement principle of the three-way pulse method, where ① and ② denote measurement pulse and echo, respectively.

As for the 2PEM described in the previous section, effects of transducer diffraction affect the propagation of ①, and consequently t_1. As for echo ②, it is affected by transducer diffraction, thermal and viscous boundary layers upon reflection, and interference with internal transducer reflections upon reflection [61], which consequently affect t_2. The correction term t^{corr} is also in this method dedicated to account for the perturbations in t_1 and t_2 due to such effects.

It may be shown [61, PPD] that the sound velocity c is given by

$$c = \frac{2K_T L_0}{\Delta t - t^{corr}}, \tag{3.9}$$

where K_T and L_0 are defined in Sec. 3.3,

$$\Delta t \equiv t_2 - t_1, \tag{3.10}$$

and

$$t^{corr} \equiv t_2^{corr} - t_1^{corr}. \tag{3.11}$$

The findings of the present work indicate that diffraction correction predominates the correction t^{corr} [PPD]; its contents is described in [PPD].

Also in this method the time delays of the electronics and transducers cancel out under certain assumptions [61, PPD], which is a major advantage. However, as for the 2PEM, a disadvantage connected to the present method is the increased influence of t^{corr}, compared to the 2DM—a quantity that is challenging to evaluate. Also, the 3PM is presumably more sensitive to angular misalignment of the transducer front faces than the 2DM.

3.5 Zero crossing time detection

To identify corresponding burst period in the transmitted and received measurement signals for the 2PEM and 3PM, the methods described in [PPC] and [PPD] were used, respectively. These methods involve zero crossing time detection through (the center part of) the burst pulse, combined with linear interpolation. This time detection approach, which was suggested for the 3PM in the feasibility study [61], is described in more detail in [92, Sec. 8.3.3].

To evaluate the zero crossing time detection uncertainty, the statistically based simulation program *Timres* [18] was applied. Both maximum and standard deviation between sampled and true zero crossing times are calculated, based on a large population of burst trials. Input parameters are frequency, vertical bit resolution, sampling frequency f_s, signal frequency variation, number of zero crossings, etc.

The transducers applied in the present work were operated at 218 kHz (cf. Sec. 4.2.1), around which frequency the simulations were carried out. The number of burst periods were set to 35, as experiments revealed this to be sufficient for Δt to become essentially

stationary for transit time measurements, for both candidate methods. The vertical bit resolution was varied between 8 and 9 bits, as the effective resolution has been estimated for the current oscilloscope [PPA] to about 8.4.[2] The frequency variation was assumed to be linear, with a maximum value of 100 ppm,[3] and the number of burst trials was set to 10^4.

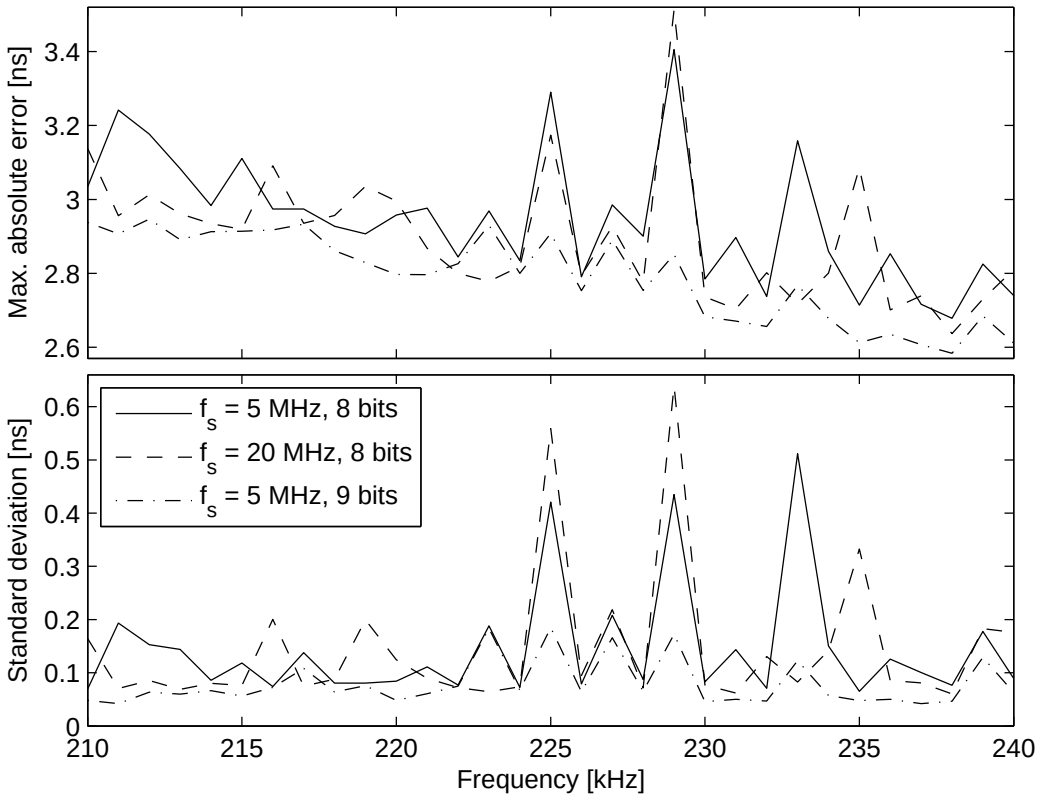

Figure 3.4: Upper subplot: maximum deviation between true and detected zero crossing time. Lower subplot: standard deviation between true and detected zero crossing. The results are based on 10^4 burst trials and a burst pulse of 35 periods.

Figure 3.4 displays simulated maximum and standard deviation between detected and true zero crossing, in upper and lower subplot, respectively. The results will here merely be used to indicate the relevant sampling requirements for the transit time detection. As

[2]the nominal vertical bit resolution is stated to 12.

[3]the HP33120 function generator will probably perform much better than this over the short measurement duration of about 1 s.

several burst pulses are averaged in the candidate methods [PPC, PPD], we are primarily interested in the standard deviation of the time detection. Around 218 kHz, the simulated standard deviation is within 0.2 ns (giving approximately 0.2 ppm uncertainty in Δt for both candidate methods [PPC, PPD]) for $f_s = 5$ MHz and 8 bits of vertical resolution. This is insignificant compared to the predominating uncertainty contributions of the candidate methods, cf. [PPC, PPD]. The result thus indicates that $f_s = 5$ MHz and 8 bits of vertical resolution suffices.

Figure 3.4 shows moreover that little is gained by increasing f_s from 5 to 20 MHz. In fact, at some frequencies the standard deviation of the time detection increases for $f_s = 20$ MHz. However, increasing the vertical resolution from 8 to 9 bits significantly reduces the standard deviation of the simulated time detection uncertainty.

3.6 Correction terms

The error effects considered relevant in the two candidate measurement methods were (1) transducer diffraction/beam spreading, (2) phase shift due to thermal and viscous boundary layers at the transducer front upon reflection, and (3) interference with echoes from the transducer interior upon reflection. However, as emerging in Sec. 3.6.3, the latter effect could, for the present transducer [63], frequency and gas conditions in question [PPC, PPD], be neglected in this work. To correct transducer diffraction and thermal and viscous boundary layer effects, the correction terms t_i^{corr} have been introduced;

$$t_i^{corr} \equiv t_i^{dif} + t_i^{tv}, \qquad \begin{cases} i = 1, \ldots, 4 & \text{[2PEM]}, \\ i = 1, 2 & \text{[3PM]}, \end{cases} \tag{3.12}$$

where i denotes respective pulse or echo, cf. Figs. 3.2 and 3.3 for the 2PEM and 3PM, respectively. The terms at the righthand side are transit time corrections due to transducer diffraction and thermal and viscous boundary layers, respectively. However, as effects of thermal and viscous boundary layers are associated with reflection at the transducer front,

t_1^{tv} and t_3^{tv} are omitted.

3.6.1 Diffraction correction

Background

In early works on ultrasonic absorption measurements it was discovered that distance-dependent error effects due to divergence of the source beam, or diffraction, was to be corrected if highly accurate absorption measurements were attempted, c.f. e.g. [77]. Consider Fig. 3.5, which displays an idealized scenario of the *transducer diffraction effects* to be corrected.

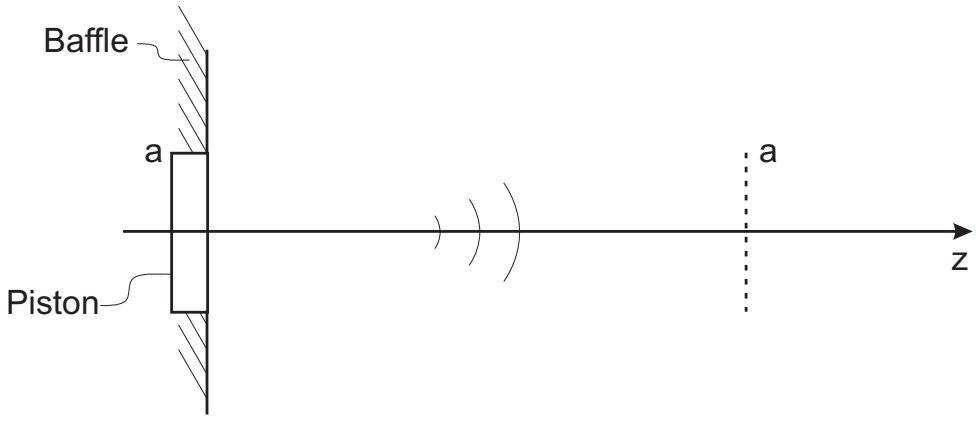

Figure 3.5: Illustration of transducer diffraction effects. The piston source is seated in an infinite rigid planar baffle, and transmits sound to a coaxial receiver plane (indicated by the dotted line). The sound waves eventually spread out spatially and leads a plane wave transmitted with same initial phase.

A planar sound source of radius a, seated in an infinite rigid planar baffle and vibrating with uniform velocity across the aperture, transmits sound through a fluid to a plane coaxial receiver of same radius as the source. Now, due to the finite aperture of the source, the sound will spread out geometrically (Fig. 3.5), and thus deviate in phase and magnitude relative to a plane wave. Upon detection at the receiver, the wave front arrives at different times along the radial direction, which also affects the magnitude and phase of the detected signal.

A diffraction correction function has been defined [44] for this idealized case as

$$H^{dif} \equiv \frac{\langle p \rangle_A}{p_{pl}}, \tag{3.13}$$

where $\langle p \rangle_A$ is the sound pressure in the fluid, averaged over the receiver with area $A = \pi a^2$, in absence of the receiver; $p_{pl} = \rho c v_0 e^{\imath(\omega t - kz)}$ is the plane wave pressure, where $\imath \equiv \sqrt{-1}$, ρ is the fluid density, v_0 is the amplitude of the normal velocity on the piston surface, ω is the angular frequency, and $k = \omega/c = 2\pi/\lambda$, where λ is the acoustic wave length. The harmonic time variation $e^{\imath\omega t}$ is henceforth omitted.

The current definition of H^{dif} implies that the source and receiver are taken to be planes with no axial extension, omitting any sound contribution that would take place at the sides and back of a realistic transducer. In practice, diffraction correction depends on a number of parameters [58], such as: sound velocity, frequency, transducer separation, source vibration pattern, which in turn depend on temperature and pressure. The transducer properties are thus highly important, and were therefore investigated in [PPB], cf. also p. 29.

The plane piston diffraction correction model

For the idealized source-receiver arrangement described in previous subsection, where the source and receiver are represented by circular disks with no axial extension, the following solution of Eq. (3.13) has been given [97, 44, 45]

$$H^{dif} = 1 - \frac{4}{\pi} \int_0^{\pi/2} e^{\imath kz\left[1-\sqrt{1+\left(\frac{2a}{z}\right)^2 \cos^2\theta}\right]} \sin^2\theta \, \mathrm{d}\theta, \tag{3.14}$$

where θ is an integration variable. The time domain diffraction correction is obtained by

$$t^{dif} = \frac{\angle H^{dif}}{\omega_0}, \tag{3.15}$$

given $\angle H^{dif}$ in radians. An example of a solution of Eqs. (3.14) and (3.15) may be found in e.g. [PPA, Fig. 6.4]. The calculation approach and value for t_i^{dif} in Eq. (3.12) for the 2PEM and 3PM may be found in [PPC] and [PPD], respectively.

Transducer modeling

The plane piston diffraction correction model accounts for transducer diffraction associated with an idealized source-receiver pair (cf. Fig. 3.5), where the source and receiver have no axial extension, and the source vibrates with uniform velocity across its planar aperture [97, 44, 45]. To model the sound field from the *Massa E-188/220* ultrasonic air transducer used here [63], and investigate how representative the plane piston diffraction correction model is for this transducer, a finite element diffraction correction model, specially designed for piezoelectric transducers (*FEMP*) [57, 56, 58, 47, 48, 49] has been utilized.

This effort is described in [PPB], but to indicate the sound pressure field produced by the Massa transducer, which is also relevant in the following subsection, a 2D sound pressure plot is presented in Fig. 3.6. It is seen that the source beam is relatively narrow (compared to alternative air transducers operating around the same frequency), and also, at a receiver distance of 151 mm the receiver is well covered by the beam.

The findings in Paper B actually indicated that the plane piston diffraction correction model may be applied to the Massa transducer around the operational frequency of 218 kHz, for a sound velocity of 340 m/s, and with the receiver located outside the nearfield, with little error. This was so in spite of the fact that the vibration pattern of the Massa transducer (at 218 kHz) proved very disparate from the uniform plane piston vibration pattern.

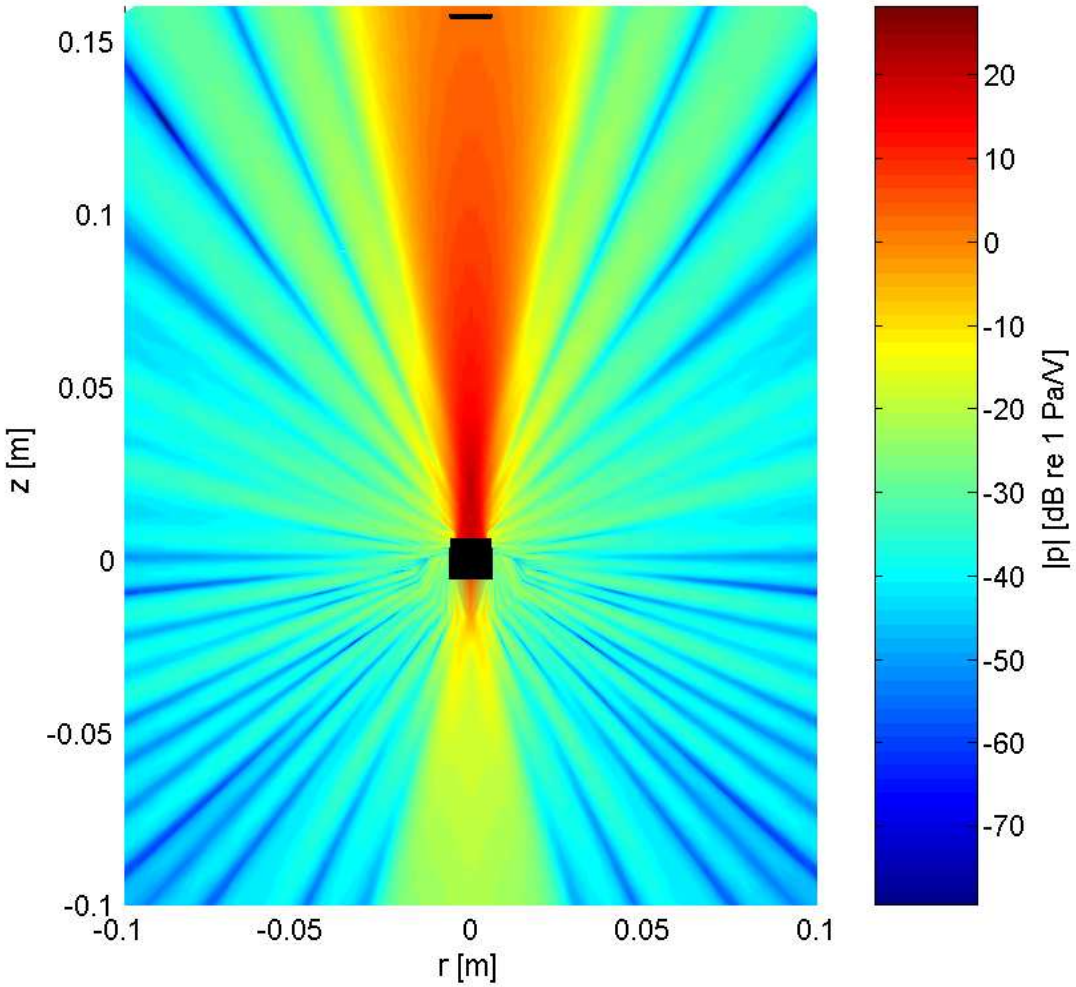

Figure 3.6: The pressure field calculated by FEMP for the Massa transducer at a frequency of 218 kHz, surrounded by atmospheric air at room temperature. The receiver front is also indicated (black line) at 151 mm distance from the source, as in the prototype sound velocity cell. Note that the transducer holders present in the prototype cell are not accounted for.

Transducer diffraction in pulse echo mode

Paper B concerned diffraction correction for the Massa transducer, for distances relevant in the precision sound velocity cell [61]. However, the problem of diffraction correction related to pulse echo mode, as when utilizing the transducer front face as a reflector (cf. Figs. 3.2 and 3.3), was not addressed in [PPB], and treated somewhat briefly in [PPC, PPD].

In the initial experimental work phase using the candidate measurement methods (cf. Sec. 4.2.1), two different approaches were considered regarding diffraction correction related to pulse echo mode (due to a reflecting circular transducer front face). One was to treat the reflecting aperture as a plane infinite perfectly reflecting baffle, such that the effect of the reflector is just to double the pulse propagation distance input in the diffraction correction model (such as e.g the plane piston diffraction correction model). The second approach was to treat the reflecting aperture as a new plane piston source with uniform vibration velocity across the front face. The latter approach was identified in [51, p. 91], whose implications are given in the following. The diffraction correction result using the two different approaches may differ considerably.

In the following, the second diffraction correction approach is underpinned by diffraction theory that applies for plane circular rigid disks, having no axial extension. The theory required the following assumptions to be made

1. the burst pulse of 35 periods applied in [PPC, PPD] is sufficiently stationary to be considered a harmonic wave;

2. the sound pulse impinges normally at the transducer front face;

3. the reflecting transducer may be treated as an infinitely thin circular rigid disk;

4. the pulse wave front is plane.

As for item 1, this holds only to some extent for the 2PEM and 3PM, for which the pulse shapes are not completely stationary, cf. [PPC, Fig. 8.5] and [PPD, Fig. 9.4], but lack about 5 periods to attain this. As for item 4, such an assumption may seem unreasonable as the reflector (i.e. transducer aperture) is located in the far field of the transducer (Fig. 3.6), where the waves tend to propagate spherically. However, as Fig. 3.6 indicates, the reflector is a relatively small portion of the sound field, with correspondingly little expected phase variations across the reflecting aperture.

The diffracted sound field from plane circular rigid disks (with no surrounding baffle) has been studied in several papers, e.g. [32, 95, 52, 82]. Both rigorous [82] and approximate [52] theory on the problem is provided for the case when the incoming waves are plane. The approximate theory [52] will here be applied, for which the details may be found in [52]. Generally, for $ka \gg 1$, where a is the disk radius, and small incident angles, the approximate theory represents a good approximation to the rigorous theory for the scattered velocity potential, Ψ^s [52, 83, 2].

Consider Fig. 3.7 that displays the geometry and quantities involved in the problem. Here, $z' = -z$, P is the point of observation, β is the angle from the axis of symmetry, and R is the distance from the disk center to the observation point.

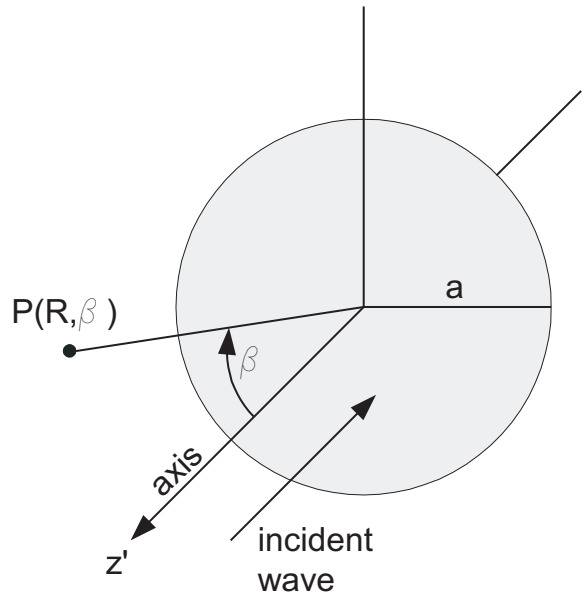

Figure 3.7: The plane rigid infinitely thin disk that diffracts/reflects the incident plane waves.

Let the incident wave be characterized by the velocity potential Ψ^{inc}, related to the pressure by $p^{inc} = -\imath\omega\rho\Psi^{inc}$. Hence a time variation $e^{-\imath\omega t}$ has been assumed, which is omitted in the following. The total velocity potential consists of the incident and scattered part, $\Psi = \Psi^{inc} + \Psi^s$. For normal incidence, $\Psi^{inc} = e^{-\imath kz'}$, and the approximate solution

for Ψ^s is given [52] as

$$\Psi^s(R,\beta) = -\imath a \left(\frac{e^{\imath kR}}{R}\right) \frac{J_1(ka\sin\beta)}{\tan\beta}, \quad R \to \infty. \tag{3.16}$$

Noteworthy, as the factor $-\imath$ implies, the phase of the scattered field leads the incident by 90° in the infinite far-field, which corresponds to the far-field limit of the plane piston diffraction correction, indicated in e.g. [PPA, Fig. 6.4]. Now, the far-field angular dependency (directivity) of Eq. (3.16), which is of primary interest, is compared to that of a plane piston source in an infinite rigid baffle [46, p. 182] in Fig. 3.8.

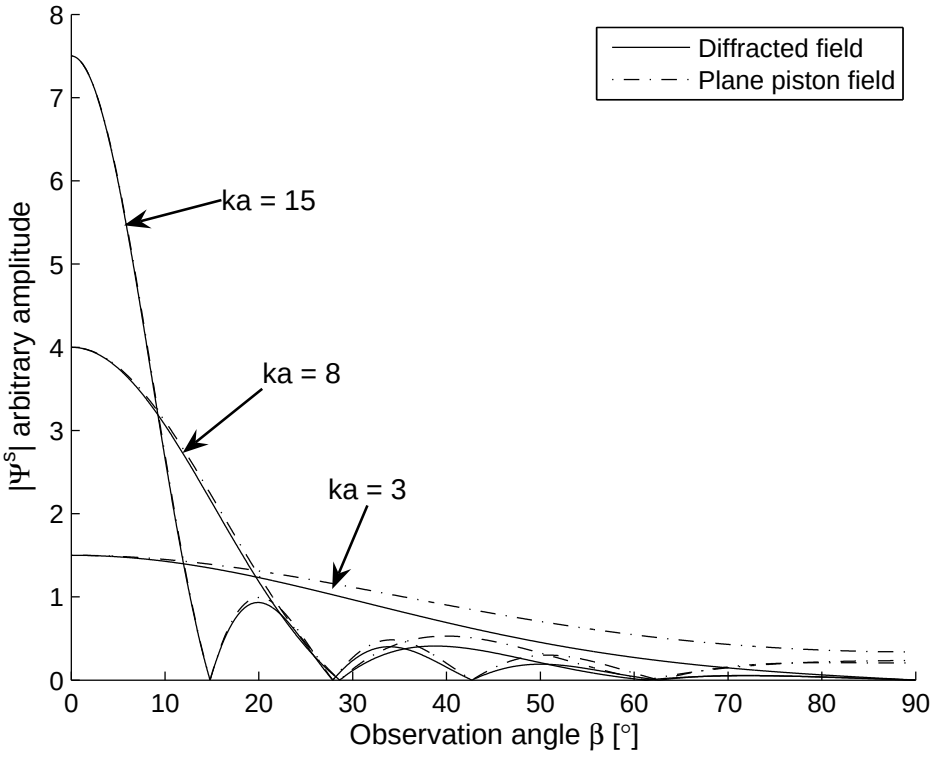

Figure 3.8: The far-field directivity of the scattered velocity potential, and that of a plane piston source in an infinite rigid baffle, for various ka-numbers.

It is observed that for β approaching zero and $ka \gg 1$, the directivity of Ψ^s coincides closely with that of the uniform plane piston source in the infinite far-field. With respect to diffraction correction, this supports the approach in [PPC, PPD], where the reflect-

ing transducer front face was treated as a new plane piston source. In such a case, the diffraction correction term t_2^{dif} may be decomposed in two and three parts for the 2PEM and 3PM, respectively, as is done in [PPC, PPD].

We must bear in mind, though, the simplifying assumptions that have been made: Firstly, the incoming waves are assumed to be plane across the reflector. Figure 3.6 indicates that the transducer front face is a relatively small portion of the incident main beam, with correspondingly little expected phase variations (in the far-field). So this may hold to some extent. Secondly, the reflecting disk is assumed to be infinitely thin, as opposed to the transducer which is extended axially. Finally, the theory applies to a rigid disk with no surrounding baffle or object, such as the transducer holder in the prototype measurement cell (Fig. 4.4). The consequences of such assumptions with respect to the measurement uncertainty have unfortunately not been evaluated for the 2PEM and 3PM in [PPC, PDD].

3.6.2 Thermal and viscous boundary layers

When sound waves are reflected at the transducer front face as in the candidate methods (cf. Figs. 3.2 and 3.3), thermal and viscous boundary layers are generated in a thin layer adjacent to the transducer front [88, p. 18]. The acoustic impedance of the fluid within this layer is thus altered, imposing a phase shift (and level reduction) of the echoes.

A complex pressure reflection coefficient, $\hat{R^{tv}}$, was in this work calculated to account for the phase shift of the reflected echo due to such effects, based on theory in [75]. The reflection coefficient, defined as the ratio of reflected pressure p_r and incident pressure p_i, is given for the case of normal incidence as [75, p. 109]

$$\hat{R^{tv}} = \frac{\hat{z} - \rho c}{\hat{z} + \rho c}, \tag{3.17}$$

where [75, p. 529]

$$\hat{z} = e^{\imath\pi/4}\rho c\left(\frac{\rho c^2}{\omega\mu}\right)^{1/2}\frac{\sqrt{Pr}}{\gamma-1}. \tag{3.18}$$

Here, μ is the viscosity and $Pr = \mu C_p/\kappa$ is the Prandtl number, where C_p is the specific heat at constant pressure and κ is the thermal conductivity. The resulting transit time corrections, which are implemented and quantified in [PPC, PPD], are calculated by

$$t_i^{tv} = \frac{\angle\hat{R}^{tv}}{\omega_0}. \tag{3.19}$$

As for the sign of t_i^{tv}, consider the following rationale: In [PPC, PPD] $\angle\hat{R}^{tv} > 0$, meaning that the transit times t_2 and t_4 for the 2PEM, and t_2 for the 3PM increase due to the boundary layers. Hence, the transit time difference Δt is increased in both candidate methods, cf. Eqs. (3.7) and (3.10). Now, from Eqs. (3.5), (3.9) and (3.12), it is clear that t_i^{tv} should have positive sign to yield a reduction in the transit time difference Δt, accounting for such effects. This is in accordance with the correction done in [PPC, PPD].

3.6.3 Internal transducer reflections

The ultrasonic Massa transducer used in this work seems to have a typical layered internal structure [PPB], comprising a matching layer in front, a piezoelectric disk, and a backing layer. Hence, when utilizing the transducer front as a reflector (as in the candidate methods), reduced and delayed echoes from the transducer interior will—to some extent—perturb the measurement echoes as coherent noise.

This effect was in the present work modeled to consider whether it should be corrected, but as shown below, it was reasonable to omit it as a correction term, and rather include it in the experimental uncertainty budgets [PPC, PPD]. A brief description of the transducer modeling is presented here. A one dimensional thickness extensional vibration model of the receiving transducer has been implemented, based on theory in [60]. The transducer is assumed to consist of a matching layer, piezoelectric disk and backing layer, in accordance with the apparent internal structure [PPB]. It is assumed that only one-

dimensional plane waves are present in the z-direction, and that influence of electrodes and glue can be neglected. The transducer, in receiving mode, is represented by a transmission line model, cf. Fig. 3.9.

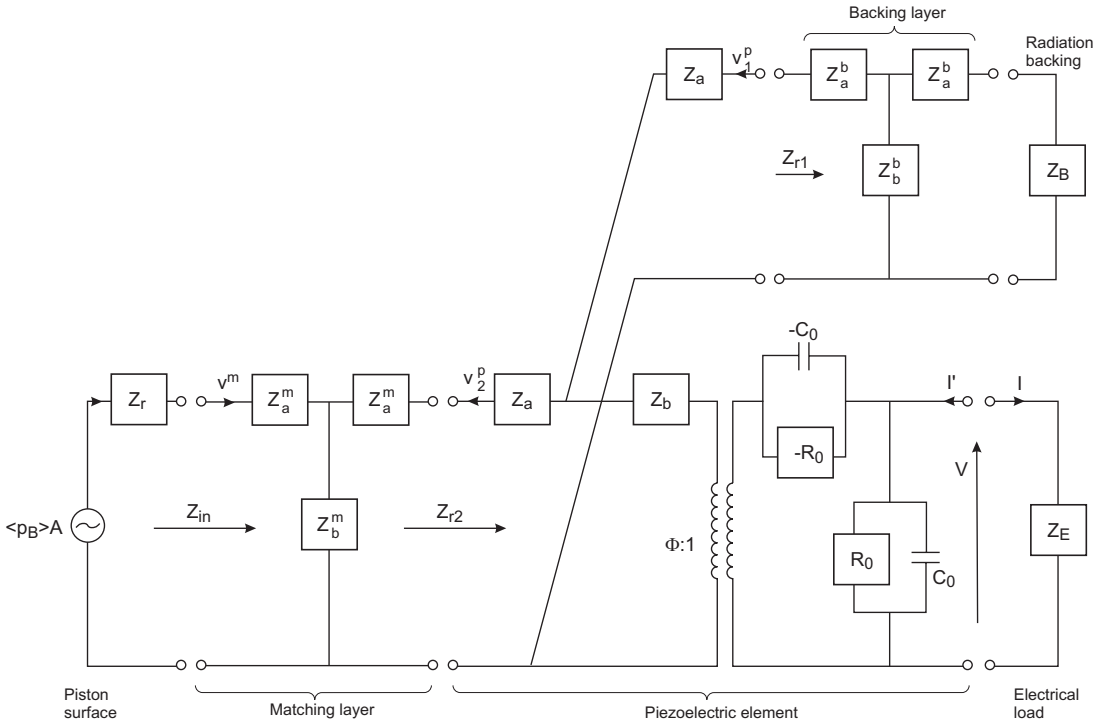

Figure 3.9: The one-dimensional transmission line model of the receiving transducer. The figure is taken from [60], with permission.

Referring to Fig. 3.9, the complex mechanical impedance of the backing layer is given by [60]

$$Z_{r1} = Z_a^b + Z_b^b - \frac{(Z_b^b)^2}{Z_a^b + Z_b^b + Z_B}, \tag{3.20}$$

where superscript b denotes backing layer, Z_B denotes mechanical radiation impedance for the backing layer,

$$Z_a^b \equiv \imath Z_0 \tan\left(\frac{\hat{k}\ell}{2}\right), \tag{3.21}$$

$$Z_b^b \equiv \frac{Z_0}{\imath \sin\left(\hat{k}\ell\right)}, \tag{3.22}$$

and

$$Z_0 \equiv \rho \hat{c} A. \tag{3.23}$$

Furthermore, $A = \pi a_d^2$ is the cross-sectional area of the circular transducer disk, a_d is the disk radius of the Massa transducer, ρ, $\hat{c}$, ℓ and $\hat{k}$ are the density, complex sound velocity, thickness and complex wave number of the respective layers. The complex wave number and complex sound velocity are respectively defined by [60]

$$\hat{k} \equiv \frac{\omega}{\hat{c}}, \tag{3.24}$$

$$\hat{c} \equiv c\left(1 + \frac{\imath}{Q}\right), \tag{3.25}$$

where c and Q respectively denote longitudinal sound velocity and longitudinal quality factor in the respective layers.

To calculate the combined complex impedance of the piezoelectric disk/element and backing layer, Z_{r2} (Fig. 3.9), the following equation was used [60]

$$Z_{r2} = Z_a^p + Z_b^{**} - \frac{(Z_b^{**})^2}{Z_a^p + Z_b^p + Z_{r1}}, \tag{3.26}$$

where superscript p denotes piezoelectric disk, Z_b^{**} is given by [60, Eq. (2.2.16)] and Z_a^p and Z_b^p are calculated by Eqs. (3.21) and (3.22), respectively, now input with material data for the piezoelectric disk, cf. Table 3.1.

Now the complex mechanical impedance of the three-layered equivalent circuit, Z_{in}, encountered by the incident sound wave, is calculated by [60]

$$Z_{in} = Z_a^m + Z_b^m - Z_b^m H^m, \tag{3.27}$$

where H^m is given by

$$H^m = \frac{Z_b^m}{Z_a^m + Z_b^m + Z_{r2}}. \tag{3.28}$$

Table 3.1: Material parameters input in the one-dimensional transducer model, in which the piezoelectric disk is taken to be piezoceramic PZT-5A [91]. The air parameters were chosen to comply with the conditions in [PPC, PDD].

Material	c [m/s]	ρ [kg/m^3]	Q	ℓ [mm]
Fluid: air at 27 °C, 30% rel. hum., 1 atm	348.2	1.17	∞	-
Front: silicone rubber	1020	950	30	1.1 – 1.5
Backing: foam rubber	1000	100	5	9.2

Here, superscript m denotes matching layer, and Z_a^m and Z_b^m are calculated by Eqs. (3.21) and (3.22), respectively, input with material data for the matching layer, cf. Table 3.1.

To investigate the phase shift due to interference with internal transducer reflections upon reflection at the transducer front, the complex pressure reflection coefficient, $\hat{\Re}$, is calculated. It is defined as the ratio of reflected sound pressure and normally incident sound pressure at the transducer front face, and obtained by [46]

$$\hat{\Re} = \frac{Z_{in} - \rho c A}{Z_{in} + \rho c A}, \tag{3.29}$$

in which ρ and c denote density and sound velocity of the fluid, respectively (cf. Table 3.1). Finally, the transit time perturbation, t^{int}, is given by

$$t^{int} = \frac{\angle \hat{\Re}}{\omega_0}. \tag{3.30}$$

The thicknesses of the matching layer and piezoelectric disk for an arbitrary Massa E-188/220 transducer sample have been measured to 1.31 mm and 1.57 mm, respectively [92], the backing layer thickness is about 9.2 mm, whereas a_d has been measured to 4.5 mm [92, PPB]. The material data are based on those used in the transducer modeling [PPB], outlined in Table 3.1.

Figure 3.10 shows t^{int} as a function of matching layer thickness. The reason for choosing matching layer thickness as input variable, was that the matching layer is somewhat soft, and thus expected to vary in thickness from transducer to transducer. Clearly, t^{int} is

highly sensitive to the matching layer thickness, but relatively small across the range, as it amounts to maximum 8 ppm relative to Δt for both candidate methods (per reflection, so that the total perturbation is twice this value) [PPC, PDD]. As mentioned, the matching layer thickness of the Massa transducer is expected to vary somewhat, hence, it seemed reasonable to omit t^{int} as correction term and rather include it as contribution to the overall experimental uncertainty budget [PPC, PDD] for both the candidate methods.

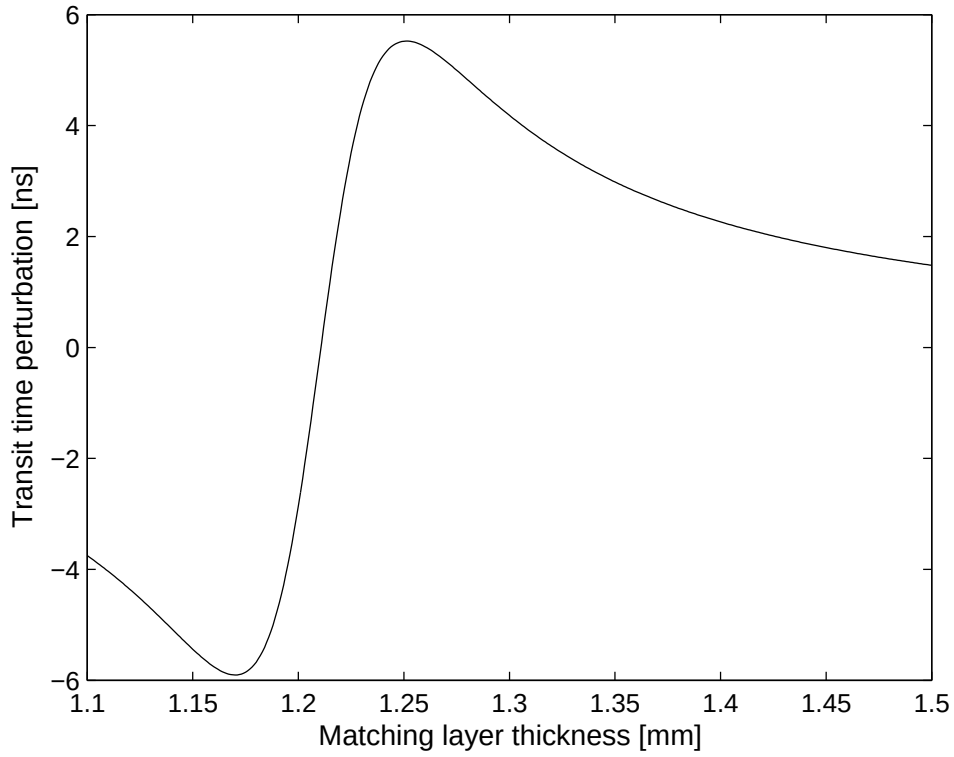

Figure 3.10: Variation in transit time perturbation for each reflection at the transducer front, as function of the matching layer thickness.

3.7 A sound velocity model for humid air

Various models for sound velocity in humid air at low pressure have been developed, see e.g. [65, 75, 99]. The sound velocity measurement results reported in this thesis, obtained for atmospheric humid air, have primarily been compared to a model for standard

atmospheric humid air [11]. The model was chosen due to (1) its realistic foundation, accounting for non-ideal gas effects by including the second virial coefficient in the sound velocity formula, and (2) its relatively sound empirical support [98, Table II]. Only a brief account of the model will be given here, cf. [11] for a more detailed description.

The sound velocity formula of the model [11] is given by

$$c_0^2 = \frac{\gamma RT}{M}\left[1 + \frac{2Bp}{RT}\right], \tag{3.31}$$

where c_0 is the zero frequency sound velocity, $\gamma = C_p/C_v$ is the ratio of specific heats, where C_v is the specific heat at constant volume, R is the universal gas constant, p and T are the thermodynamic pressure and temperature, respectively, M is the molar mass and B is the second virial coefficient. The formula is valid for low pressures, and suitable for use in experiments, as c_0 is a function of temperature and pressure, which may be readily measured using conventional instruments.

The quantities γ, M and B in Eq. (3.31) are however somewhat more challenging to obtain. The ratio of specific heats, γ, is difficult to model accurately, partly due to the need for d^2B/dT^2 [11]. Conveniently, however, an approximate formula for γ is provided in [11], which was used in the current model implementation. The approximate formula value agrees to within 35 ppm with the more comprehensive value [11].

Next, the molar mass M is needed. As air is a mixture of gases, including water vapor, M is a compound quantity. In the present model, standard air constitution has been assumed [39], for which the molar fractions of nitrogen, oxygen and argon are approximately 78%, 21% and 1%, respectively. Now, the molar mass of humid air is given by [25]

$$M = M_a x_a + M_w x_w, \tag{3.32}$$

where M_a and M_w are the molar masses of dry air and water vapor, respectively, and x_a

and x_w are the molar fractions of dry air and water, respectively. A spreadsheet of the air constituents and value of M_a may be found in [11, Table I]; a value for M_w is given in [25], and x_w is obtained from the measured relative humidity (RH), cf. [25].

Although the sound velocity model facilitates a variation in CO_2 concentration, it was in the present work set to 382 ppm [70], as the expected amount of variation affects c_0 relatively little. As an example, an increase in the CO_2 concentration of 200 ppm would decrease the predicted c_0 of about 50 ppm [PPC].

Finally, to obtain the second virial coefficient B, the following equation was used [11]

$$B = x_a^2 B_{aa} + 2x_a x_w B_{aw} + x_w^2 B_{ww}, \tag{3.33}$$

where B_{aa} and B_{ww} are the second virial coefficients for dry air and water vapor, respectively, and B_{aw} is the second interaction virial coefficient between the two gases. The quantities B_{aa} and B_{aw} were calculated using [37, Eq. (4)] and [37, Eq. (9)], respectively, and B_{ww} was obtained from [37, Eq. (A-5)]. Example results for the sound velocity, c_0, may be found in [11].

In the operating frequency range around 218 kHz, frequency dependent dispersion effects are significant. To account for these, so as to obtain the sound phase velocity c, the following expression was applied [11, 68]

$$\frac{1}{c_0} - \frac{1}{c} = \frac{\alpha_{vN}}{2\pi f_{rN}} + \frac{\alpha_{vO}}{2\pi f_{rO}}, \tag{3.34}$$

where α_{vN} and α_{vO} are the plane-wave attenuation coefficients due to vibrational relaxation of N_2 and O_2, respectively, and f_{rN} and f_{rO} are respectively the relaxation frequencies of N_2 and O_2. Relaxation contributions from less significant air gases are thus neglected. The attenuation coefficients were calculated according to [104], and the relaxation frequencies were calculated by means of formulae in [5, 6].

The dispersion correction, $c - c_0$, for humid air at, say 1 atm, 25 °C, 30% RH and a frequency of 218 kHz amounts to approximately 0.15 m/s, or 431 ppm at $c = 348$ m/s. This is more than twofold the target measurement uncertainty of the precision sound velocity cell [61]. To the author's knowledge, the uncertainty of the present dispersion correction has not been evaluated at a sufficient accuracy level in the frequency range relevant here. Unfortunately, this means that the overall uncertainty of the sound velocity model is in excess of the stated ±300 ppm [11], to an unknown extent. Some example plots on dispersion correction for air are provided in [92, p. 23].

Chapter 4

Experimental

In the current chapter, the experimental setups of the three sound velocity measurement methods used in this work are described. Section 4.1 concerns the experimental setup of the two-distance method, from which valuable experience was gained that later was used in the development of the two candidate methods. As this method was not intended for the precision sound velocity cell, it is only briefly summarized here. A three-step development process toward the *prototype sound velocity cell* is described briefly in Sec. 4.2. Only subjects scantly treated in papers C and D are included here, and emphasize is put on observations and challenges in the early experimental setups, as they constituted the basis of the final design of the prototype sound velocity cell.

4.1 The two-distance method

The purpose of using this preliminary method was twofold: (1) The method is flexible in the sense that the transducer separation may be varied, and also, the acoustic cavity is open and readily accessible for the experimentalist (in the present setup), and thus well suited for obtaining relevant experience and study various effects relevant for other transient methods; (2) the method has common properties with the two candidate methods [PPA] that could be tested using an existing measurement facility, developed as part of a doctoral work [93].

The theory was given in brief in Sec. 3.2 (cf. [PPA] for a more thorough treatment), and the experimental setup, primarily described in [PPA], is for convenience shown in Fig. 4.1. The transducer stages facilitate transducer alignment in all directions, including transversally off the axis. Notice the *Ealing series 53-8116/5* linear positioning stage at the base, enabling a transducer distance resolution of 5 μm. The (white plastic) transducer holders were equipped with the Massa E-188/220 ultrasonic air transducers [63], intended for operation around 220 kHz. They were primarily chosen due to

1. their bandwidth of 25 kHz (transmit mode at -3 dB), which is relatively broad compared to other off-the shelf air transducers. This is advantageous in order to minimize the transient region of the burst pulse;

2. their relatively narrow beam, having a total beam angle of $\pm 10^\circ$ at -3 dB, which is advantageous to keep the diffraction correction as low as possible; confer also [PPB];

3. they were already available and usable with the transducer alignment stages developed as part of [93], facilitating progress in the present experimental work.

The results obtained using the 2DM are reported in [PPA], and some of the conclusions drawn that were utilized in the development of the candidate methods are outlined in Chapter 5.

4.2 The candidate measurement methods

For the candidate measurement methods, the 2PEM and 3PM, identical transducer configurations could be used, cf. Figs. 3.2 and 3.3. Therefore, unless otherwise noted, the experimental setup descriptions below covers both candidate methods.

Figure 4.1: The experimental setup of the 2DM. The source and receiver transducer stages are seen to the left and right, respectively. The measurement chamber [PPA] is indicated in the background.

4.2.1 Experimental setup I

In experimental setup I, a slightly modified version of the setup shown in Fig. 4.1 was applied,[1] which is not designed for pulse-echo operation. However, the purpose was primarily to gain experience, evaluate effects critical to the measurement uncertainty, system settings, transducer separation etc., and utilize this knowledge in the design of the prototype measurement cell (Fig. 4.5).

The transducer separation L was varied over the range 157−200 mm for both measurement methods, which is a relevant range in the precision sound velocity cell [61]. The transducer separation was measured using a *Mitutoyo series 137* micrometer screw, with a stated uncertainty of 10 μm at $L = 200$ mm.[2] To facilitate measurements with the 2PEM, the transducer needed be switched from transmitting to receiving mode within a few microseconds. To facilitate this, a custom design switching circuit was developed, for which the circuitry is outlined in Appendix A.

[1] a spacer plate was inserted below the transducer stage to the left to reduce the transducer separation.

[2] for L = 150 mm, the uncertainty is about 8.2 μm [92], at an unknown confidence level, presumed to be 95%, as recommended in [38].

Transducer holders

Figure 4.2: The transducer holder developed as part of a doctoral work [93], surrounding the Massa E-188/220 ultrasonic air transducer.

Figure 4.2 is a close-up image of the transducer holders used in the present experimental setup (cf. Fig. 4.1). The holders are not designed for pulse echo operation as in the candidate methods. Hence, high measurement accuracy was not expected using this setup.

This is firstly due to the quite significant area of the annulus that surrounds the transducer front, which may cause a phase shift upon reflection if the transducer front face is not flush with the holder annulus. Secondly, the annular gap between the transducer and holder may cause a significant delayed echo that may interfere with the measurement echo. Thirdly, the gap between the transducer front and holder annulus represents a challenging geometry regarding diffraction correction, which is presumably difficult to model accurately.

Transducer ringing in the 2PEM

In the 2PEM, the transducers are switched to receiving mode within tens of nanoseconds after pulse transmission. Because of the finite bandwidth of the transducer, some time elapses from the electrical drive signal is switched off, until the transducer has stopped ringing [88, p. 220]. The transducers applied here [63] are still ringing slightly when the echoes ② and ④ arrives at the receiver[3], shifting the received echoes in phase (and magnitude), and thus the measured transit time. Such effects are illustrated (for the final

[3] at sound velocities around 348 m/s

experimental setup) in Fig. 4.3, and their influence on the measurement uncertainty is evaluated in [PPC].

Switching noise in the 2PEM

The 2PEM relies on the custom designed switching circuit, shown in Appendix A. Now every switching event is accompanied by a charge injection [1], taking the form of a coherent noise spike decaying roughly exponentially, cf. the upper subplot of Fig. 4.3.

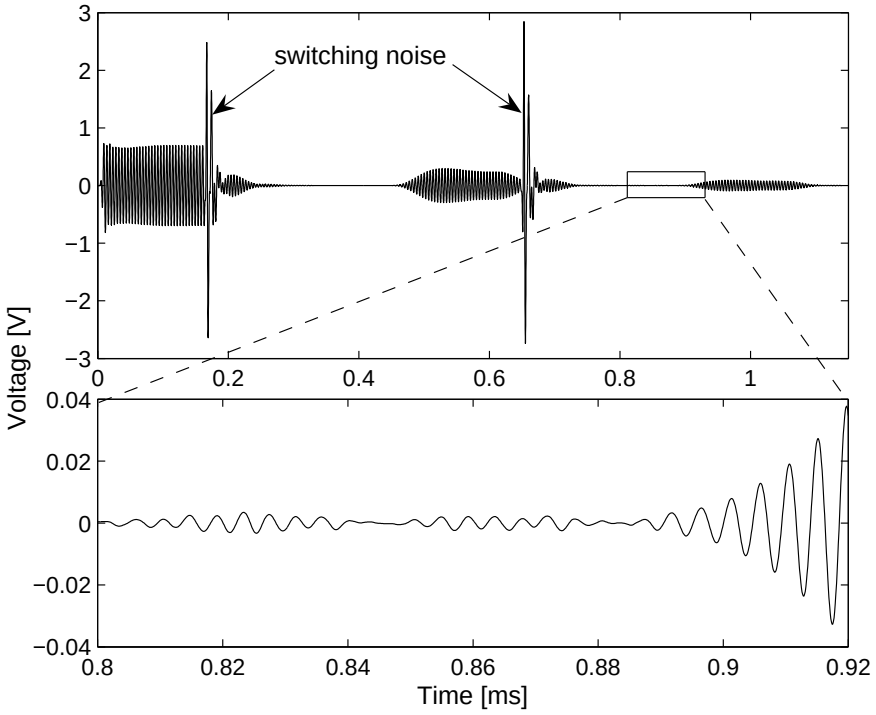

Figure 4.3: Upper subplot: a typical signal trace of the 2PEM, where the switching noise is emphasized. For clarity, only one channel is shown (showing e.g. signals ① and ②). Lower subplot: ringing noise present in the beginning of echo ②, visible from 0.8 to 0.88 ms.

A major problem associated with this noise was its elevated level which occasionally saturated the oscilloscope, and lead to shifted transit times. The following efforts were executed to avoid such effects.

- As the moment of switching is adjustable, it has been tuned to occur at the trailing edge of the burst signals (just after the transit time measurement range), so that

the available decay time of the switching noise is maximized;

- shunt resistors of 1000 Ω are coupled to the transducer input in order to dampen the noise, cf. Appendix A;
- butterworth bandpass filters (hardware and software) were applied to remove the highest frequency components of the noise spikes, which reduced the noise level significantly.

These efforts reduced the switching noise to a level subordinate of the transducer ringing noise.

Observations

Some observations regarding the current experimental setup were made. Modifications and tuning of the switching circuit was necessary to get the 2PEM working properly. In both candidate methods, a software *Matlab* bandpass filter was implemented to remove remaining bias from the electrical signal input at the oscilloscope. This was necessary despite of the fact that the oscilloscope was set in AC mode. Such bias causes a shift, i.e. error, in the measured transit time.

In these experiments, settings like sampling frequency f_s, burst center frequency f_0, and transducer separation L were varied. Some comments on these parameters are given below.

As for f_s, the simulation results in Sec. 3.5 indicate that 5 MHz should provide sufficient precision in the transit time detection. However, as the oscilloscope does not allow f_s to be 5 MHz in dual channel mode, it was decided to rather use $f_s = 10$ MHz in the remaining work [PPC, PPD]. There were no indications that this action lead to insufficient precision in the time detection, which would appear occasionally as large ripple in the transit time vectors.

The burst center frequency f_0 is primarily critical with respect to diffraction correction. In [PPB] it is indicated that $f_0 = 218$ kHz is a suitable center frequency, because at this frequency the plane piston diffraction correction model (Sec. 3.6.1) may probably be applied to the Massa transducer with little error, for a transducer separation in the range $15 - 20$ cm. Moreover, an f_0 of 218 kHz is experimentally found to be an optimal frequency with respect to minimizing the transient regime of the burst pulses.

Measurements were performed, using both candidate methods, for various values of L in the range 16 to 21 cm, while measured sound velocity relative to the model was monitored. There were no indications that varying L across this range affected the measurement results significantly. Also, the echo signal levels (cf. Figs. 3.2 and 3.3), which are distance dependent, appeared to be adequate over such distances.

4.2.2 Experimental setup II

In experimental setup II, a *measurement unit* was devised, providing a well defined transducer alignment where the transducers are separated axially by $L = 151$ mm, cf. Fig. 4.4. The measurement unit was in this experimental setup enclosed by the acoustically insulated measurement chamber described in [PPA].

Most parts of the measurement unit are labeled in Fig. 4.4; yet some parts need explicit explanation. The 'transducer cone', which elsewhere in this thesis is referred to as 'transducer holder', keeps the transducers aligned and in place. 'PT-100 clamp' refers to the clamping facility of the two PT-100 thermocouples that protrude 7 mm into the measurement cavity. 'Adjustment screw' refers to the screws of the parallelity adjustment plate facility of one of the transducers. The 'gage ring' facilitates a reference base for the adjustment plate, at which the transducer cones are aligned parallel to better than 0.02° with each other.

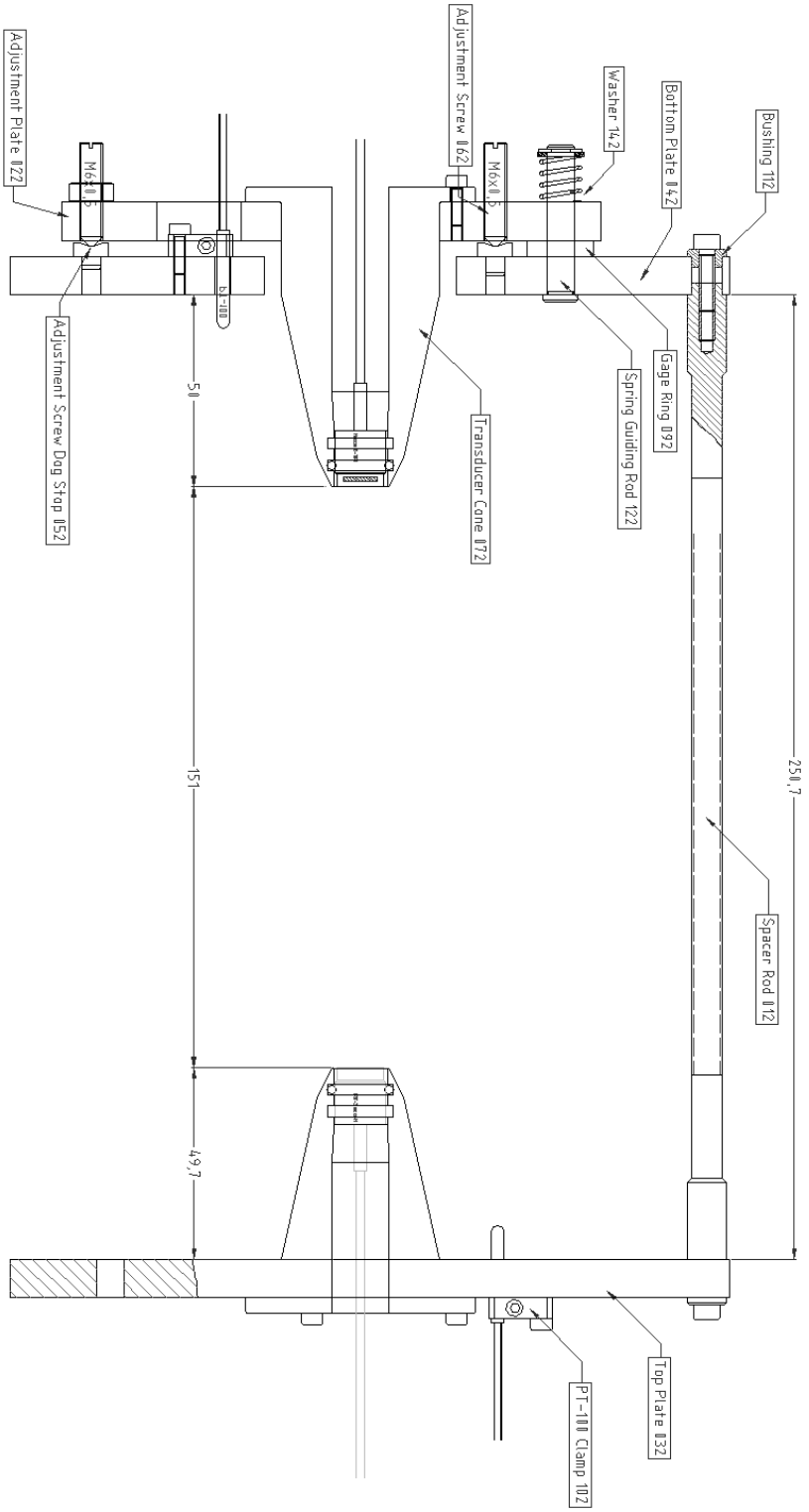

Figure 4.4: The design plot of the final version of the measurement unit. All dimensions are in millimeters.

Observations

The transducer holders of the measurement unit was, based on an initial version, redesigned (Fig. 4.4). The initial version was optimized with respect to angular alignment of the transducer, which was achieved by having direct contact between the transducer and holder. This lead to strong ringing effects in the 2PEM; the worst case SNR in the beginning of echoes ② and ④ (cf. Fig. 4.3, lower subplot) was about 25 dB, causing a relative shift in Δt of about 100 ppm, which is well beyond an acceptable value. To minimize such ringing effects, the final transducer holder suspends the transducer by one rubber o-ring in the frontmost part (cf. Fig. 4.4). Another advantage of using one rather than two o-rings for transducer suspension, is a significant reduction of acoustical cross-talk between the transducers (traveling via the measurement unit), to a negligible level.

As the front face of the transducer holders are parallel to within 0.02°, which is probably sufficient to avoid significant measurement error, it was attempted to align the transducer front face flush with the front annulus of the holder. The transducer was inserted in the holder by carefully pushing the transducer backwards, using a plane object, until it stopped at the holder front. To prevent that the o-ring, which is quite resilient, would reject the transducer slightly back, out of position, the o-rings were lubricated with grease. The transducer fronts are estimated to be parallel to within $\lambda/10$ using this configuration. It should be noted that the present design is "preliminary", and possibly not sufficient with respect to transducer parallelity for the precision sound sound velocity cell. The uncertainty contributions due to such effects were unfortunately not evaluated in the present work.

The experiments using experimental setup II were also troubled by medium convection currents due to temperature gradients [62, p. 269], causing a significant measurement spread. However, such effects were expected to be significantly reduced in a well defined precision sound velocity cell. Another important observation was that the transducer holders and transducer mounting should be carefully designed. This is of particular

importance with respect to controlling diffraction correction (cf. Sec. 3.6.1), reducing acoustical cross-talk, and optimizing the transducer parallelity alignment.

Nonlinearity measurements

Experiments using the current transducers in air have indicated effects of nonlinearity that affects the pulse transit time for transducer drive levels beyond $V_{in} = 1$ V (peak-peak; pp), which is approximately the drive level of the 2PEM [PPC]. Hence, this method is presumably not affected by such effects. For the 3PM it was, however, based on the findings below decided to use a somewhat higher transducer drive level than for the 2PEM. The reasoning behind this was to maximize the SNR of the somewhat weak echo ②, cf. [PPD], so as to obtain a more smooth and stationary transit time difference vector, from which Δt could be obtained (cf. Eq. (3.9)).

The following approach was taken to quantify the influence of nonlinearity effects on Δt for the 3PM: the variation in Δt was measured as a function of V_{in} within time intervals below 1 min, so that the temperature of the measurement medium was essentially constant. Preferably, $V_{in} = 1$ V pp should be used as reference drive level, as this represents the linear regime. However, as the SNR was rather poor in this range, such that air flickering gave a relatively large variance in Δt, it was decided to rather use $V_{in} = 2$ V pp as reference level. It was assumed that nonlinearity effects due to this action were negligible.

The measurements were carried out with atmospheric air as measurement medium, at a temperature and RH of about 24 °C and 24%, respectively. The temperature variation was less than 4 mK during the measurements, which is equivalent to a change of about 7 ppm in Δt.

On average, changing V_{in} from 2 V pp to 5 V pp resulted in a change in Δt of about -3 ns (95% conf. level). Due to the significant spread of the result, amounting to 5 ns, this value

was attributed to nonlinearity effects in the uncertainty budget in the final measurements using the 3PM [PPD]. This value corresponds to about 6 ppm relative to Δt, which is negligible compared to the other predominating uncertainty contributions [PPD].

4.2.3 Experimental setup III

This final experimental setup consists of a prototype sound velocity cell for pressures below 13 bara, containing the measurement unit described in previous subsection. The cell, shown in Figs. 4.5 and 4.6, features the option of using both candidate methods with the same measurement medium, rendering possible a direct experimental comparison.[4]

The design rationale of the cell, relevant for both candidate methods, is primarily covered in [PPC], but dimensional considerations are treated here. To provide flexibility with respect to measurement gas, and give plentiful measurement time windows, the prototype cell was designed for sound velocities up to 450 m/s. During the development work, the measurement unit was immersed into a steel pipe with approximately the intended cell diameter to check for interfering wall echoes. None such were observed for any of the two candidate methods, indicating that the current dimensions could be used in the prototype measurement cell.

Number of burst averages

The number of coherent burst averages N is basically limited by the measurement duration, which preferably be less than, say 1 s. A relatively low burst repetition rate is advantageous, to ensure that previous pulses essentially have died out in the cavity of the sound velocity cell. Experiments have indicated that a burst repetition rate below 40 Hz is required to fulfill this specification. With respect to suppression of random noise, it has been found that $N > 10$ be sufficient.

Another aspect which makes coherent averaging of several burst signals important, is

[4] notice however that the measurement electronics is slightly different [PPC, PPD].

timing jitter effects, which are due to the unsynchronized clock signal references of the function generator and oscilloscope. It is reasonable to assume that the jitter in sampled time point has a Gaussian probability density function [41]. Hence, perturbations in the transit time should be suppressed by averaging. It was in the present work assumed that $N = 15$ is sufficient to suppress timing jitter effects to an insignificant level, which complied with the requirement that the measurement duration of the candidate methods be less than 1 s. As a worst case example: if omitting the averaging by setting $N = 1$, the standard deviation of the transit time jitter would be less than 25 ns [31], corresponding to about 30 ppm relative to Δt (at $c = 348$ m/s [PPC, PPD]).

In the following, the dimensional analyses of the measurement cell is presented. It is based on a simplified arrival time estimation of the measurement signals and disturbing echoes, meaning that the wave fronts are taken to be rays. As the measurement cell is designed for both candidate methods, two separate transit time budgets are given. It has been found experimentally that a burst pulse of about 170 μs (37 periods at 218 kHz) is suitable for the Massa transducer to obtain a sufficiently stationary transit time regime from which Δt can be obtained.

Arrival times of signals and noise in the 2PEM

Referring to Fig. 4.5, the following dimensions provided 170 μs measurement time slot for the candidate methods: $L_0 = 151$ mm, $L_{pen} = 49.7$ mm, $r_{sp} = 86$ mm and $r_{cw} \in (101.5, 109.5)$ mm. The term r_{cw} is given as an interval because the measurement unit has its axis 4 mm off the cell axis. Now let t_{sp} denote the arrival time of an echo going via the spacer rod **3**, and t^1_{cw} and t^2_{cw} denote the arrival times of echoes traveling via the closest and most distant cell wall **12**, respectively. The term t_{E2} denotes the arrival time of an echo going via the end face **11** opposite to the source transducer—and back to the source. The estimated arrival times of the measurement signals and possible disturbing echoes are given for the 2PEM in Table 4.1, calculated for $c = 450$ m/s.

Table 4.1: Calculated arrival times of the measurement pulses and disturbing echoes for the 2PEM in the prototype sound velocity cell, shown in Fig. 4.5, for a sound velocity of 450 m/s.

Quantity	$t_1,\ t_3$	t_{sp}	t_{cw}^1	t_{cw}^2	$t_2,\ t_4$	t_{E2}
Arrival time [μs]	333	507	561	590	667	889

We note that the critical time slot is between t_{sp} and t_1 or t_3—amounting to 174 μs—as the time window between t_{E2} and t_2 or t_4 is larger (222 μs).[5] However, the possible echo due to the spacers **3**, arriving at t_{sp}, has not been observed in the measurements, suggesting that the actual available time slot for measurement using the 2PEM is 222 μs.

Arrival times of signals and noise in the 3PM

The arrival times of the measurement signals and possible disturbing echoes are given for the 3PM in Table 4.2, in which $c = 450$ m/s. An additional term, t_{E3}, has been introduced, denoting the travel time of an echo traveling from the source—to the opposite end face **11**—back to the opposite end face **11**—to the receiver.

Table 4.2: Calculated arrival times of measurement pulses and disturbing echoes for the 3PM in the prototype sound velocity cell (Fig. 4.5). The sound velocity c is 450 m/s.

Quantity	t_1	t_{sp}	t_{cw}^1	t_{cw}^2	t_2	t_{E3}
Arrival time	333	507	561	590	1000	1222

Table 4.2 shows that the critical time slot, $t_{sp} - t_1$, again is due to the echo traveling via the spacer rods **3**, which however not is experienced to yield a significantly disturbing echo, cf. previous section. Thus, the available time window is given by $t_{E3} - t_2 = 222$ μs, which incidentally is equal to the time window of the 2PEM.

[5] although the time separation between t_2 or t_4 and t_{cw}^2 is notably less than the required time slot, this is not critical because the echo associated with t_{cw}^2 does not arrive at the receiving transducer.

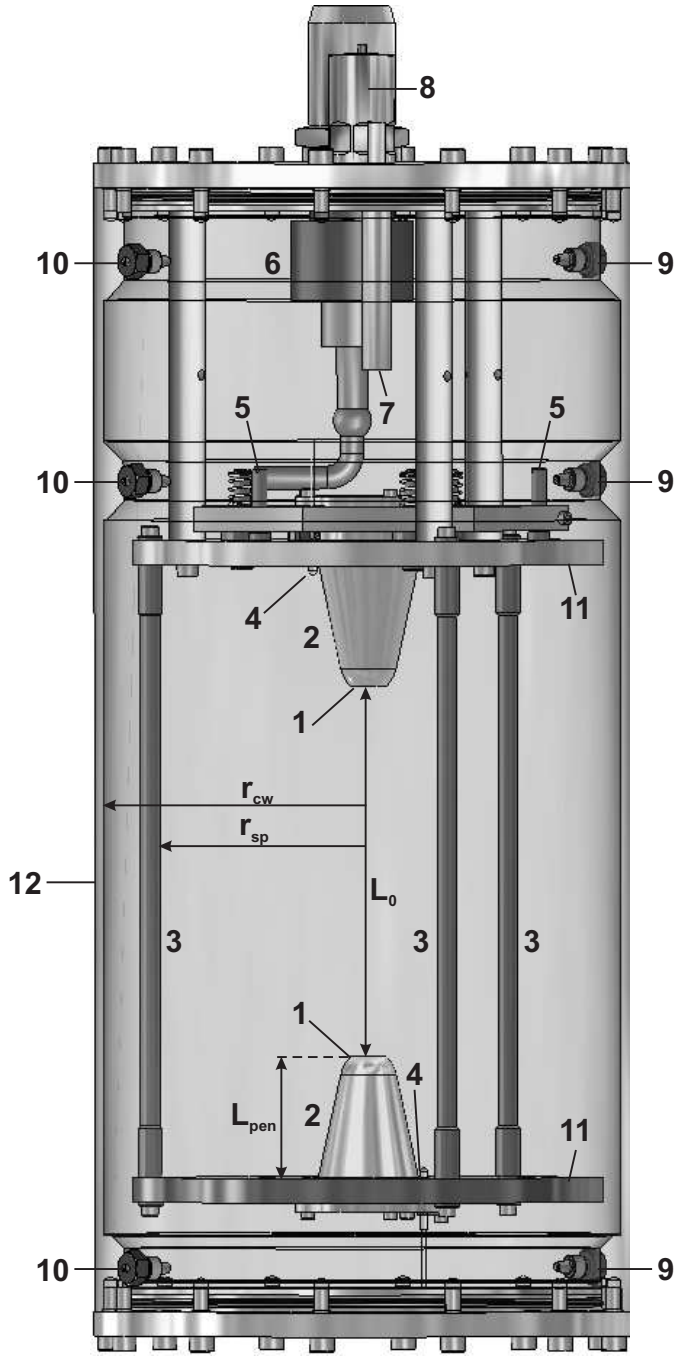

Figure 4.5: Cut-through design sketch of the prototype sound velocity measurement cell for low pressures. The numbers refer to the following objects. **1** ultrasonic transducers; **2** transducer holders; **3** transducer spacer rods; **4** *Pt-100* thermocouples; **5** parallelity adjustment screws; **6** cable feedthrough connector; **7** humidity sensor; **8** safety valve; **9** gas inlet ports; **10** gas outlet ports; **11** end faces, and **12** cell wall. Note that the wall was covered with a rugged, soft clothing (not shown) to spread and absorb wall echoes.

Figure 4.6: Bird view image of the manufactured prototype measurement cell. The three objects at the lid are from left to right cable feed-through connector, safety valve and RH probe.

Chapter 5

Concluding remarks

In paper A, the two-distance sound velocity measurement method for gases was used as a preliminary method to gain experience on transit time methods in general, and to investigate common features with the two proposed candidate methods for the precision sound velocity cell [61, PPC, PPD] in particular.

The attained experimental uncertainty was estimated to 282 ppm at 95% confidence level, and medium convection currents due to temperature gradients was found to be the predominant contributor to the experimental uncertainty. Hence, it was recognized that the presence of such effects be carefully considered when designing the prototype sound velocity cell. Also, it was found that the transducer drive level could cause effects of nonlinearity that affect the transit times, and thus the measured sound velocity. Care should thus be taken to limit or avoid such effects in the candidate methods by restricting the drive level.

Moreover, the findings [PPA] indicated that the uncertainty in the transit time detection method (zero crossing time detection combined with linear interpolation) was the least significant uncertainty contribution, considerably less than those due to convection currents and nonlinear effects. Indeed, this indicated a fair potential for using this transit time detection method in the candidate sound velocity measurement methods.

A great advantage with the 2DM compared to the candidate measurement methods is the relatively low influence of diffraction correction [PPA], which is challenging to evaluate [58]. Furthermore, it is expected to be less sensitive to angular misalignment of the transducer fronts. However, as was pointed out in the feasibility study for the precision sound velocity cell, a cell without moving parts is preferred [61], hence the 2PEM was not considered a candidate for the precision sound velocity cell.

It was expected that diffraction correction would be one of the major contributors to the measurement uncertainty using the candidate methods, 2PEM and 3PM [61, PPA], which motivated a more careful evaluation of the diffraction correction modelling than performed for the 2DM [PPA]. Hence, in Paper B, diffraction correction was investigated for the ultrasonic Massa transducer applied throughout this work, using a finite element model for diffraction correction [58, 56, 57, PPB].

In spite of strong indications that the Massa transducer vibrates very differently from a uniform plane piston source, a close agreement was found between the FEM [58, 56, 57, PPB] and the plane piston diffraction correction models [44, 45] for transducer separations in the range between the near field and the far field. In fact, a phase discrepancy of only 0.13° was found for a transducer separation of 15 cm, the distance used in the prototype cell, around the frequency of operation, 218 kHz, for a sound velocity of 340 m/s. This indicates thus that the plane piston diffraction correction model may be applied with little error to the Massa transducer under the conditions relevant in [PPC, PPD]. One should yet bear in mind the shortcomings of the FEM diffraction correction model [58, 56, 57, PPB], as well as numerical uncertainty due to limited numerical resolution.

Paper C concerned the Two-way pulse echo sound velocity measurement method for gases, proposed as a candidate for the precision sound velocity measurement cell. The 2PEM is based on a similar method, described in a patent article [86]. To the best of the author's

knowledge, the 2PEM, or the method in [86], has never before been realized experimentally so as to demonstrate their potential or performance.

Using the 2PEM, the present work demonstrates agreement to within 172 ppm between measured and modelled sound velocity [PPC], using air at about 1 atm, 27 °C and 30% relative humidity. This indicates a good potential for using the 2PEM in the precision sound velocity cell for gas. However, it must be noted that the employed sound velocity model for air have an uncertainty of at least ±300 ppm [11, PPC], besides that alternative sound velocity models do exist for humid air [99] which deviate by about 515 ppm from the present model [11].

The attained experimental uncertainty of the 2PEM was estimated to 130 ppm at 95% confidence level [PPC]. However, due to lacking knowledge of (i) the transducer front face planarity, (ii) the degree of angular misalignment between the transducer fronts, and (iii) the diffraction correction uncertainty,[1] the experimental uncertainty should be regarded preliminary and incomplete.

Paper D presented the Three-way pulse method for sound velocity measurements in gases, originally proposed as a candidate method for the precision sound velocity cell in the feasibility study [61]. The 3PM has—to the author's knowledge—never before been realized in an experimental setup; hence, the present measurement results are the first to yield indications of the performance of the 3PM.

The sound velocity measurement results were obtained for atmospheric air at a temperature and relative humidity of about 27 °C and 30%, respectively. The results agreed to within 144 ppm with the output from the sound velocity model [PPD], indicating a promising potential for use in the precision sound velocity cell for gas. It is however

[1] although the one-way diffraction correction was modelled quite carefully for the present Massa transducer [PPB], it was hardly feasible in this work to account for the overall diffraction correction uncertainty, comprising effects of e.g. an imperfect pulse echo diffraction correction model, transducer holders and skew beam lobes.

stressed, as for the 2PEM, that the present sound velocity model for humid air [11] has a relatively moderate uncertainty of at least ±300 ppm [11, PPC], besides that alternative models do exist [99].

Due to the electrical cross-talk noise in the beginning of the signal traces of the 3PM [PPD], the cross-correlation algorithm for detection of corresponding zero crossings occasionally failed. The zero crossing detection was therefore carried out manually,[2] which of course is not a viable approach in a measurement method for the precision sound velocity cell. It is underlined however, that this procedure was superfluous in experimental setup II, where coaxial transducer cables were used instead of the (non-coaxial) feedthrough connector of the prototype sound velocity cell (cf. Fig. 4.5).

The experimental uncertainty using the 3PM was estimated to 126 ppm at a 95% confidence level [PPD]. However, as for the 2PEM [PPC], the lacking estimate of the diffraction correction uncertainty (expected to dominate the uncertainty budget), lacking knowledge of the transducer front face planarity, and lacking knowledge of the angular misalignment between the transducer fronts, the experimental uncertainty budget should be regarded preliminary and incomplete.

For both candidate measurement methods, there were strong indications that convection currents (medium flow) due to temporal and spatial temperature variations caused significant spread in the sound velocity results. These effects were identified as a relatively large spread in the deviation from the model [PPC, PPD]. During this work, it was unfortunately not possible to immerse the prototype sound velocity cell in a properly regulated thermostat bath. The problem has in subsequent work been resolved, enabling a more homogeneous and stationary measurement temperature [59]. Sound velocity measurements with this modified experimental setup, using argon gas at atmospheric and room tem-

[2] in the following way: if the detection fails by one period, the measurement error amounts to about 5300 ppm, which is regarded an unrealistically poor measurement value. On this basis, the corresponding zero crossings were identified by "trial and error", using the predicted sound velocity from the model as reference.

perature conditions [59], demonstrated a result spread below 22 ppm for both candidate methods, representing a reduction in the total sound velocity spread by a factor of about 12 compared to the results presented herein [PPC, PPD].

Although the experimental uncertainty budgets for the candidate measurement methods presented here [PPC, PPD] were preliminary and incomplete, they are still valuable, as the predominating and critical uncertainty contributions are identified. This renders possible a more thorough evaluation of these in future work, so that the measurement uncertainty of the candidate methods be further reduced.

In papers C and D—where atmospheric air was used as measurement medium—it is concluded that the candidate measurement methods for the precision sound velocity cell have demonstrated a promising potential with respect to meeting the technical specifications for the sound velocity cell (cf. Sec. 1.3). Further confidence to such conclusions is provided in [59], where argon at atmospheric and room temperature conditions was used as measurement gas. The sound velocity measurements were found to agree to within 239 ppm and 224 ppm with the argon model [17] for the 2PEM and 3PM, respectively, given a model uncertainty of about 10 ppm [17]. The present work [PPC, PPD] and [59] indicate moreover that diffraction correction is a predominating and critical uncertainty contribution, which preferably be evaluated with an uncertainty below 100 ppm [59] in a possible realization of the precision sound velocity cell.

Bibliography

[1] Analog Devices, ADG453. http://www.analog.com/en/prod/0,,768_833_ADG453, 00.html, Aug. 2006.

[2] Baars, J. W. M. On the diffraction of sound waves by a circular disc. *Acustica 14* (1964), 289 – 296.

[3] Ball, S. J., Goodwin, A. R. H., and Trusler, J. P. M. Phase behaviour and physical properties of petroleum reservoir fluids from acoustic measurements. *Journal of Petroleum Science and Engineering 34* (2002), 1 – 11.

[4] Barreau, A., Gaillard, K., Béhar, E., Daridon, J. L., Lagourette, B., and Xans, P. Volumetric properties, isobaric heat capacity and sound velocity of condensate gas measurements and modelling. *Pluid phase equilibria 127* (1997), 155 – 171.

[5] Bass, H. E., Sutherland, L. C., and Zuckerwar, A. J. Atmospheric absorption of sound: Update. *Journal of the Acoustical Society of America 88* (1990), 2019 – 2022.

[6] Bass, H. E., Sutherland, L. C., Zuckerwar, A. J., Blackstock, D. T., and Hester, D. M. Atmospheric absorption of sound: Further developments. *Journal of the Acoustical Society of America 97* (1995), 680 – 683.

[7] Benedetto, G., Gavioso, R. M., and Spagnolo, R. Measurement of speed of sound in a gas-filled acoustic resonator. In *IEEE Instrumentation and Measurement, Technology Conference* (Brussels, Belgium, June 1996).

[8] Blend, H. Free-field technique for measuring ultrasonic dispersion and absorption in gases. *Journal of the Acoustical Society of America 47, Part 2* (1969), 757 – 761.

[9] Brooks, R. Determination of the velocity of sound in distilled water. *Journal of the Acoustical Society of America 32* (1960), 1422 – 1425.

[10] Colgate, S. O. Acoustic determination of phase equilibria, June 1992. Annual report (June 1991 - May 1992), University of Florida, Gainesville, Florida, USA. GRI Report No. GRI-92/0487, Gas Research Institute, Chicago, Illinois, USA.

[11] Cramer, O. The variation of the specific heat ratio and the speed of sound in air with temperature, pressure, humidity and CO_2 concentration. *Journal of the Acoustical Society of America 93* (1993), 2510 – 2516.

[12] Daridon, J. L. Mesure de la vitesse du son dans le fluides sous pression composés de constituants gazeux et liquides. *Acoustic 80* (1994), 416 – 419.

[13] Dorr, J. A. Ultrasonic apparatus for measuring the speed of sound in a gaseous medium. US Patent No. 4,938,066, July 1990.

[14] Duan, Y. Y., Sun, L. Q., Shi, L., Zhu, M. S., and Han, L. Z. Speed of sound and ideal-gas heat capacity at constant pressure of gaseous trifluoroiodomethane (CF_3I). *Fluid Phase Equilibria 137* (1997), 121 – 131.

[15] El-Hakeem, A. S. Velocity of sound in nitrogen and argon at high pressures. *Journal of Chemical Physics 42* (1965), 3132 – 3133.

[16] Estela-Uribe, J. F., and Trusler, J. P. M. Acoustic and volumetric virial coefficients of nitrogen. *International Journal of Thermophysics 21* (2000), 1033 – 1044.

[17] Estrada-Alexanders, A. F., and Trusler, J. P. M. The speed of sound in gaseous argon at temperatures between 110 K and 450 K and pressures up to 19 MPa. *Journal of Chemical Thermodynamics 27* (1995), 1075 – 1089.

[18] Personal communication with Kjell-Eivind Frøysa, Christian Michelsen Research AS, Bergen, Norway, 2004.

[19] FRØYSA, K.-E., AND LUNDE, P. Mass and energy measurement of natural gas using ultrasonic flow meters. Recent results. In *Proc. 27th Scandinavian Symposium on Physical Acoustics* (Ustaoset, Norway, Jan. 2004).

[20] FRØYSA, K.-E., AND LUNDE, P. Density and calorific value measurement in natural gas using ultrasonic flow meters. In *Proc. 23rd International North Sea Flow Measurement Workshop* (Tønsberg, Norway, Oct. 2005).

[21] FRØYSA, K.-E., LUNDE, P., PAULSEN, A., AND JACOBSEN, E. Density and calorific value measurement in natural gas using ultrasonic flow meters. Results from testing on various north sea gas field data. In *Proc. 24th International North Sea Flow Measurement Workshop* (Glasgow, UK, Oct. 2006).

[22] GAMMON, B. E., AND DOUSLIN, D. R. A system for measuring the velocity of sound in compressed fluids and its application to helium between -175 and 150°C. In *Proc. of the Fifth Symposium on Thermophysical Properties* (New York, U.S.A., 1970), The American Society of Mechanical Engineers.

[23] GAMMON, B. E., AND DOUSLIN, D. R. The velocity of sound and heat capacity in methane from near-critical to subcritical conditions and equation-of-state implications. *Journal of Chemical Physics 64* (1976), 2556 – 2568.

[24] GIACOBBE, F. W. Precision-measurement of acoustic velocities in pure gases and gas-mixtures. *Journal of the Acoustical Society of America 94* (1993), 1200 – 1210.

[25] GIACOMO, P. Equation for the determination of the density of moist air. *Metrologia 18* (1982), 33 – 40.

[26] GOLIK, A. Z., KUZOVSKOV, Y. I., AND NAGIN, V. Y. Pulse equipment for the measurement of ultrasound absorbtion coefficient and speed in liquids under high pressure. *Akustika i Ultrazvukovaya Tekhnika (Kiev) 247* (1989), 184 – 189.

[27] Goodwin, A. R. H., Hill, J. A., and Savidge, J. L. Acoustic measurements in natural gas mixtures. In *International Gas Research Conference* (Cannes, France, 1995), vol. 1, pp. 681 – 684. Government Studies, Inc., Rockville, MD, USA.

[28] Greenspan, M., and Thompson, M. C. An eleven megacycle interferometer for low pressure gases. *Journal of the Acoustical Society of America 25* (1953), 92 – 96.

[29] He, M. G., Liu, Z. G., and Yin, J. M. Measurement of speed of sound with a spherical resonator: HCFC-22, HFC-152a, HFC-143a, and Propane. *International Journal of Thermophysics 23* (2002), 1599 – 1615.

[30] Herzfeld, K. F., and Litowitz, T. A. *Absorption and dispersion of ultrasonic waves.* Academic press, New York, USA, 1959.

[31] Hewlett packard. *HP33120A. Function generator / Arbitrary Waveform Generator*, 5 ed., Aug. 1997.

[32] Huang, C.-J., and Chwang, A. T. Diffraction of acoustic waves by rigid plane baffles. *Journal of the Acoustical Society of America 95* (1994), 668 – 680.

[33] Hubbard, J. C. The acoustic resonator interferometer: II. Ultrasonic velocity and absorption in gases. *Physical Review 41* (1932), 523 – 535.

[34] Hubbard, J. C., and Zartman, I. F. A fixed path acoustic interferometer for the study of matter. *Review of Scientific Instruments 10* (1939), 382.

[35] Hurly, J. J. Thermophysical properties of nitrogen trifluoride, ethylene oxide, and trimethyl gallium from speed-of-sound measurements. *International Journal of Thermophysics 23* (2002), 667 – 696.

[36] Hurly, J. J. Thermodynamic properties of gaseous nitrous oxide and nitric oxide from speed-of-sound measurements. *International Journal of Thermophysics 24* (2003), 1611 – 1635.

[37] Hyland, R. W. A correlation for the second interaction virial coefficients and enhancement factors for moist air. *Journal of Research of National Bureau of Standards—A. Physics and Chemistry 79A* (1975), 551 – 560.

[38] Guide to the expression of uncertainty in measurement, first ed. International Organization for Standardization, Geneva, Switzerland, 1995. ISBN: 92-67-10188-9.

[39] ISO 2533-1975. Standard atmosphere. Tech. rep., International Organization for standardization (ISO), 1975.

[40] Jarvis, G. K., Johnson, K. A., and Walmsley, S. L. An annular resonator used to measure the speed of sound in gasous fluoralkanes: Trifluormethane and hexafluormethane. *Journal of Chemical & Engineering Data 41* (1996), 220 – 230.

[41] Kalashnikov, A. N., and Challis, R. E. Errors and uncertainties in the measurement of ultrasonic wave attenuation and phase velocity. *IEEE Transactions on Ultrasonics, Ferroelectrics, and Frequency Control 52* (2005), 1754 – 1768.

[42] Kelner, E., Minachi, A., Owen, T. E., Burzynski Jr., M., and Petullo, S. P. Device for precision measurement of speed of sound in a gas. US Patent No. 6,823,716, Nov. 2004.

[43] Keolian, R., Garret, S., Maynard, J., and Rudnick, I. Acoustic measurement of isotropic concentration of gases. *Journal of the Acoustical Society of America 64(S1)* (1978), S61.

[44] Khimunin, A. S. Numerical calculation of the diffraction corrections for the precise measurement of ultrasound absorption. *Acustica 27* (1972), 173 – 181.

[45] Khimunin, A. S. Numerical calculation of the diffraction corrections for the precise measurement of ultrasound phase velocity. *Acustica 32* (1975), 192 – 200.

[46] Kinsler, L. E., Frey, A. R., Coppens, A. B., and Sanders, J. V. *Fundamentals of acoustics*, 4th ed. John Wiley and sons, Inc., New York, USA, 2000.

[47] Kocbach, J. Finite element modeling of ultrasonic piezoelectric transducers. Influence of geometry and material parameters on vibration, response functions and radiated field. Dr. Scient thesis, University of Bergen, Dept. of Physics, Bergen, Norway, 2000.

[48] Kocbach, J., Lunde, P., and Vestrheim, M. FE simulations of piezoceramic disks with a front layer of varying thickness. In *Proc. IEEE International Ultrasonics Symposium* (Caesars Tahoe, USA, Oct. 1999). pp. 1113 – 1117.

[49] Kocbach, J., Lunde, P., and Vestrheim, M. Resonance frequency spectra with convergence tests of piezoceramic disks using the finite element method. *Acustica 87* (2001), 271 – 285.

[50] Kortbeek, P. J., Biswas, S. N., and Trappeniers, N. J. PVT and sound velocity measurements for CH_4 up to 10 kbar. *Physica 139 & 140B* (1986), 109 – 112.

[51] Krautkrämer, J., and Krautkrämer, H. *Ultrasonic testing of materials.* Springer-Verlag, Berlin, Germany, 1977.

[52] Leitner, A. Diffraction of sound by a circular disk. *Journal of the Acoustical Society of America 21* (1949), 331 – 334.

[53] Lestz, S. S. A method for measuring the sound wavelength in gases. *The American Journal of Physics 31* (1963), 96 – 98.

[54] Liebenberg, D. H., Mills, R. L., and Bronson, J. C. High-pressure apparatus for simultaneous adiabatic and isothermal compressibility measurement: Data on argon to 13 kbar. *Journal of Applied Physics 45* (1974), 741 – 747.

[55] Lunde, P., and Frøysa, K.-E. Mass and energy measurement of gas using ultrasonic flow meters. In *Proc. 25th Scandinavian Symposium on Physical Acoustics* (Ustaoset, Norway, Jan. 2002).

[56] Lunde, P., Frøysa, K.-E., Kippersund, R. A., and Vestrheim, M. Transient diffraction effects in ultrasonic meters for volumetric, mass and energy flow measurement of natural gas. In *Proc. 21st International North Sea Flow Measurement Workshop* (Tønsberg, Norway, Oct. 2003). pp. 33 – 59.

[57] Lunde, P., Kippersund, R. A., Vestrheim, M., and Frøysa, K.-E. Finite element modelling of diffraction correction for non-uniformly vibrating piezoelecric ultrasonic transducers. Manuscript to be submitted to a peer refereed journal.

[58] Lunde, P., Kippersund, R. A., Vestrheim, M., and Frøysa, K.-E. Transient diffraction effects in piezoelectric ultrasonic transducers using finite element modelling. In *Proc. 27th Scandinavian Symposium on Physical Acoustics* (Jan. 2004). CD issue only, ISBN 82-8123-000-2.

[59] Lunde, P., Norli, P., Vestrheim, M., and Kippersund, R. A. Precision sound velocity cell as reference for gas quality measurement in ultrasonic flow meters. In *Proc. 30th Scandinavian Symposium on Physical Acoustics* (Geilo, Norway, Jan. 2007).

[60] Lunde, P., and Vestrheim, M. Pizeoelectric transducer modelling. Thickness mode vibration. Tech. Rep. CMI-91-A10003 (Confidential), CMR, Bergen, Norway, Dec. 1991.

[61] Lunde, P., and Vestrheim, M. Precision sound velocity cell for natural gas at high pressures. Phase 1 — feasibility study. Tech. Rep. CMR-98-F10039 (Confidential), CMR, Bergen, Norway, Dec. 1998.

[62] Mansfield, M., and O'Sullivan, C. *Understanding physics.* John Wiley & Sons, Chichester, England, 1998.

[63] The massa E-188/220 transducers, Massa Corporation [Online]. http://www.massa.com/datasheets/e188.html, Jan. 2006.

[64] Mehl, J. B., and Moldover, M. R. Precision acoustic measurements with a spherical resonator: Ar and C_2H_4. *Journal of Chemical Physics 74* (1981), 4062 – 4077.

[65] Miller, D. C. *Sound waves. Their shape and speed.* The Macmillan Company, New York, USA, 1937.

[66] Moldover, M. R., Mehl, J. B., and Greenspan, M. Gas filled spherical resonators: Theory and experiment. *Journal of the Acoustical Society of America 79* (1986), 253 – 272.

[67] Moldover, M. R., Trusler, J. P. M., Edwards, T. J., Mehl, J. B., and Davis, R. S. Measurement of the universal gas constant R using a spherical acoustic resonator. *Journal of Research of National Bureau of Standards 93* (1988), 85 – 144.

[68] Morfey, C. L., and Howell, G. P. Speed of sound in air as a function of frequency and humidity. *Journal of the Acoustical Society of America 68* (1980), 1525 – 1527.

[69] Morse, P. M., and Ingard, K. U. *Theoretical acoustics.* Princeton university press, Princeton, New Jersey, USA, 1968.

[70] National Oceanic and Atmospheric Administration (NOAA) [Online]. http://www.cmdl.noaa.gov/ccgg/trends/, June 2006.

[71] Norli, P. Comparison of three methods for precision sound velocity measurement of gases. In *Proc. 28th Scandinavian Symposium on Physical Acoustics* (Ustaoset, Norway, Jan. 2005). ISBN 82-8123-000-2.

[72] Norli, P., Lunde, P., and Vestrheim, M. Methods for precision sound velocity measurements in pressure cells for gas characterization. In *Proc. 27th Scandinavian Symposium on Physical Acoustics* (Ustaoset, Norway, Jan. 2004). CD issue only, ISBN 82-8123-000-2.

[73] Regulations relating to measurement of petroleum for fiscal purposes and for calculation of CO_2 tax. Norwegian Petroleum Directorate (NPD), Nov. 2001.

[74] Fiscal measurement systems for hydrocarbon gas. NORSOK standard I-104. Norwegian Technology Standards Institution (NTS), June 1998. Revision 2.

[75] Pierce, A. D. *Acoustics. An introduction to its physical principles and applications.* McGraw-Hill, USA, 1981.

[76] Pierce, G. W. Piezoelectric crystal oscillators applied to the precision measurement of the velocity of sound in air and CO_2 at high frequencies. In *Proc. of the American Academy of Arts and Sciences* (1925), vol. 60, pp. 270 – 302.

[77] Pinkerton, J. M. M. On the pulse method of measuring ultrasonic absorption in liquids. *Proceedings of the Physical Society of London 62B* (1949), 286 – 299.

[78] Quinn, T. J., Colclough, A. R., and Chandler, T. R. D. A new determination of the gas constant by an acoustical method. *Philosophical Transactions of the Royal Society of London, Series A: Mathematical and Physical Sciences 283* (1976), 367 – 420.

[79] Sato, H., Ito, K., and Aizawa, Y. Simultaneous velocity and attenuation measurements applicable to various solids at high pressures and temperatures up to 1200 °C. *Measurement Science and Technology 15* (2004), 1787 – 1793.

[80] Sivaraman, A., and Gammon, B. E. Thermophysical properties of natural gas components determined by speed of sound measurements. Speed of sound measurements in methane. Tech. Rep. Report No. NIPER-142, National Institute for Petroleum and Energy Research, Bartlesville, Oklahoma, USA, Feb. 1986.

[81] Smith, D. H., and Harlow, R. G. The velocity of sound in air, nitrogen and argon. *British Journal of Applied Physics* (1963), 102 – 106.

[82] Spence, R. D. The diffraction of sound by circular disks and apertures. *Journal of the Acoustical Society of America 20* (1948), 380 – 386.

[83] Spence, R. D. A note on the Kirchoff approximation in diffraction theory. *Journal of the Acoustical Society of America 21* (1949), 98 – 100.

[84] Starling, K. E., and Savidge, J. L. Compressibility factors of natural gas and other related hydrocarbon gases. A.G.A. Transmission measurement committee report No. 8 (AGA-8). Tech. rep., American Gas Association, Arlington, Virginia, Nov. 1992. 2nd printing July 1994.

[85] Sun, L. Q., Duan, Y. Y., Shi, L., Zhu, M. S., and Han, L. Z. Speed of sound and ideal-gas heat capacity at constant pressure of gaseous difluoromethane. *Journal of Chemical & Engineering Data 42* (1997), 795 – 799.

[86] Suzuki, H., Tanaka, H., and Hachisuka, H. Method and apparatus for ultrasonic wave measurement. US Patent No. 6,094,987, Aug. 2000.

[87] Tempest, W., and Parbrook, H. D. The absorption of sound in argon, nitrogen and oxygen. *Acustica 7* (1957), 354 – 362.

[88] Trusler, J. P. M. *Physical acoustics and metrology of fluids.* The Adam Hilger Series on Measurement Science and Technology. Adam Hilger, Bristol, England, 1991.

[89] Trusler, J. P. M., and Zarari, M. P. The speed of sound and derived thermodynamic properties of methane at temperatures between 275 K and 375 K and pressures up to 10 MPa. *Journal of Chemical Thermodynamics 24* (1992), 973 – 991.

[90] Van Itterbeek, A., Van Dael, W., and Grevendonk, W. *Physica 25* (1959), 640.

[91] Five modern piezoelectric ceramics, bulletin 66011f, 1976. Vernitron Ltd., England; now Morgan Matroc Ltd.

[92] VERVIK, S. Transitt-tidsbestemmelse for ultralyd strømningsmetre. Nullstrømningsforhold. Cand. Scient. thesis, University of Bergen, Dept. of Physics, Bergen, Norway, Jan. 1995. (in norwegian).

[93] VERVIK, S. Methods for characterization of gas-coupled ultrasonic sender-receiver measurement systems. Dr. Scient thesis, University of Bergen, Dept. of Physics, Bergen, Norway, Dec. 2000.

[94] VORONOV, F. F., PITAEVSKAYA, L. L., AND BILEVICH, A. V. Rate of propagation of ultrasound in nitrogen at pressures up to 4 kbar and temperatures in the range 25 – 175 °C. *Russian Journal of Physical Chemistry 43* (1969), 321 – 324.

[95] WIENER, F. M. The diffraction of sound by rigid disks and rigid square plates. *Journal of the Acoustical Society of America 21* (1949), 334 – 347.

[96] WILLIAMS, J., AND LAMB, J. On the measurement of ultrasonic velocity in solids. *Journal of the Acoustical Society of America 30* (1958), 308 – 313.

[97] WILLIAMS JR., A. O. The piston source at high frequency. *Journal of the Acoustical Society of America 23* (1951), 1 – 6.

[98] WONG, G. S. K. Speed of sound in standard air. *Journal of the Acoustical Society of America 79* (1986), 1359 – 1366.

[99] WONG, G. S. K., AND EMBLETON, T. F. W. Variation of the speed of sound in air with humidity and temperature. *Journal of the Acoustical Society of America 77* (1985), 1710 – 1712.

[100] YOUNGLOVE, B. A., AND FREDERICK, N. V. Speed-of-sound measurements in liquid and gaseous air. *International Journal of Thermophysics 13* (1992), 1033 – 1041.

[101] YOUNGLOVE, B. A., AND MCCARTY, R. D. Speed-of-sound measurement for nitrogen gas at temperatures from 80 to 350 K and pressures to 1.5 MPa. *Journal of Chemical Thermodynamics 12* (1980), 1121 – 1128.

[102] Zhang, C., Duan, Y.-Y., Shi, L., Zhu, M. S., and Han, L.-Z. Speed of sound, ideal-gas heat capacity at constant pressure, and second virial coefficients of HFC-22yea. *Fluid phase equilibria 178* (2001), 73 – 85.

[103] Zhu, M. S., Han, L. Z., Zhang, K. Z., and Zhou, T. Y. Sound-velocity and ideal-gas specific-heat of gaseous 1,1,1,2-tetrafluoroethane (R134a). *International Journal of Thermophysics 14* (1993), 1039 – 1050.

[104] Zuckerwar, A. J., and Meredith, R. W. Low-frequency absorption of sound in air. *Journal of the Acoustical Society of America 78* (1985), 946 – 955.

Chapter 6

Paper A

Investigation of precision sound velocity measurement methods as reference for ultrasonic gas flow meters

Authors:

Petter Norli, Per Lunde and Magne Vestrheim

Reformatted version of the paper originally published in:

Proceedings of the 2005 IEEE Ultrasonics symposium, Rotterdam, The Netherlands, 18 – 21 September 2005, pp. 1443 – 1447.

Abstract

Ultrasonic gas flow meters for volumetric flow rate fiscal metering of natural gas (USMs) may possibly also be used for mass and energy flow rate measurement, partially based on velocity of sound (VOS) measurement. To establish the accuracy of the VOS measurements given by the USM, and for traceability purposes, an independent and high-accuracy VOS measurement cell may be used as reference. To include relevant effects of dispersion, the cell should preferably work in the operational frequency range of USMs, e.g. 100-200 kHz, with natural gas under high pressure.

Three different transient methods are investigated, aiming to realize a VOS measurement cell, and they are seen to have several common experimental uncertainty sources. In the present work, a two-distance method is discussed in more detail as an example, and some results from measurements in an insulated chamber with air at 1 atm and ca. 25 °C are presented.

The relative expanded measurement uncertainty was estimated according to ISO guidelines to 282 ppm (95 % conf. level). One major source of measurement uncertainty was experienced to be small convection currents in the chamber. Without these, the expanded uncertainty would have been about 162 ppm. Such convection effects are expected to be strongly reduced in a properly designed measurement cell.

The VOS measurement results were compared with predictions from a VOS model for standard air, including dispersion [J. Acoust. Soc. Amer. 93 (5), pp. 2510-2516, 1993], resulting in a mean deviation of -18 ppm with a two standard deviation spread in the data of 190 ppm over the temperature range.

6.1 Introduction

Ultrasonic gas flow meters (USM) are currently employed to measure gas volumetric flow rate in fiscal gas metering. As the USM gives a measurement of the velocity of sound (VOS) in addition to the volumetric flow rate, it may offer a potential for gas density and energy measurement [1].

Recent developments have proposed methods for calculation of the mass and energy content of the gas from the measured VOS, pressure and temperature [1]. If using the USM as an energy or mass flow meter, the uncertainty in the VOS output from the USM should be evaluated against an independent, accurate and documented method. No such reference method exists today, raising the need for a precision VOS measurement cell for natural gases.

A feasibility study for realizing such a cell has been carried out [2]. The literature on the field appears to be extensive, but none of the identified measurement methods could directly meet the specifications given below. VOS measurement cells with extreme accuracy are available in the audio frequency range, for which uncertainties down to 1 ppm have been reported. Less work was however identified at a sufficient accuracy level in the frequency range 100-200 kHz. A more recent literature study was carried out in 2004 [3], still not revealing any directly applicable cell method. The most promising methods needed development, or alternatively, a new method should be devised.

Tentative technical cell specifications have been pointed out [2], and the absolute VOS measurement uncertainty should not exceed $\pm(0.05 - 0.1)$ m/s (100 – 200 ppm) at a 95 % confidence level. The operational parameters are those of the USMs, a pressure range of, say, 0 – 250 barg, a temperature range of 0 – 60 °C, and the frequency range 100 – 200 kHz.

Three transient methods are being investigated [2, 4, 5] as part of the work to realize a

precision VOS cell. They are seen to have several similarities, as being transit time based, cancelling out system delay, and the same time detection method may be applied.

One of these methods is presented and used in this paper, as a preliminary method, mainly due to moving parts which is regarded to be a disadvantage in a practical measurement cell. However, the method is flexible and well suited for investigating common experimental aspects and uncertainty sources that also are relevant for the two other candidate methods.

6.2 Theory

6.2.1 The two-distance VOS measurement method

The two-distance VOS measurement method (2DM) is described in e.g. [6, 7], and the principle is shown in Fig. 6.1. In [7] the method was applied on water, and an experimental accuracy of about 205 ppm was achieved.

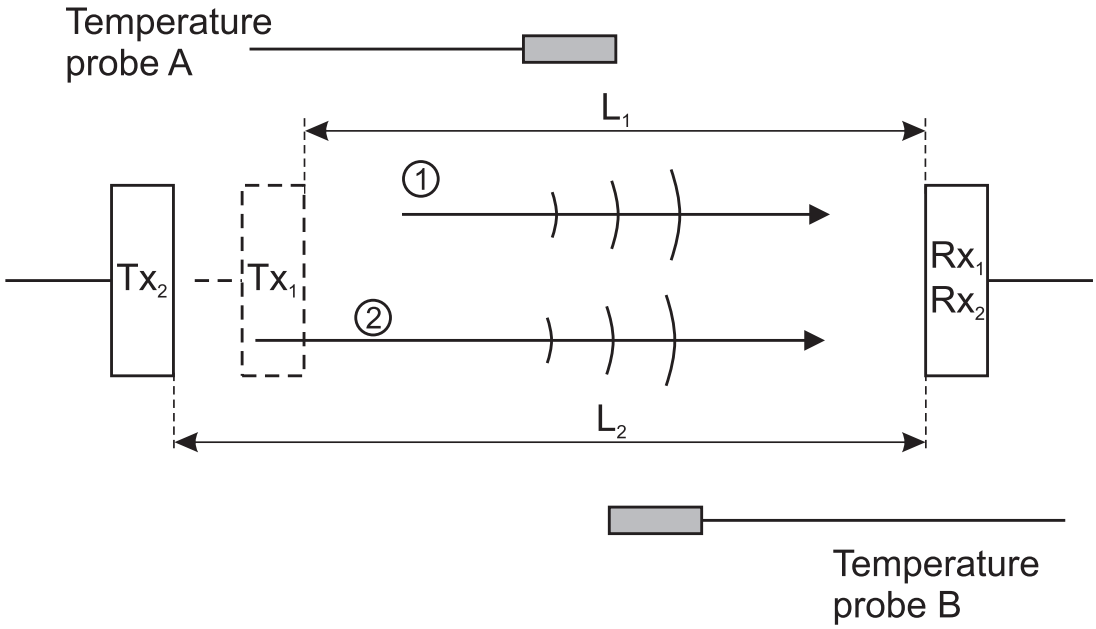

Figure 6.1: Principle sketch of the two-distance method. $Tx_{1,2}$ denotes the transmitted pulse at respective distance 1 and 2, and $Rx_{1,2}$ denotes the received pulse at respective distance 1 and 2.

The measurement principle is as follows (cf. Fig. 6.1): a pulse (1) is transmitted in the gas over the distance L_1, and the total transit time t_1 is measured. The transducer separation is changed by ΔL, and the process is repeated at L_2 to obtain the transit time, t_2, from the second pulse (2).

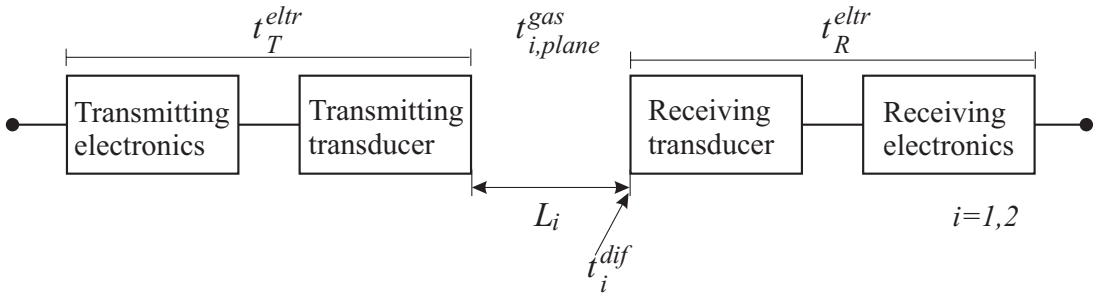

Figure 6.2: A model of the transit time measurement with the two-distance method. Subscript i denotes the measurement at respective distances 1 and 2. t_i^{dif} is the diffraction time advance due to departure from plane wave propagation.

The model in Fig. 6.2 illustrates the system time delay components, and according to this, the following expression represents the measurements at distances L_1 and L_2

$$t_i = t_T^{eltr} + t_{i,plane}^{gas} + t_i^{corr} + t_R^{eltr}, \quad i = 1, 2, \tag{6.1}$$

where t_i denotes the total measured transit time and t_T^{eltr} is the time delay in the transmitting electronics, cables and transmitting transducer. $t_{i,plane}^{gas} = L_i/c$ denotes the plane wave pulse time-of-flight in the gas, and t_i^{corr} accounts for non-ideal effects such as non-plane wave propagation, i. e. diffraction phase shift, t_i^{dif}, and other possible contributions. t_R^{eltr} is the time delay in the receiving transducer, cables and receiving electronics. Note that the time delays in the transmitting and receiving circuits are assumed to be constant throughout the measurements at distances L_1 and L_2 (i.e. not affected by temperature).

By rewriting (6.1) and subtracting t_1 from t_2 we obtain

$$t_2 - t_1 = t_{2,plane}^{gas} - t_{1,plane}^{gas} + t_2^{corr} - t_1^{corr}. \tag{6.2}$$

Now, by introducing $\Delta L \equiv L_2 - L_1$, $\Delta t \equiv t_2 - t_1$ and $t^{corr} \equiv t_2^{corr} - t_1^{corr}$, the VOS, c, may be obtained as

$$c = \frac{\Delta L}{\Delta t - t^{corr}}. \tag{6.3}$$

6.2.2 A VOS model for standard air

A model for VOS in air given in [8] was chosen for comparison due to its extensive empirical support [9, 10, Table II]. A virial equation of state, including first and second virial coefficients was used to develop a pressure dependent model for VOS in standard air. Model input parameters are temperature, pressure, humidity and CO_2 concentration. As an example, at standard temperature and pressure (0 °C and 101 325 Pa) the model predicts a VOS of: $c_0 = 331.46$ m/s ± 300 ppm [8] at a 95 % conf. level, where subscript '0' denotes the zero frequency limit.

The following relation was used to account for dispersion in the medium [8, 11]

$$\frac{1}{c_0} - \frac{1}{c_\phi} = \sum_r \frac{\alpha_r}{2\pi f_r}, \tag{6.4}$$

where c_ϕ is the VOS at a specific frequency and α_r and f_r are the attenuation coefficient and relaxation frequency respectively for each relaxation process. The dominating processes in air are due to nitrogen and oxygen, hence, the model was confined to accounting for these. From (6.4), the dispersion, $\Delta c \equiv c_\phi - c_0$, in the experiments described here was typically 0.15 m/s ($\sim$ 435 ppm), and thus significant.

Although this is a well known dispersion model, little empirical data have been found that may validate the model in the relevant frequency range [8, 11]. The dispersion model uncertainty, $u(\Delta c)$, is thus not determined, but may contribute to the overall model uncertainty. The uncertainty contribution from this dispersion model is therefore omitted, hence, the overall model uncertainty is taken to be 300 ppm [8] (95 % conf. level; see above).

Table 6.1: Measurement parameters.

Parameters	Value
Carrier frequency, f_0 [kHz]	218
Burst wave form	Sine
Peak amplitude [V]	3
Number of periods	50
Burst repetition rate [Hz]	80, 100
Sampling frequency [MHz]	5, 10
L_1, L_2 [cm]	28, 40

6.3 Experimental

6.3.1 Measurement system

A functional diagram of the experimental setup is outlined in Fig. 6.3, and some relevant measurement settings are given in Table 6.1. The transducer separation was adjusted with a linear *Ealing 53-8116/5* positioning stage with a length resolution of 5 μm.

The temperature was acquired from a probe A (T_A), seated just below the acoustic path, and from probe B (T_B), located right below the chamber ceiling. The calibrated, combined temperature uncertainty of the *ASL F250* thermometer and the probes was 13 mK (95 % conf. level).

6.3.2 Environmental conditions

A stationary, low-noise air environment is crucial to achieve high measurement accuracy, and such conditions were attempted obtained by using an insulated chamber enclosing the transducers and positioning system. The walls and ceiling consisted of layered plastic and expanded polyester, covered with a wool carpet on top. The chamber made a closed volume with inner dimensions $52 \times 60 \times 127$ cm^3, well large enough to avoid interfering reflections.

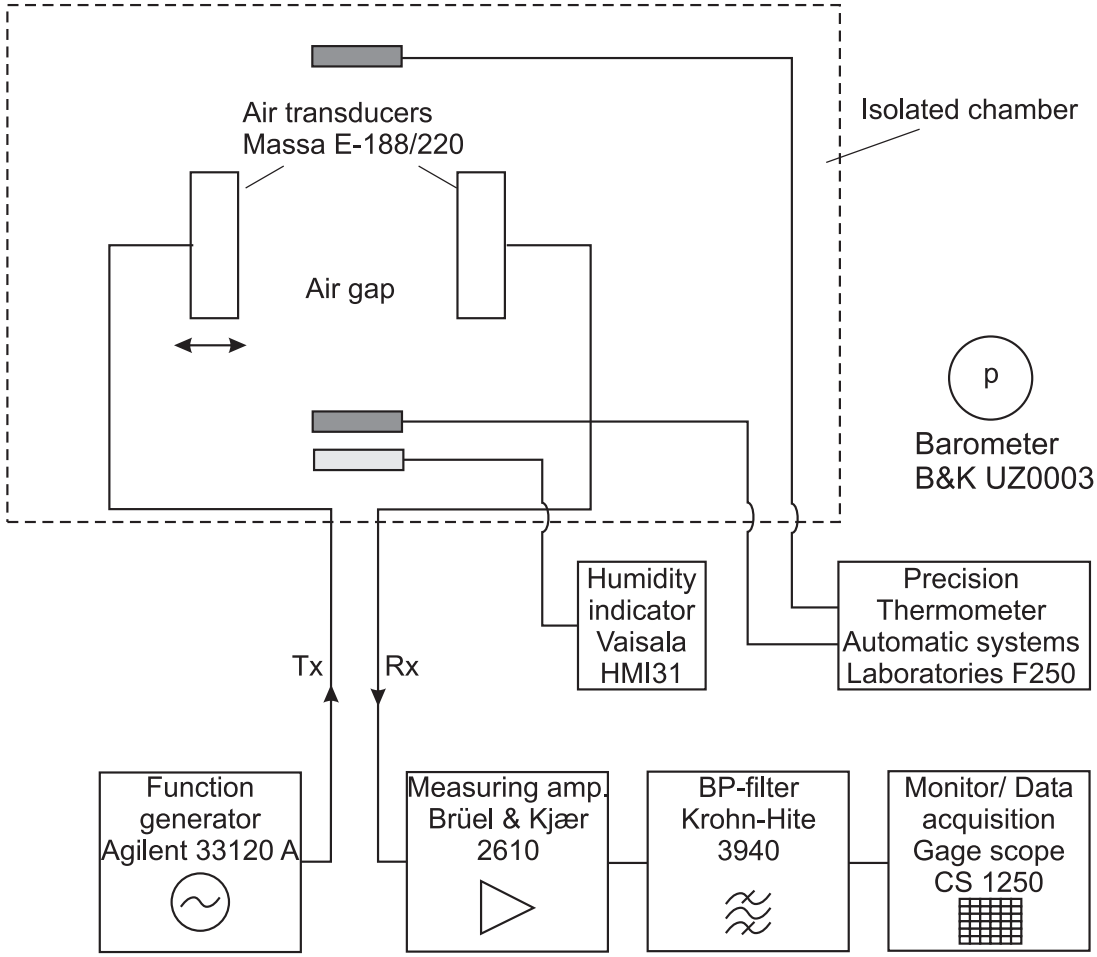

Figure 6.3: Functional diagram of the experimental setup for the 2DM.

Phase shifts detected as rapid changes in the transit times have been observed when either changes or high values in the temperature difference, $\Delta T \equiv |T_A - T_B|$ were present.[1] The phenomenon is experienced to come from medium convection currents, caused by heating from the *Ealing* stage. The problem was also reported in [12], where the same positioning stage was used. To reduce the problem, the stage was insulated and in off-mode until the positioning took place.

[1]Typical values of the temperature difference, ΔT, could be from 30 - 110 mK, with the highest temperature beneath the chamber cealing (T_B).

6.3.3 Data acquisition

Relevant measurement settings were acquired just before the data acquisition, whereas the averaged temperature $\overline{T}_1 \equiv (T_{A1} + T_{B1})/2$ was recorded simultaneously with the acoustic data acquisition in position one. The transmitter was then moved to position two, immediately followed by a second averaged temperature ($\overline{T}_2$) and data acquisition.

The transit time was determined for twenty signal traces, and then averaged to constitute a mean transit time. The zero crossing times in the stationary part of the mean transit time were then averaged to obtain Δt to be input in (6.3).

The transmitted and received burst pulses were recorded with a *GageScope CS1250* (PC-Oscilloscope), with 12 bits sampling resolution. Presumably due to internal PC noise, the effective number of sampling bits were less than 12. By inspecting the level of the short-circuited sampling noise and knowing the range, the effective number of bits could be estimated to 8.4.

6.3.4 Processing

The transit time was determined by zero crossing time detection, combined with linear interpolation between the samples around zero to achieve a sufficient time resolution. By using this method in the stationary part of the burst, the measurand is the phase VOS [13, p. 220] which is the VOS model output as well.

A statistical software [14] was employed to determine the achieved time resolution as a function of sampling frequency (f_s), number of bits, burst periods and generator frequency variation. It was found that $f_s = 5$ MHz, 8 bits, 100 zero crossings and a linear frequency variation of 1 % yielded a standard time uncertainty of 0.14 ns, which is insignificant compared to other quantities. By inspecting the transit time for each zero crossing through the burst, it was found that sampling frequencies exceeding 5 MHz had no impact on the span of the transit time variations.

A threshold was utilized for capturing the burst to determine zero crossings within. Due to medium absorption and long transducer risetime, the signal onset is typically embedded in noise. Consequently, the detected zero crossings of burst (1) may not necessarily correspond to those of burst (2). However, by limiting ΔL, the shape of burst (1) and (2) will be very similar, so by scaling the treshold to the burst amplitude, the zero crossings of the two bursts are likely to correspond.[2]

6.3.5 Corrections

The only identified contribution to the correction term, t^{corr}, in (6.3) was that of a diffraction correction. Williams' model [15] for diffraction correction was used to account for diffraction effects. Model assumptions are that the transmitter oscillates as a plane, circular piston source with a uniform radius, seated in an infinite rigid baffle. This may be a somewhat rude approximation, as the transducers used here probably are designed for fundamental radial mode oscillation [16], and also, the transmitter is not mounted in an infinite baffle.

According to [17], a disc-shaped transducer element can have an effective radius being 40 % smaller than the physical dimension. The effective source radius, a_{eff}, was thus estimated to increase the accuracy of the model input parameters. This was done by adapting the -3 dB angle, θ_{-3dB}, of the piston directivity to the measured directivity, and solving for the radius, resulting in $a_{eff} = 4.25$ mm.

Fig. 6.4 shows the calculated diffraction correction as a function of distance, for the parameters: VOS 345 m/s, source radius 4.25 mm and frequency 218 kHz. t_1^{corr} and t_2^{corr} are marked as a function of the respective distances L_1 and L_2. It is seen that for a pulse travelling a distance like L_1 and L_2, the calculated diffraction time shift becomes a

[2] At the given frequency and VOS, a possible mismatch of one period in Δt gives a perturbation in the VOS of about 4 m/s, which deviates a lot from the model value. The model was thus used to identify erroneous period detection that could arise from the treshold criterion.

significant portion of one period, nearly −85° in the example here.

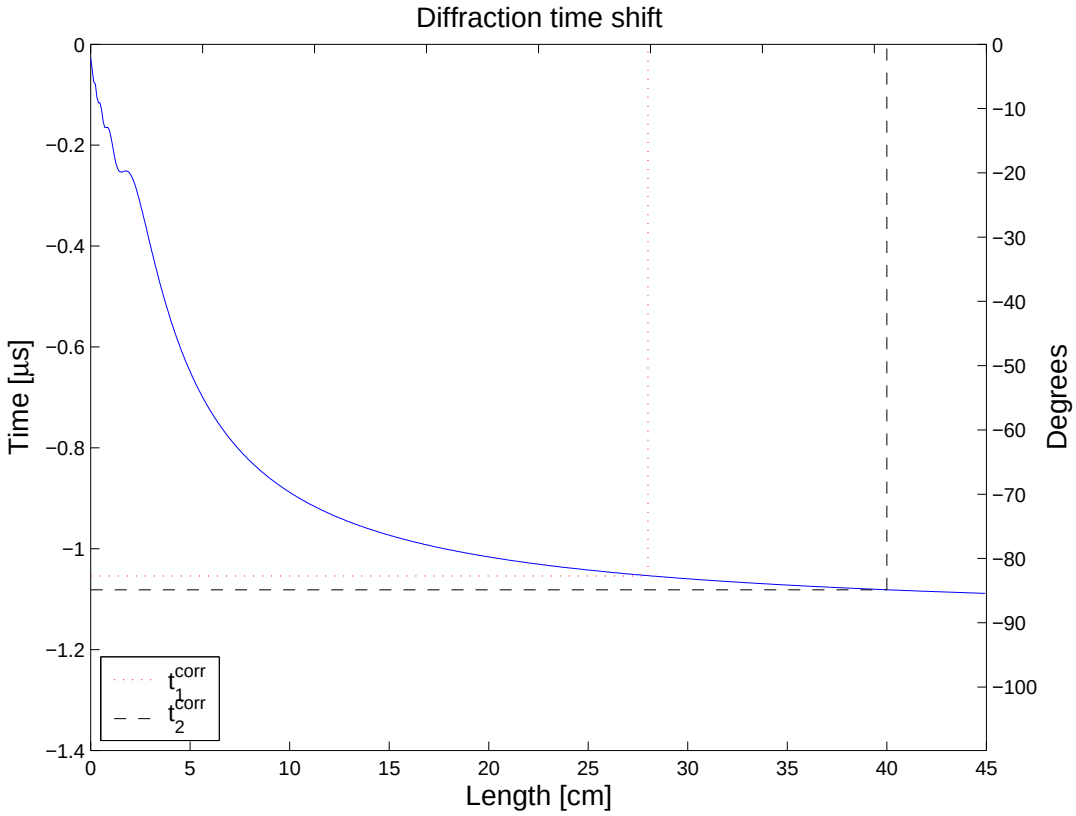

Figure 6.4: Example of calculated diffraction time shift with Williams' model for a plane piston with a VOS of 345 m/s, source radius 4.25 mm and center frequency, $f_0 = 218$ kHz.

It is also evident from Fig. 6.4 that the diffraction correction, t^{corr}, which is the difference between t_2^{corr} and t_1^{corr} can be made relatively small [18] by choosing suitable values for L_1 and L_2. The value of t^{corr} was about 28 ns in the present experiments.

6.4 Results

6.4.1 Sound velocity

The measurement results with estimated uncertainty (cf. Sec. 6.4.2), shown as vertical errorbars, are plotted as a function of temperature in Fig. 6.5, together with the model predictions. The mean and maximum deviation from the model is -18 ppm and -222 ppm

respectively, with a two standard deviation spread of 190 ppm (95 % conf. level), over this temperature range. Hence, the measured VOS values are within the model uncertainty band.

It is stressed that the model uncertainty band possibly should be expanded due to the neglected dispersion model uncertainty, cf. Section 6.2.2. Note also that the "bumps" in the model value / uncertainty band are due to varying air humidity.

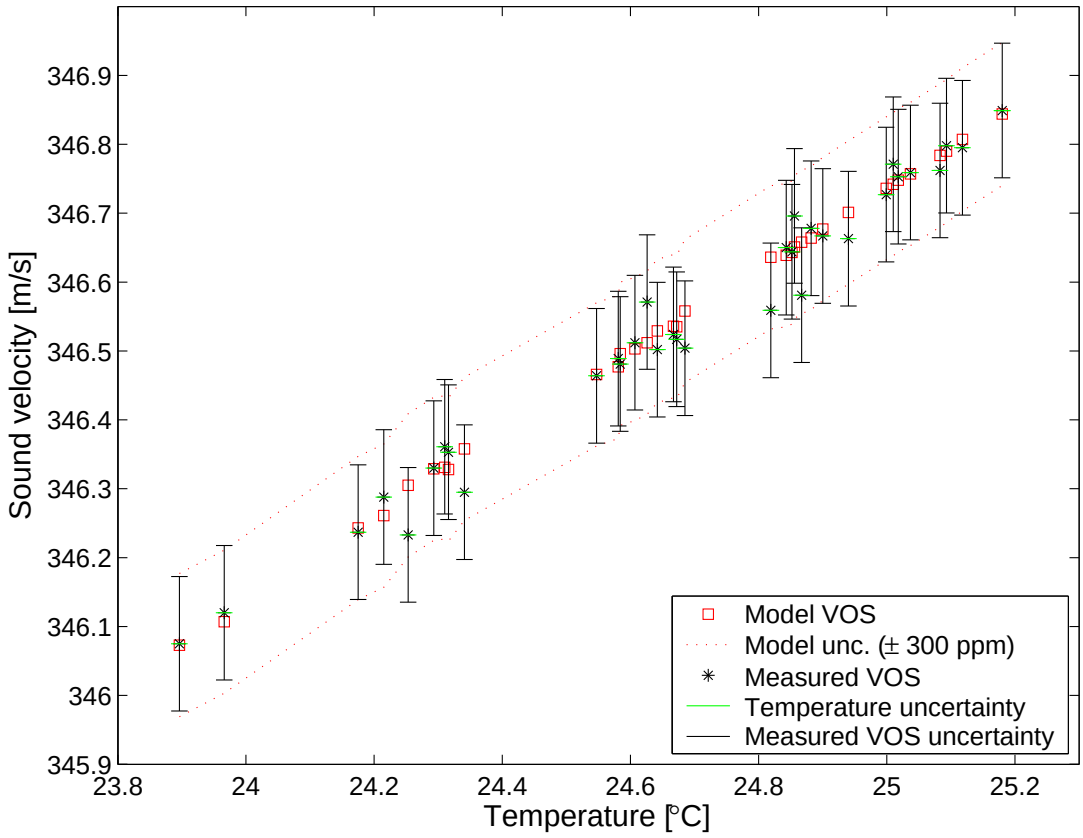

Figure 6.5: VOS measurement results and model predictions. The vertical and horizontal errorbars illustrate the uncertainty in measured VOS and uncertainty in temperature respectively.

6.4.2 Measurement uncertainty

The functional relationship in (6.3) states that $c = c(\Delta L, \Delta t, t^{corr})$. Although Δt and t^{corr} are correlated, they were for simplicity assumed to be uncorrelated, which is a worst case

scenario. Hence, the uncertainty contributions $u(\Delta L)$, $u(\Delta t)$ and $u(t^{corr})$ were combined in a square-root-sum way [19, Eq. (10)].

Dominating uncertainty contributions in $u(\Delta L)$ were temperature expansion and tracking- and positioning accuracy of the positioning stage. Due to insufficient knowledge about the temperature expansion of the positioning stage, and that the measurement temperature was close to the reference temperature[3] stated in the *Ealing* manual, the temperature expansion effect was treated as an uncertainty contribution rather than being corrected for. Additional contributions to $u(\Delta L)$ were identified, but found to be of insignificant importance. $u(\Delta L)$ was estimated to 5 μm at a 67 % confidence level.

The two dominating uncertainty components in $u(\Delta t)$ were phase shift due to medium convection currents and non-linearity, with respective uncertainty contributions of about 28 ns and 9 ns (67 % conf. level). The combined uncertainty in $u(\Delta t)$ was estimated to 42 ns at a 67 % confidence level. If the convection currents could be avoided, then the relative, estimated uncertainty in $u(\Delta t)$ would presumably be reduced to 37 ppm (67 % conf. level)

The correction term uncertainty, $u(t^{corr})$, is difficult to evaluate (cf. Sec. 6.3.5). It is expected that any departure from the plane piston diffraction model will be approximately equal for t_1^{corr} and t_2^{corr} well into the farfield. As $t^{corr} = t_2^{corr} - t_1^{corr}$, these deviations should thus be nearly cancelled out. $u(t^{corr})$ was estimated to 20 ns (67 % conf. level).

The expanded measurement uncertainty was estimated as recommended in [19] to 282 ppm (95 % conf. level). The experimental uncertainty budget is outlined in Table 6.2.

[3]The temperature for which the performance figures of the positioning stage are stated.

Table 6.2: Experimental uncertainty budget.

Relative quantity	Value [ppm]
$u(\Delta L)/\Delta L$	43
$u(\Delta t)/\Delta t$	121
$u(t^{corr})/\Delta t$	58
Combined uncertainty, $u(c)/c$	141
Expanded uncertainty, $U(c)/c$ (conf. level 95 %)	282

6.5 Discussion and conclusions

Table 6.2 shows that the experimental uncertainty is dominated by $u(\Delta t)$, for which the major contributor are medium convection currents. By avoiding the heating from the positioning stage and having a proper temperature control, the relative uncertainty in $u(\Delta t)$ would presumably be estimated to 37 ppm (67 % conf. level), and the expanded experimental uncertainty would be about 162 ppm. Obtaining this should be practically feasible, and note that no moving parts are intended in the planned VOS cell.

The uncertainty contribution from nonlinear effects is also expected to be reduced in a well designed measurement cell facility. The *GageScope* used here put some restrictions on maximum number of signal traces that could be stored for averaging, and in addition, the measurement facility used here is not optimized for suppressing noise, like a properly designed measurement cell would. The transducer driving voltage is thus expected to be reduced in a measurement cell, yielding a linear system operation.

The present work is considered to be preliminary in the sense that it aims to investigate important aspects and uncertainty sources relevant for the three methods [6, 7, 2, 4]. Particularly the uncertainty in transit time difference is affected e.g. by the time detection method and system stability, and these parameters are crucial also for the other two transient methods.

If both the convection currents and nonlinear effects could be reduced as outlined above, then the uncertainy in the time detection appears to be the least significant uncertainty contribution, with a relative, estimated uncertainty of only 14 ppm. This should indicate a fair potential for using this time detection method in one of the candidate cell methods, besides that the system stability should be sufficient.

A major challenge with the other two candidate methods is the diffraction correction, which will be much greater than here, and thus needs to be more carefully modelled than in the present case. A prototype measurement cell is now being deviced to test the potential of the two candidate methods on gases like e.g. argon and nitrogen.

Acknowledgment

The present work is part of a Ph.D project under the 4-year strategic institute programme (SIP) *Ultrasonic technology for improved exploitation of oil and gas resources* (2003-2006) at Christian Michelsen Research AS, supported by the Research Council of Norway (NFR), Statoil ASA and Gassco AS. The SIP is carried out in a cooperation with the University of Bergen, Dept. of Physics and Technology (UoB).

Steinar Vervik developed the transducer stages and measurement chamber as part of his Dr. Scient work [12].

Bibliography

[1] P. Lunde and K.-E. Frøysa, "Mass and energy measurement of gas using ultrasonic flow meters," in *Proc.* 25^{th} *Scandinavian Symposium on Physical Acoustics, Ustaoset, Norway, 27-30 January 2002*, U. R. Kristiansen, Ed., Scientific/Technical Report No. 420103. Trondheim, Norway: Norwegian University of Science and Tecnology, Dept. of Telecommunications, June 2002, CD issue only, ISSN 1501-6773.

[2] P. Lunde and M. Vestrheim, "Precision sound velocity cell for natural gas at high pressures. Phase 1 — feasibility study." Christian Michelsen Research AS, Bergen, Norway, Tech. Rep. CMR-98-F10039 (Confidential), Dec. 1998.

[3] P. Norli, P. Lunde, and M. Vestrheim, "Methods for precision sound velocity measurements in pressure cells for gas characterization," in *Proc.* 27^{th} *Scandinavian Symposium on Physical Acoustics, Ustaoset, Norway, 25-28 January 2004*, U. R. Kristiansen, Ed. The Norwegian Physical Society, June 2004, CD issue only, ISBN: 82-8123-000-2.

[4] H. Suzuki, H. Tanaka, and H. Hachisuka, "Method and apparatus for ultrasonic wave measurement," US Patent 6.094.987, August 2000.

[5] P. Norli, "Comparison of three methods for precision sound velocity measurement of gases," in *Proc.* 28^{th} *Scandinavian Symposium on Physical Acoustics, Ustaoset, Norway, 23-26 January 2005*, U. R. Kristiansen, Ed. The Norwegian Physical Society, August 2005, CD issue only, ISBN: 82-8123-000-2.

[6] A. Z. Golik, Y. I. Kuzovskov, and V. Y. Nagin, "Pulse equipment for the measurement of ultrasound absorbtion coefficient and speed in liquids under high pressure," *Akustika i Ultrazvukovaya Tekhnika (Kiev)*, vol. 247, pp. 184–189, 1989.

[7] R. Brooks, "Determination of the velocity of sound in distilled water," *J. Acoust. Soc. Amer.*, vol. 32, pp. 1422–1425, 1960.

[8] O. Cramer, "The variation of the specific heat ratio and the speed of sound in air with the temperature, pressure, humidity and CO_2 concentration," *J. Acoust. Soc. Amer.*, vol. 93, pp. 2510–2516, 1993.

[9] M. Greenspan, "Comments on "speed of sound in standard air" [J.Acoust.Soc.Am. 79, 1359-1366 (1986)]," *J. Acoust. Soc. Amer.*, vol. 82, pp. 370–372, 1987.

[10] G. S. K. Wong, "Speed of sound in standard air," *J. Acoust. Soc. Amer.*, vol. 79, pp. 1359–1366, 1986.

[11] G. P. Howell and C. L. Morfey, "Frequency dependence of the speed of sound in air," *J. Acoust. Soc. Amer.*, vol. 82, pp. 375–377, 1987.

[12] S. Vervik, "Methods for characterization of gas-coupled ultrasonic sender-receiver measurement systems," Dr. Scient thesis. University of Bergen, Dept. of Physics, Bergen, Norway, 2000.

[13] J. P. M. Trusler, *Physical Acoustics and Metrology of Fluids.* Bristol, England: Adam Hilger, 1991.

[14] Personal communication with Kjell-Eivind Frøysa, Christian Michelsen Research AS, Bergen, Norway, 2004.

[15] A. O. Williams, "The piston source at high frequencies," *J. Acoust. Soc. Amer.*, vol. 23, pp. 1–6, 1951.

[16] S. Vervik, "Transitt-tidsbestemmelse for ultralyd strømningsmetre. Nullstrømningsforhold," Cand. Scient thesis. University of Bergen, Dept. of Physics, Bergen, Norway, 1995, In norwegian.

[17] R. C. Chivers, L. Bosselaar, and P. R. Filmore, "Effective area to be used in diffraction correction," *J. Acoust. Soc. Amer.*, vol. 68, pp. 80–84, 1980.

[18] P. Lunde, K.-E. Frøysa, and M. Vestrheim, "Transient diffraction effects in ultrasonic flow meters for gas and liquid," in *Proc.* 26^{th} *Scandinavian Symposium on Physical Acoustics, Ustaoset, Norway, 26-29 January 2003*, U. R. Kristiansen, Ed., Scientific/Technical Report No. 420304. Trondheim, Norway: Norwegian University of Science and Tecnology, Dept. of Telecommunications, June 2003, CD issue only.

[19] "Guide to the expression of uncertainty in measurement," First edition, International Organization for Standardization, Geneva, Switzerland, 1995, ISBN: 92-67-10188-9.

Chapter 7

Paper B

Diffraction correction for a piezoelectric ultrasonic gas transducer using finite element modelling

Authors:

Petter Norli and Per Lunde

Reformatted version of the paper submitted to:

IEEE Transactions on Ultrasonics, Ferroelectrics, and Frequency control, as of April 12 2007.

Abstract

It is well known that accurate correction for transducer diffraction effects may be necessary for precise sound velocity measurements. In connection with work on a high-precision sound velocity cell for natural gas at high pressures, the following questions have been raised: (a) how accurate is the traditionally used plane piston diffraction correction model for the different vibration modes of the transducer, and (b) can this plane piston diffraction correction model be used for the commercial transducer employed in the measurements, at the operational frequency used in the measurements, 218 kHz, in spite of a possible non-piston-like vibration pattern of the transducer?

In the present work, these two questions are investigated using a finite element model (FEM) for diffraction correction of non-uniformly vibrating piezoelectric transducers. Results using the plane piston diffraction correction model are compared with results using the FEM diffraction correction model for a tentative construction model of the transducers.

Measurements and FEM calculations show that,—in spite of the general poor ability of the plane piston model to describe the transducer, the plane piston diffraction correction model may still provide a reasonably accurate description for the transducers for the measurement configuration in question, at the operational frequency and distance used in the sound velocity measurements, provided an effective piston radius approach is used.

In certain frequency ranges outside the operational frequency band of the transducer, the results show significant deviations between the FEM and plane piston diffraction correction models, both with respect to phase and magnitude. Better and more controlled investigations are feasible and necessary to precisely explain the deviations between the two diffraction correction models, and relate them to measured effects for real transducers.

7.1 Introduction

When high accuracy is required in ultrasonic measurement methods, correction for diffraction effects associated with the ultrasonic transducers may need to be accounted for [1, 2, 3, 4, 5, 6, 7, 8, 10, 11, 12, 13, 14, 15, 16, 17, 18]. Consider a source transducer, and a receiving transducer located at the sound axis of the source, facing the source. When measuring the sound field as a function of axial distance, and absorption has been corrected for, a result is obtained which depends on distance. That is, a deviation is obtained both for the amplitude and phase relative to what one would obtain if the sound field were a plane wave field. Traditionally, one has tried to describe this effect using the diffraction correction model proposed by Williams [1] and Khimunin [13, 14], using the model for a plane circular piston mounted on a flat rigid baffle of infinite extent, vibrating with uniform velocity normally to the radiating surface [19] (hereafter referred to as "the plane piston model"). In the diffraction correction model proposed in [1, 13, 14], which will be referred to as "the plane piston diffraction correction model", the sound pressure in the fluid at the location of the receiver is averaged over a plane surface corresponding to the receiver front area, A, and denoted $\langle p \rangle_A$, cf. Eq. 3.13 below.

This traditional and frequently used approach is—for several reasons—not correct. Firstly, the sound field from a real transducer is in general not described very accurately by the sound field given by the plane piston model. This is related to the calculation of the function $\langle p \rangle_A$, that the piston model sound field used as input to $\langle p \rangle_A$ may not be a correct sound field. Secondly, the interaction with the receiving transducer and the distance dependency, is not as simple as described in such a model. This is related to the fact that use of the function $\langle p \rangle_A$ itself, as proposed in [1, 13, 14], may not be quite correct. The resulting sound signal is a result of reception over the complete transducer, also at the sides and possibly the back, and not just at the front face. In the far field such effects are accounted for by the receiving sensitivity. However, as the receiver is moved into the near field of the source, and the sound field starts to deviate from a plane wave field, such effects may change. This is to be accounted for in a correct model for diffraction correc-

tion. The first of these two items is addressed here. The second item is not discussed further in the present work.

Classical examples where transducer diffraction effects need to be addressed and corrected for are e.g. precise measurements of the attenuation and sound velocity in fluids and solids [1, 13, 14], involving the magnitude and phase of the transducer diffraction, respectively. Other examples include transducer calibrations, ultrasonic custody transfer metering of gas (volumetric, mass and energy flow rate metering) [20, 21, 22, 23, 24], and sound velocity cells for gas characterization [25, 26, 27, 28].

In [26, 27, 28, 29], a commercial, piezoelectric ultrasonic air transducer has been applied to evaluate candidate measurement methods for a precision sound velocity cell for natural gas at elevated pressures. In this work, transducer diffraction effects and high control with the correction for such effects, appear to be among the most critical factors in order to realize a high precision measurement cell.

In [26, 27, 28, 29], transducer diffraction effects were corrected for in a simplified manner, using the plane piston diffraction correction model [1, 13, 14]. However, the transducer used in the sound velocity measurements does not necessarily vibrate uniformly as a piston at all it's vibration modes, raising the questions (a) how accurate is the plane piston diffraction correction model for the different vibration modes of the transducer, and (b) can the plane piston diffraction correction model be used for this transducer at the operational frequency used in [26, 27, 28, 29], 218 kHz, in spite of a possible non-piston-like vibration pattern of the transducer at this frequency?

In the present work, these two questions are investigated using a finite element model (FEM) for diffraction correction of non-uniformly vibrating piezoelectric transducers proposed and described in [24, 30, 31]. Results using the plane piston diffraction correction model [13, 14] are compared with results using the FEM diffraction correction model for

a tentative construction model of the commercial transducer used in [26, 27, 28, 29].

In this approach, the FEM diffraction correction model proposed in [24, 30, 31] is expected to provide a more realistic description for the transducer used in [26, 27, 28, 29] than the plane piston diffraction correction model. To add some confidence to this approach, FEM simulation results are also compared with measured electrical and acoustical transducer properties of the transducer, to (a) illustrate that the transducer does not in general vibrate uniformly as a plane piston, and (b) indicate that the FEM results—although suffering from unknown constructional details of the transducer—may still provide a reasonable representation of the transducer.

Note that a precise agreement of the FEM and measurement results cannot be expected (and is not needed), as knowledge of construction details, materials used, material data and dimensions for the transducer construction in question have been unavailable for the study. The purpose is thus not to accurately model the actual transducer and its properties, but to demonstrate that the FEM simulation results agree qualitatively with the measurement results. That is, to form a basis for using FEM for calculating diffraction correction for the transducer, as an improvement to investigate the accuracy of using the simplified plane piston diffraction correction model approach for this transducer.

The influence of some analytical vibrational source profiles on the diffraction correction was studied in [11]. It was found that deviations from the plane piston source profile had appreciable effect on the diffraction correction, and should be accounted for whenever high accuracy is required.

A numerical model for diffraction correction was developed in [16], based on a discretization of the source and receiver, which were assumed to be two-dimensional circular arrays that may differ in radius and be non-coaxially aligned. The source may vibrate with a non-uniform magnitude and phase profile, and the receiver may have a non-uniform magnitude

and phase sensitivity across the aperture. In addition, the medium may be attenuating. However, significant idealization lies in the assumption that the transducer pair consists of two planes, as sound radiation from the sides and rear of the source transducer is omitted.

The FEM diffraction correction model described in [24, 30, 31] has several similarities with that in [16]: The source may differ in radius from the receiver and have non-uniform sensitivity across the front face, the medium may be attenuating, and the receiver is a two-dimensional plane. In addition, the FEM diffraction correction model extends the model of [16] by fully modelling the source as an axisymmetric piezoelectric transducer, extended axially as a real transducer. Hence, radiation due to realistic vibrational modes of a piezoelectric transducer construction is included, as well as radiation contributions from the sides and back of the source transducer body.

The paper is organized as follows. In Section II, the plane piston and FEM diffraction correction models are described briefly, with emphasis on the mathematical expressions used. Finite element modelling of the transducer used in [26, 27, 28, 29] is described in Section III. The experimental measurements are described in Section IV. Measurement and simulation results of the transducer properties are given in Section V, followed by a comparison of the diffraction correction results for FEM and the more traditional plane piston model in Section VI. Discussion and conclusions are given in Sections VII and VIII, respectively.

7.2 Diffraction correction

7.2.1 The plane piston diffraction correction model

Consider a sound source in a fluid medium, coaxially aligned to a receiving plane as shown in Fig. 7.1. Harmonic time variation $e^{\nu\omega t}$ is assumed, and suppressed in the following. Khimunin [13] defined a diffraction correction function, H^{dif}, for a simplified case, where

a uniformly vibrating plane piston radiates sound to a coaxial circular receiver, given as

$$H^{dif} \equiv \frac{\langle p \rangle_A}{p_{pl}}, \tag{7.1}$$

where $\langle p \rangle_A$ is the sound pressure in the fluid, averaged over a circular plane corresponding to the receiver front area A, in absence of the receiver (i.e. the free-field pressure); p_{pl} is the plane wave pressure at the center point of the receiver, in absence of the receiver, having the same particle velocity as the piston source in the plane piston model.

If the source is seated in a plane infinite rigid baffle, vibrates like a plane circular piston with uniform velocity, and transmits sound to a coaxially aligned circular receiver with equal diameter, Eq. (7.1) becomes [13, 14, 1]

$$H^{dif} = 1 - \frac{4}{\pi} \int_0^{\pi/2} e^{\imath kz \left[1 - \sqrt{1 + \left(\frac{2a}{z} \cos\theta\right)^2}\right]} \sin^2\theta \, \mathrm{d}\theta, \tag{7.2}$$

where θ is an integration variable, $k = 2\pi/\lambda$ is the loss-free wave number, λ is the acoustic wavelength, z is the source – receiver distance, and a is the piston source and receiver radius.

7.2.2 The finite element diffraction correction model

The model description below follows that in [24, 30, 31], but is briefly repeated here for completeness. The definition in Eq. (7.1) is still applied, but has now been extended to include a three-dimensional axisymmetric source transducer with arbitrary vibration pattern, cf. Fig. 7.1. Thus, source contributions from the entire transducer volume may contribute to the sound field. $\langle p \rangle_A$ is here the sound pressure in the fluid radiated by this transducer, averaged over a circular plane corresponding to the receiver front area, A, in absence of the receiver (i.e. the free-field pressure).

Now, to evaluate H^{dif} (Eq. (7.1)), the pressure is averaged over the receiver area A by

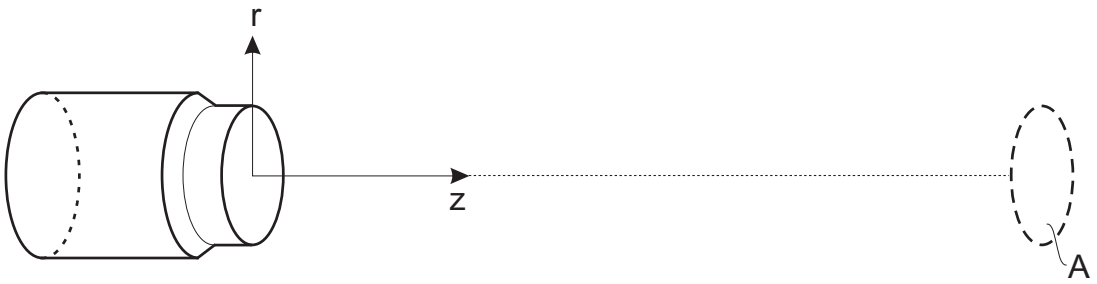

Figure 7.1: Axisymmetric coordinate system for the diffraction correction model used in FEM. Origin is taken at the center of the source front, and A denotes the area of the receiver's front face.

taking [24, 30, 31]

$$\langle p \rangle_A \equiv \frac{1}{A} \int_A p(r,z) \mathrm{d}A, \tag{7.3}$$

where $p(r,z)$ is the free field pressure in the fluid, calculated by FEM, in absence of a receiving transducer.

The plane wave pressure, p_{pl}, is calculated as follows. In the distant far field it is assumed that the non-uniformly vibrating source essentially produces a spherical and directive wave, which is propagated back to the source front using the axial farfield expression for the plane piston model [19]. An "equivalent uniform piston velocity" is then obtained from the axial far field pressure, p_{ff}, as [24, 30, 31]

$$v_0^{eq} = p_{ff} \frac{2z_{ff}}{\imath \rho c \hat{k} a_{eq}^2} e^{\imath \hat{k} z_{ff}}, \tag{7.4}$$

where v_0^{eq} is the normal velocity amplitude on the surface of a hypothetical plane piston source of radius a_{eq}; z_{ff} is the axial far-field distance at which p_{ff} is calculated (set somewhat arbitrarily to 1000 m in the present work), ρ is the fluid density, c is the sound velocity, and $\hat{k}$ is the complex wave number accounting for losses.

The equivalent plane wave sound pressure may then be calculated for the receiver distance z as [24, 30, 31]

$$p_{pl} = \rho c v_0^{eq} e^{-\imath k z}. \tag{7.5}$$

Equations (7.3) and (7.5) are then inserted into Eq. (7.1).

7.3 Finite element modelling

7.3.1 The finite element model

The finite element model used here is specially designed for ultrasonic piezoelectric transducers (FEMP) [32, 33, 34], and capable of modelling the transducer as an axisymmetric structure with a piezoelectric disk, front layer, backing layer and housing, surrounded by a fluid medium or vacuum [33].

The piezoelectric disk and elastic layers are modelled using piezoelectric and elastic finite elements, respectively, of type 8 node quadratic isoparametric axisymmetric elements [33, 34]. The inner and outer part of the fluid medium is modelled using fluid finite elements, and 10^{th} order infinite wave envelope elements [33], respectively.

7.3.2 Transducer modelling

The transducer used in [26, 27, 28, 29] and subject to study here is manufactured by *Massa Products Corporation* and denoted *Massa E-188/220*, henceforth abbreviated *mas*. It is primarily designed for operation in atmospheric air around 220 kHz [35].

Constructional details, materials and used precise dimensions have unfortunetaly not been available for the present study. One thus had to rely on a tentative model for the transducer, shown in Fig. 7.2.

Based on inspection [36], the structure appears to consist of a matching layer in front, adjacent to a piezoelectric disk, with a soft backing layer at the rear, cf. Fig. 7.2b. A metal housing, reduced in diameter toward the circular front, bounds the structure radially and at the back.

In the tentative construction model for the transducer used here, the matching layer was taken to be silicone rubber, the material of the piezoelectric disk was tentatively taken to be *PZT-5A* from *Morgan Matroc Ltd.* [37], whereas the backing layer was assumed to consist of two compressed cylinders of light foam rubber. The housing material was taken to be steel. The dimensions of the piezoelectric disk and matching layer of the transducer sample measured in [36] were taken as starting points in the present work, but slightly tuned to match the measured transducer properties.

The following assumptions were made for the transducer model

1. Influence of electrodes and glue can be neglected;

2. the rear seal of the metal housing can be neglected;

3. the ramp-like constriction of the housing toward the front (cf. Fig. 7.1) may be replaced by a step-like constriction; and

4. non-axisymmetrical modes are of insignificant importance.

Effects of the transducer holder used in the measurements were neglected in the simulations, which may be questioned, since interference with and radiation from the holder may possibly contribute to the measured sound field.

The material parameters given in Table 7.1 were chosen to provide a reasonable overall agreement with measurement results for the simulated transducer properties (electrical and acoustical). The silicone and foam rubber data were chosen in the typical range of such materials. In Table 7.1, c_l and c_s are the compressional and shear wave velocities, and Q_l and Q_s are the compressional and shear wave quality factors (accounting for losses).

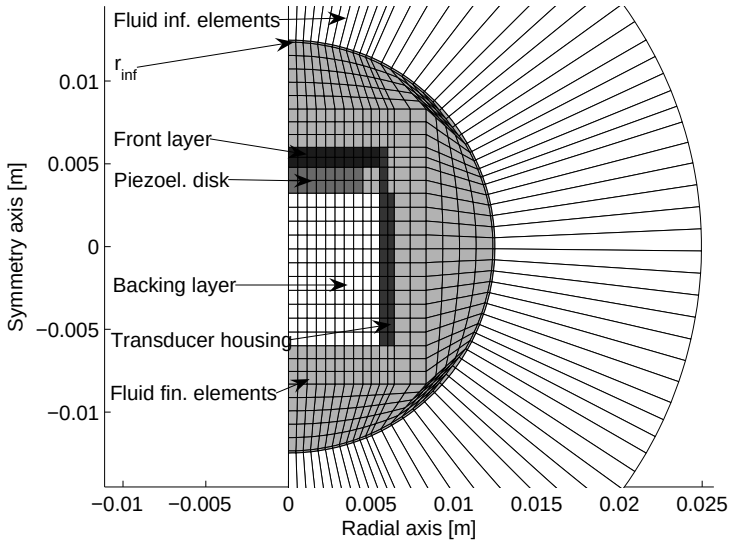

(a) The axisymmetric FEM transducer model shown with reduced mesh resolution for visibility. Notice the increased radial resolution through the structure to obtain sufficient pressure resolution for calculating diffraction correction (cf. Sec. 7.3.3). The gap between the piezoelectric disk and housing is fluid. The circle with radius $r_{inf} = 12.48$ mm separates the fluid finite and infinite elements.

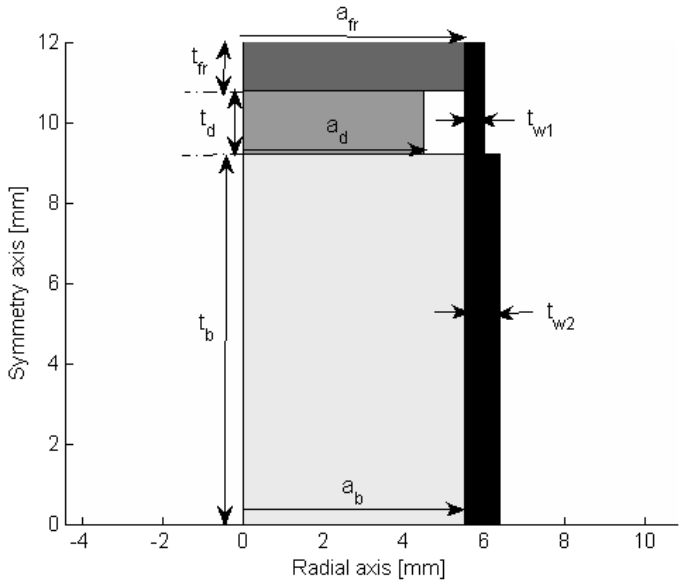

(b) The subscripts b, d, fr and w refer to backing, disk, front layer and wall, respectively. The dimensions of the model are as follows: $a_{fr} = 5.5$ mm, $a_d = 4.5$ mm, $t_{fr} = 1.21$ mm, $t_d = 1.57$ mm, $t_b = 9.22$ mm, $t_{w1} = 0.5$ mm and $t_{w2} = 0.9$ mm.

Figure 7.2: Outline of the FEM transducer model in subplot (a), with dimensions given in subplot (b).

Table 7.1: Material parameters used in the transducer model. Material data for PZT-5A [37] were tentatively used for the piezoelectric disk.

Material	c_l [m/s]	c_s [m/s]	ρ [kg/m^3]	$Q_l = Q_s$
Front: silicone rubber	1020	379	950	30
Backing: foam rubber	1000	302	100	5
Housing: steel [19]	6100	3372	7700	100

7.3.3 Numerical considerations

In a convergence test on FEMP [33], it was found that the axial pressure error is minimum at the normalized distance, $S_{inf} = r_{inf}\lambda/a^2 = 0.32$ for the present type of infinite elements. Hence r_{inf} was set so as to yield $S_{inf} = 0.32$.

Another important parameter affecting the numerical accuracy is the number of elements per shear wavelength, n_p. In [38] the far-field axial pressure relative to that of a plane piston radiator in an infinite rigid baffle was investigated for $ka = 30$, which seems relevant for our case, where $ka = 18$ (218 kHz). A relative numerical error of about 0.2% and 1.5° was found for the magnitude and phase, respectively, given $n_p = 5.7$, which is the coarsest resolution used here.[1] This may give a rough estimate of the numerical uncertainty in the source sensitivity, S_V, cf. Sec. 7.4.2.

Figure 7.2a indicates that the radial resolution in the infinite elements decreases with distance. To compensate for this, and maximize the resolution over the receiver area A (cf. Eq. (7.3) and Fig. 7.1), n_p was set to 8 in the radial direction within the transducer structure [39]. The current mesh resolution was limited by the PC memory.

A simplified convergence test was performed on the diffraction correction results by varying n_p from 4 to 5 for the axial distance 15 cm. For the frequency band 150 – 270 kHz, the magnitude and phase discrepancies are less than 0.1 dB and 0.5°, respectively, and beyond this frequency range the similar figures are 0.35 dB and 2.9°, respectively.

[1] The coarsest part of the mesh had $n_p = 5$ in the axial direction at a frequency of 340 kHz, corresponding to $n_p \approx 5.7$ at the maximum frequency used here, 300 kHz.

7.4 Experimental

7.4.1 Electrical admittance measurements

Input electrical conductance (G) and susceptance (B) measurements were carried out for the transducer in atmospheric air at a temperature of about 25 °C, using a *Hewlett Packard 4192A* impedance analyzer.

7.4.2 Source sensitivity measurements

The voltage source sensitivity measured here is defined by: $S_V \equiv p_{z=1m}/V_{in}$, where $p_{z=1m}$ is the peak pressure measured 1 m axially from the transducer front, and V_{in} is the peak input voltage at the source terminals. In the current work, the pressure was measured at 20 cm distance (using a *Brüel & Kjær 4138* (1/8") microphone) and extrapolated to 1 m.[2] Effects of absorption were removed according to [40]. The experimental setup is shown in Fig. 7.3, and the temperature and relative humidity of the atmospheric air medium were typically about 25 °C and 25%, respectively, during the measurements.

Previous S_V measurements have indicated nonlinear effects in the transducer, or air medium, for transducer drive levels beyond 1 V_{pp}, around the operational frequency of 218 kHz, which limits the allowed drive level. On the other hand, measuring outside the operational frequency range requires an SNR as high as possible. The nonlinearity effects are considered acceptable for drive levels below 4 V_{pp} (at 218 kHz), so it was decided to use 30 V_{pp} for frequencies below 50 kHz; 20 V_{pp} for the ranges 50 – 150 kHz and 267 – 300 kHz; and 4 V_{pp} for the 151 – 266 kHz range.

Due to unavailable microphone calibration data beyond 200 kHz, the value at 200 kHz was used also for the 200 – 300 kHz range. Obviously, the measurement uncertainty in this frequency range is considerable.

[2] A microphone distance of 20 cm corresponds to the normalized distance $S = z\lambda/a_d^2 \approx 11$ at the maximum frequency, 300 kHz.

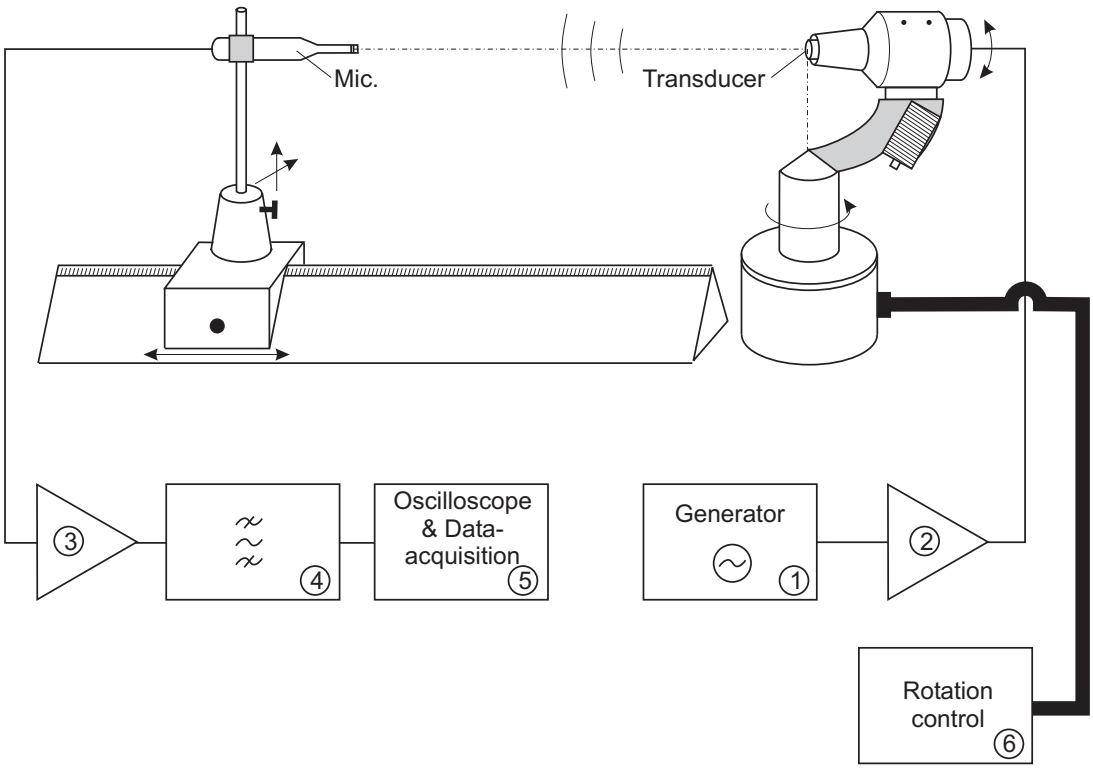

Figure 7.3: The experimental setup for the sensitivity and directivity measurements; cotton was wrapped around the transducer and microphone stage (not shown) to avoid acoustical air-borne interference. A measurement chamber of plastic served to suppress air-flow effects. The instruments are denoted as follows: ① *function generator HP33120A*; ② *20 dB custom design amplifier*; ③ *Brüel & Kjær Measuring amplifier 2610*; ④ *Krohn-Hite BP-filter 3940*; ⑤ *oscilloscope GageScope CS1250*; and ⑥ *Ealing rotary stage 37-0379*.

7.4.3 Directivity measurements

A similar experimental setup as for the S_V measurements was used for the directivity measurements (cf. Fig. 7.3), including the measurement distance and dynamic drive level. The temperature and relative humidity of the atmospheric air medium were in the same range. The source transducer was assumed to point at the 0° direction when its angular alignment gave maximum received signal level.

7.5 Transducer property results

In the following, FEM simulated directivity results for some of the transducer vibration modes are compared with directivity results using the plane piston model, as a basis for evaluating and discussing the diffraction correction results, cf. Secs. 7.6 and 7.7. The FEM simulated vibration modes of the transducer are also shown, to indicate to which degree a close directivity agreement is linked to a close vibration pattern agreement or not, for the piston model and transducer at hand.

In addition, comparisons are made with the measured directivity and the electrical admittance and source sensitivity responses of the two *mas* transducers, to investigate to which extent the transducer construction under study (cf. Fig. 7.2),—in spite of all the unknown construction details (cf. Secs. 7.1 and 7.3.2)—may still provide a reasonable representation of the transducer used in [26, 27, 28, 29].

7.5.1 Measured and simulated electrical admittance

The measured electrical input admittance of two transducer samples named *masA* and *masB* are compared with FEM simulation in Fig. 7.4.
Basically, both measurement and simulation results exhibit a double peak structure. The simulated peak centered around 225 kHz is in better agreement with measurements than that centered around 197 kHz, which in the simulations is located about 10 kHz lower than in the measurements. Moreover, several tiny peaks appear in the simulations as opposed to the measurements. The discrepancy is expected to be due to the limited knowledge of the detailed transducer construction and the associated material data.

7.5.2 Measured and simulated source sensitivity

Measured and simulated source sensitivity S_V results are shown for masA and masB in Fig. 7.5. Note that in the simulations the transducer holder has not been accounted for, whereas in the measured results effects of the holder may possibly be present.

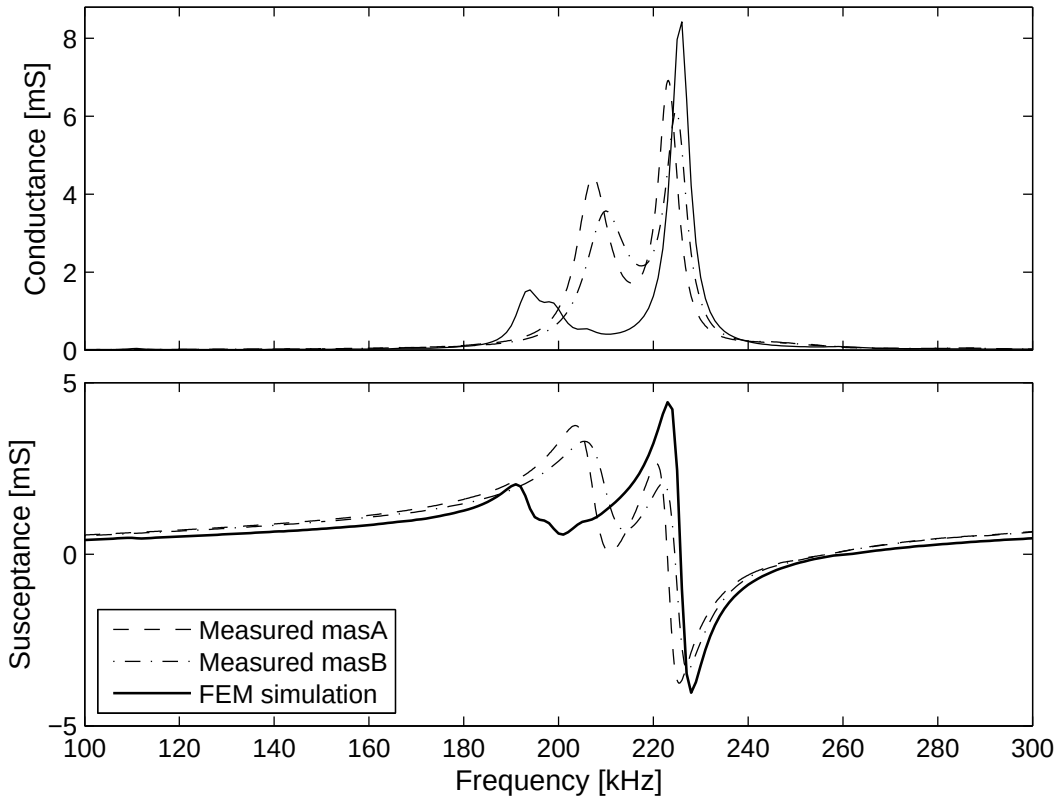

Figure 7.4: Measured and simulated electrical conductance and susceptance results, respectively, for *masA* and *masB* in atmospheric air.

In the frequency region below 100 kHz, the simulation results exhibit various dips and peaks that are absent in the measurements. The discrepancies are discussed in Sec. 7.7.

In the frequency region 100 – 190 kHz, a reasonable qualitative correspondence with the measurements is found; a peak is apparent at about 110 kHz for both measurement and simulation results, however, it is significantly stronger in the simulations. The FEM results roughly follow the tendency of the measurements, but the simulated sensitivity is basically much higher than the measured in the region 140 – 190 kHz.

Around 200 kHz, three peaks are visible in the simulations, in contrast to the measurements, where only one peak appears, situated about 10 kHz higher in frequency. The lower resonance frequency of these three peaks in the simulations may possibly explain

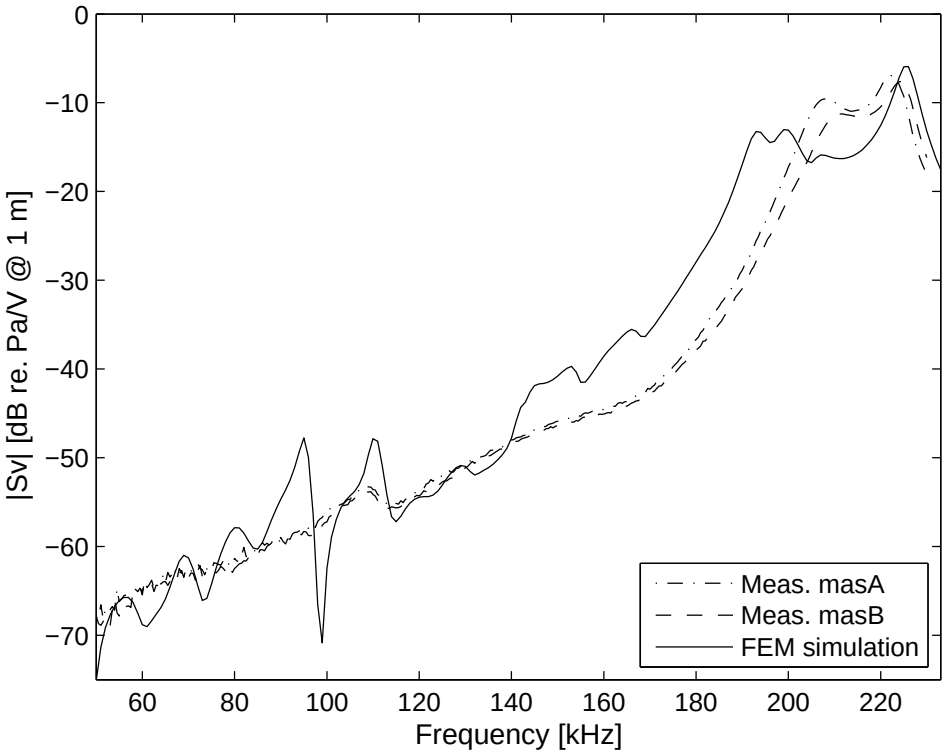

Figure 7.5: Measured and simulated source sensitivity magnitude for masA and masB transducers, in air at 1 atm. and room temperature.

the considerable discrepancy with the measured sensitivity level in the 140 – 190 kHz range, as the trend of the measurements fits well with the simulations, and the lower resonance frequency contributes to raise the sensitivity level below the peaks.

For the 210 – 230 kHz range, the simulated peak around 224 kHz is in fair agreement with the measurement results, both with respect to frequency and level.

7.5.3 Measured and simulated directivity, and simulated vibration pattern

Due to the difficulties in precise comparison with measurements (cf. Sec. 7.1), the FEM calculated directivity of each mode was compared to measurements at both the measurement frequency and at adjacent frequencies, to check for possible deviation in frequency

with respect to at which frequency the mode occurs. The simulated directivity was evaluated at $z = 1$ m, as opposed to the measurement distance of 20 cm. This was however not found to affect the simulation results significantly. As the masA transducer became defect during the measurements, it was replaced with another, denoted masC. The plane piston directivities [19] outlined in this section were calculated using the piezoelectric disk radius of the transducer model, $a_d = 4.5$ mm (cf. Fig. 7.2b).

FEM simulated vibration patterns of the transducer model are also shown below, as snapshots taken at maximum outward displacement, exaggerated between $5 \cdot 10^4$ and $40 \cdot 10^4$ times, depending on the mode. Both directivities and vibration patterns are displayed for some selected frequencies.

Results at 58 kHz

Figure 7.6a shows the vibration pattern, and a piston-like movement is seen for the central part of the front face (like a "vibrating plateau"). Relatively strong waves are apparent in the backing layer.

The FEM directivity results shown in Fig. 7.6b are in very good agreement with the measurements over the central part of the main lobe ($\pm 20°$), with deteriorating agreement for increasing opening angles. For the same angular range, there is close correspondence between the plane piston and FEM directivity.

Results at 81 kHz

Figure 7.7a shows the simulated vibration pattern, and again, a vibrating plateau is apparent, as is also the strong vibrations in the backing layer.

The measured directivity in Fig. 7.7b agrees well with the FEM simulation for angles within $\pm 10°$; and in the same angular range, good agreement between FEM and the plane piston directivity is observed. The agreement is however deteriorating with greater

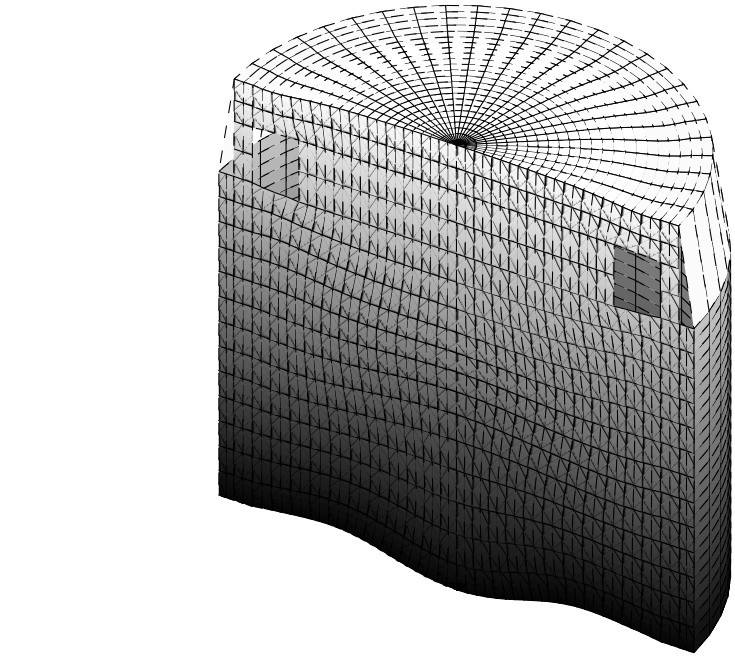

(a)

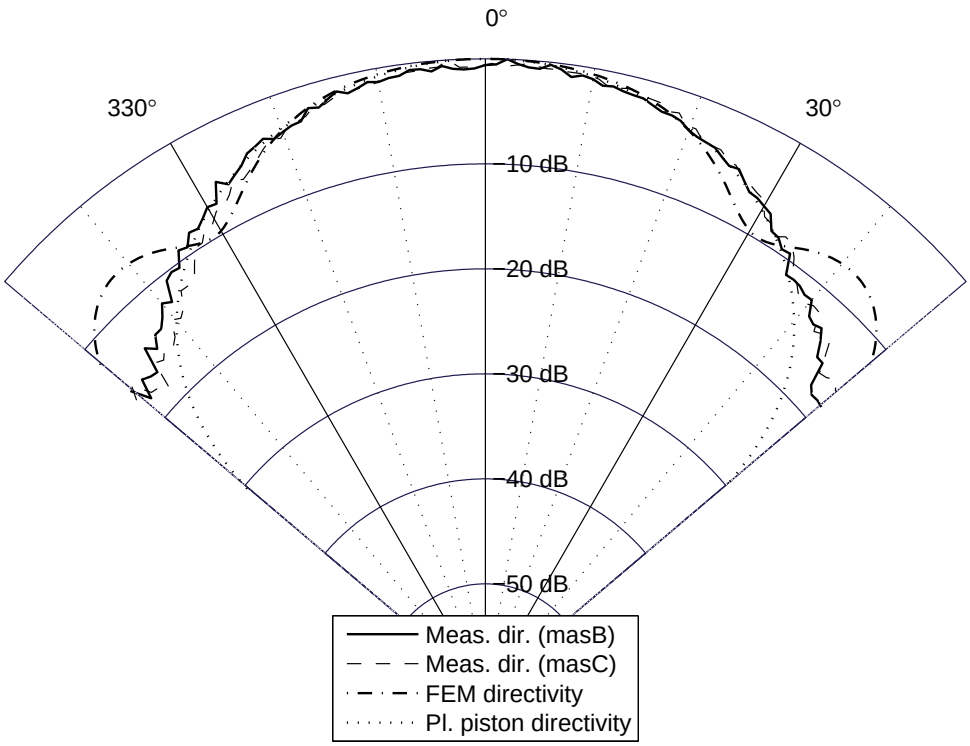

(b)

Figure 7.6: The vibration (a) and directivity (b) pattern of the transducer at 58 kHz.

angles.

Results at 99 kHz

Figure 7.8a shows the simulated vibration pattern, and the front face vibrates in a manner where the central and peripherical regions are in opposite phase, i.e. very unlike a plane piston source.

At this frequency, there is a distinct dip in the FEM simulated directivity in the 0° direction, cf. Fig. 7.8b, deviating considerably from the measured directivity. Similar (but weaker) dips appear in the FEM directivity at the frequencies 27, 49, 61 and 74 kHz (not shown here), corresponding closely to the frequencies associated with the dips in S_V, cf. Fig. 7.5.

The FEM beam is also very different from the plane piston directivity.

Results at 163 kHz

The simulated vibration pattern, shown in Fig. 7.9a, appears to be highly complex over the front face. The vibrations in the backing layer are now, presumably due to the reduced acoustic wavelength, significantly reduced.

The FEM directivity exhibits in this case too narrow a main lobe compared to the measurements; a good correspondence is only found within the angular range ±5°. There is however very good match between the FEM and plane piston directivity over the main lobe. As for the side lobes of the models: at about ±25°, the plane piston directivity exhibits significantly stronger side lobes than FEM, and contrary, around ±45° the FEM side lobe level is appreciably stronger than the plane piston level.

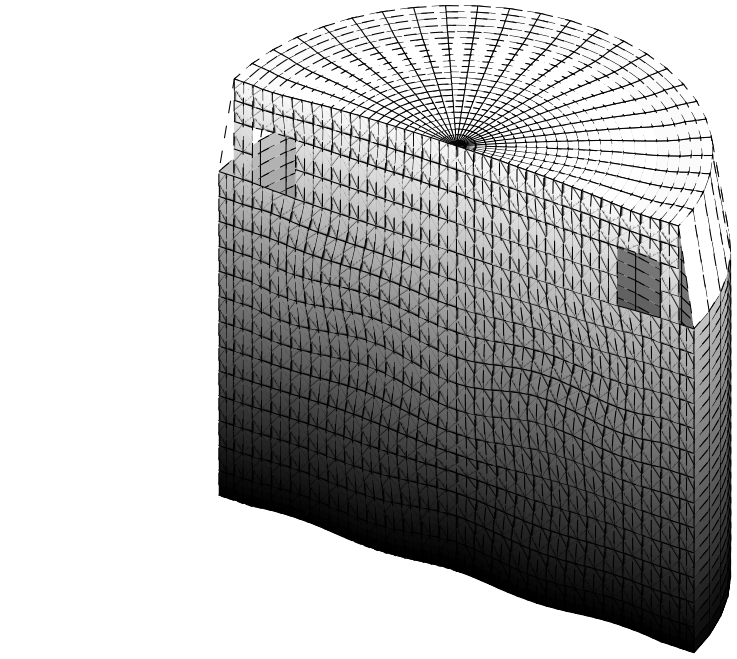

(a)

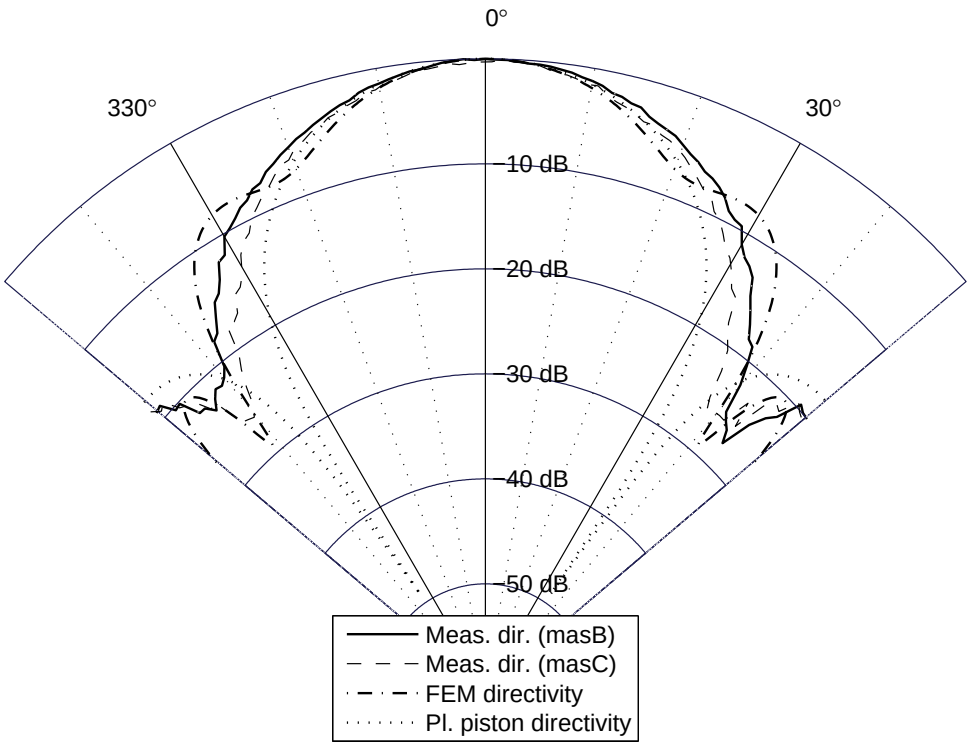

(b)

Figure 7.7: The vibration (a) and directivity (b) pattern of the transducer at 81 kHz.

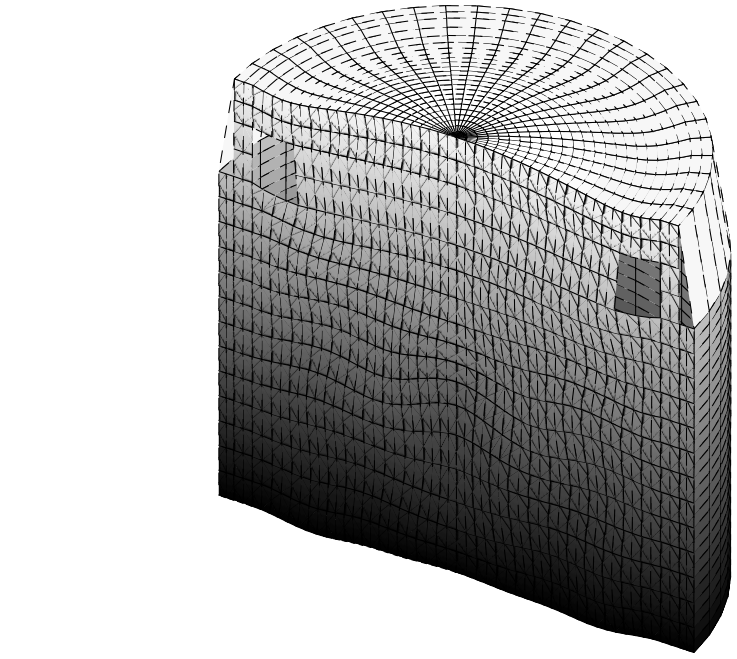

(a)

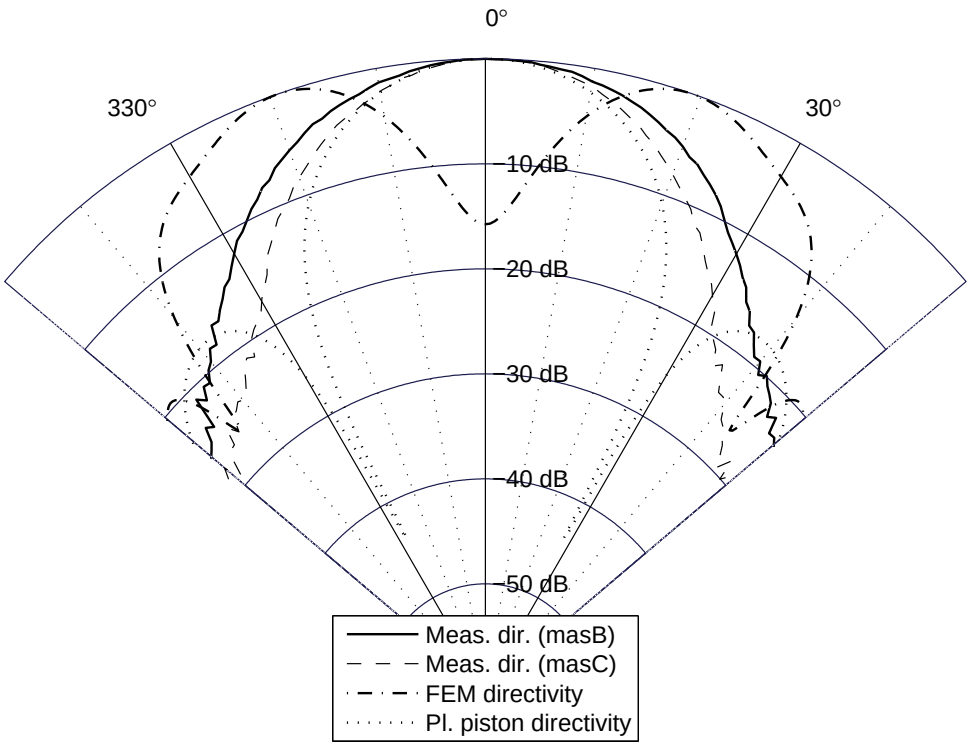

(b)

Figure 7.8: The vibration (a) and directivity (b) pattern of the transducer at 99 kHz.

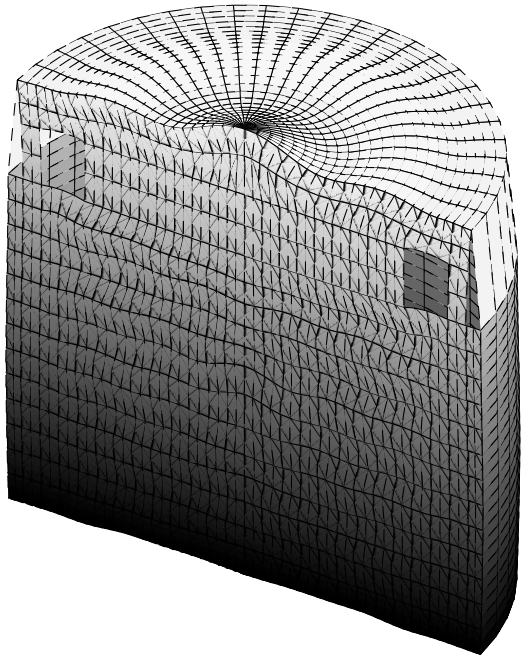

(a)

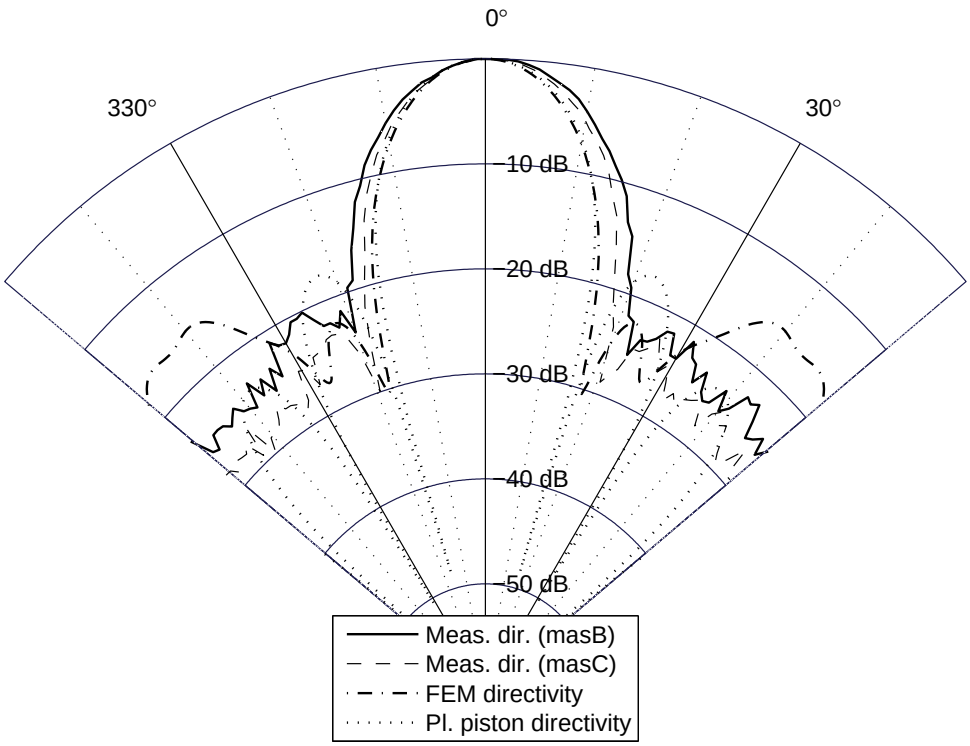

(b)

Figure 7.9: The vibration (a) and directivity (b) pattern of the transducer at 163 kHz.

Results at 180 kHz

The FEM simulated vibration pattern, shown in Fig. 7.10a, is very complex, possessing several nodes across the front face.

Regarding the directivity pattern, shown in Fig. 7.10b, a reasonable correspondence is found between the FEM and measured directivity over a sector of about $\pm 40°$; however, outside this range the FEM directivity exhibit rather strong side lobes (around $\pm 50°$), which are not present in the measurements. The plane piston directivity deviates significantly from that of FEM, as it has a narrower main lobe, and much stronger primary side lobes.

Results at 198 kHz

Figure 7.11a shows the FEM simulated vibration pattern for the transducer model, and again, a plateau-like outward displacement is seen for the front face.

Regarding the directivity results shown in Fig. 7.11b, FEM corresponds closely to the measurements within a beam sector of about $\pm 13°$. However, the FEM main lobe expands with increasing opening angle. This may be due to merged main and primary side lobes, a feature which is not present in neither of the measurements. The FEM side lobe level is in reasonable agreement with the measurements. The plane piston directivity corresponds well with the FEM directivity only within, say $\pm 5°$; elsewhere the plane piston directivity is significantly more narrow. Also, the side lobe levels are stronger.

Results at 218 kHz

The simulated vibration pattern of the transducer model is shown in Fig. 7.12a, for which a bowl-like vibration pattern is noted for the front face.

The FEM directivity, cf. Fig. 7.12b, is in quite good agreement with the measurements over the main lobe, and a reasonably fair agreement is found for the first side lobe.

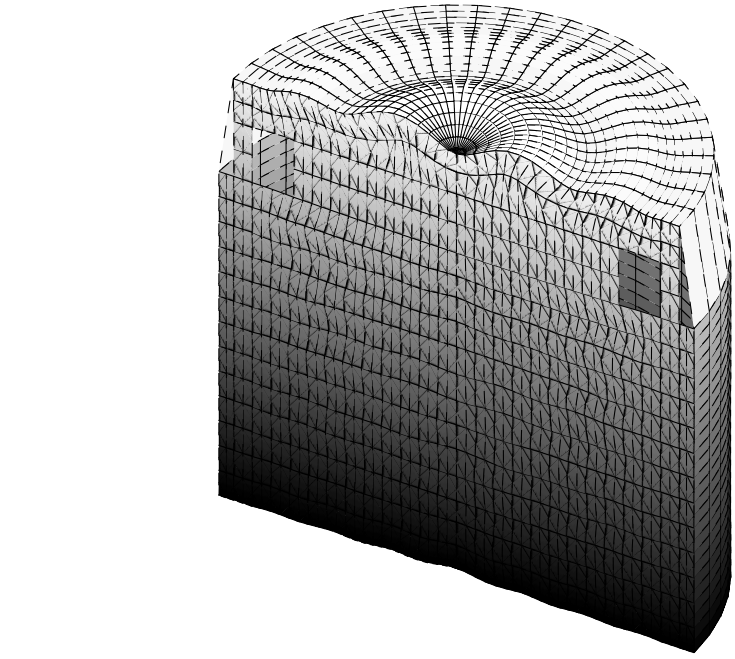

(a)

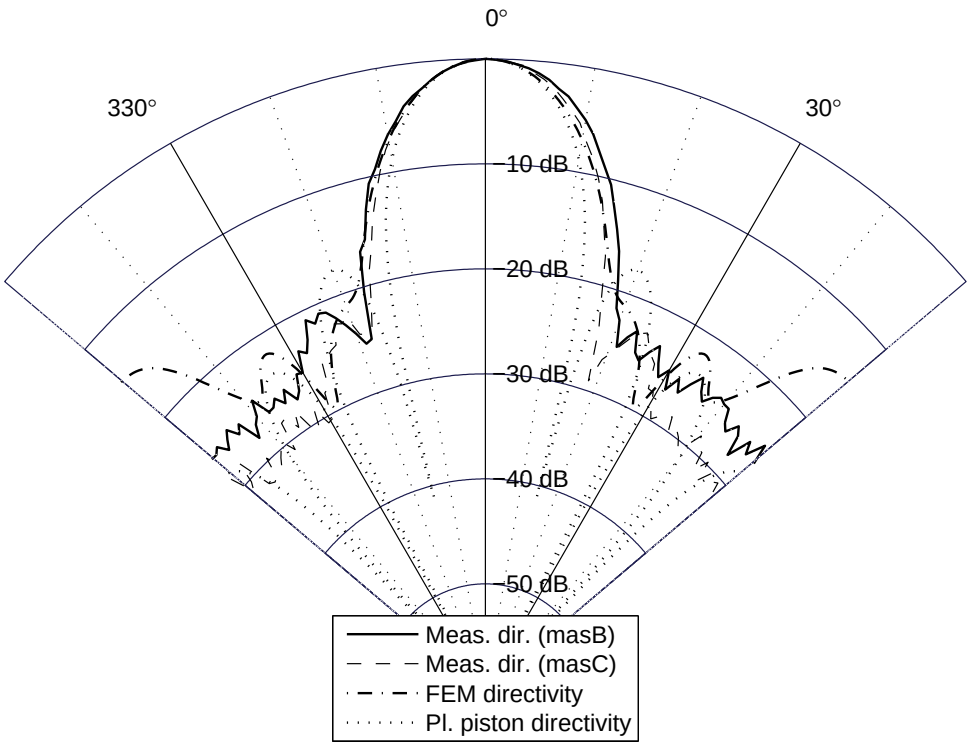

(b)

Figure 7.10: The vibration (a) and directivity (b) pattern of the transducer at 180 kHz.

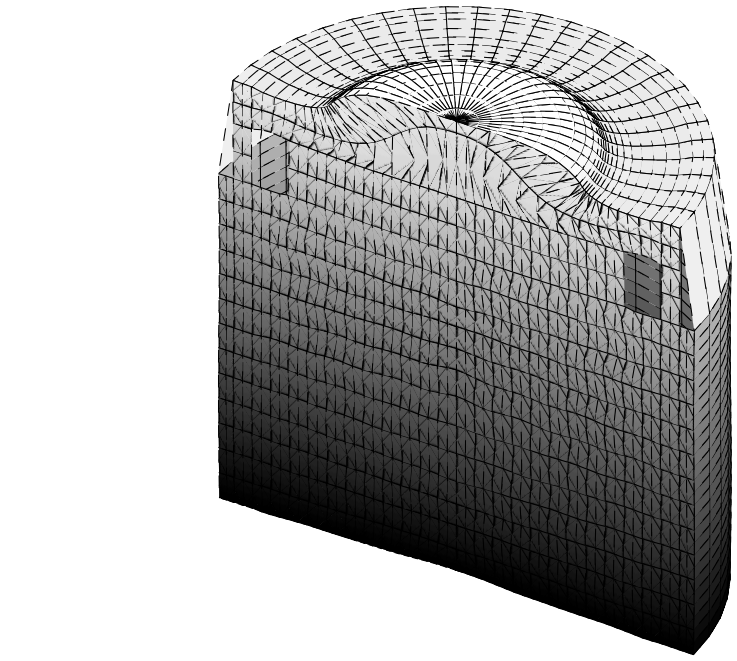

(a)

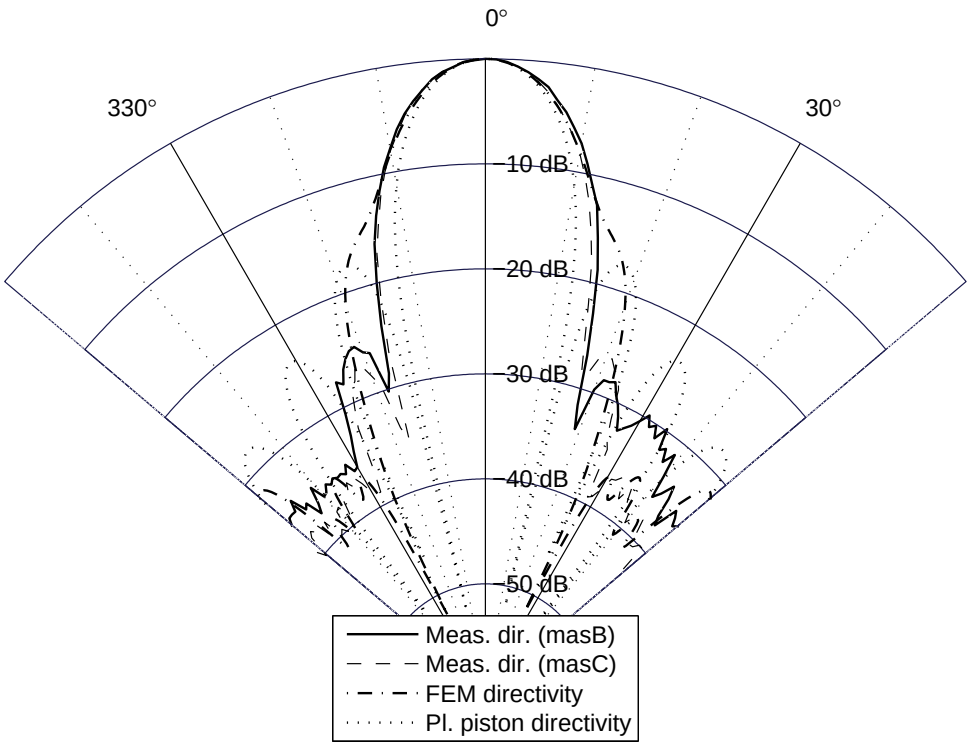

(b)

Figure 7.11: The vibration (a) and directivity (b) pattern of the transducer at 198 kHz.

Also, despite of the considerable disparity in vibration pattern between the front face of the FEM model (Fig. 7.12a) and that of a plane piston, they match reasonably well with respect to the central part of the main lobe directivity, say within $\pm 5^\circ$ (cf. Fig. 7.12b). Outside this range however, the plane piston directivity is significantly more narrow than FEM, and in addition, the side lobes of the former model are appreciably stronger than measured.

Results at 300 kHz

The FEM vibration pattern is now highly complex, cf. Fig. 7.13a.

Figure 7.13b shows the directivities at 300 kHz, and clearly there is great discrepancy between the two transducers in this frequency range. Hence, there is little utility in comparing FEM and measured directivity. This indicates that the manufacture spread of the transducer samples have increased impact on the transducer properties in this frequency range.

The correspondence between the FEM and plane piston directivity is poor for the entire beam range, in particular the main lobe of FEM is significantly more narrow than that of the plane piston model.

7.6 Diffraction correction results

The main objective of the present work, as pointed out in Sec. 7.1, is to investigate how representative the plane piston diffraction correction model is for the transducer in question. The present section outlines a comparison of the FEM and plane piston diffraction correction model results, calculated using the approach described in Secs. 7.2.1 and 7.2.2, respectively.

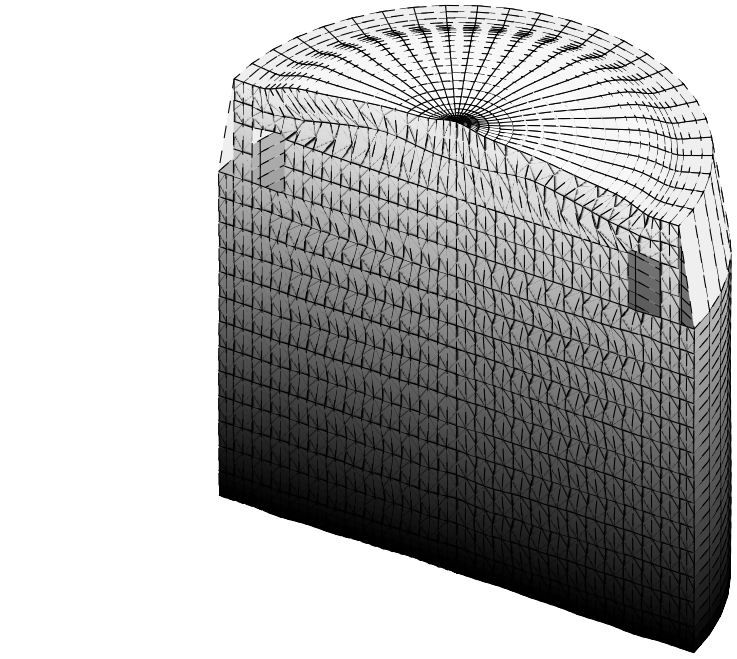

(a)

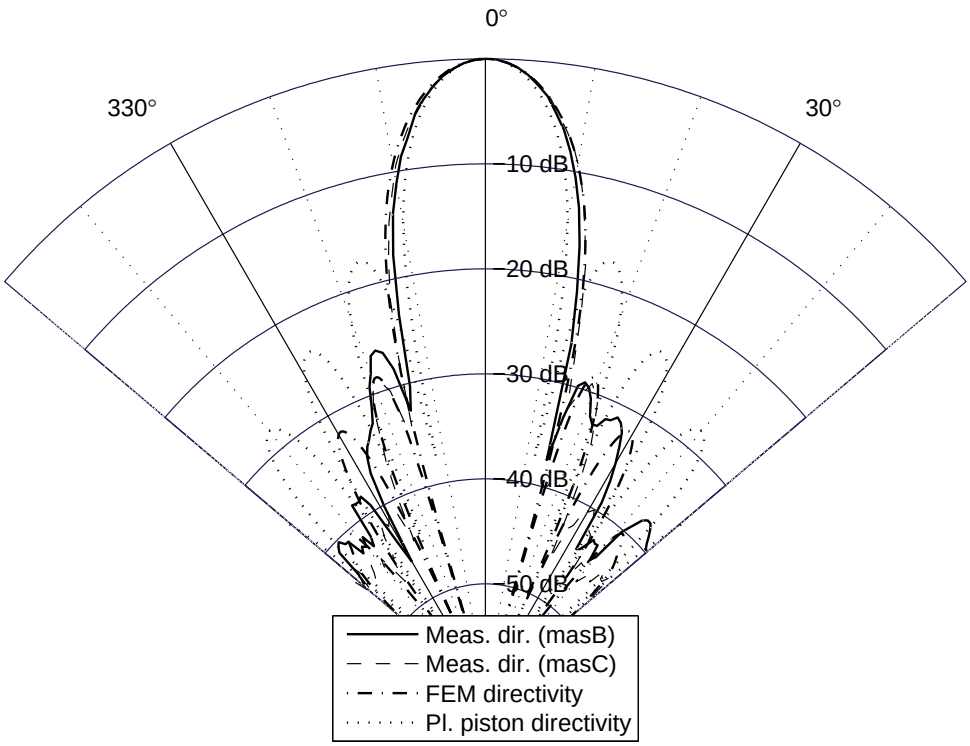

(b)

Figure 7.12: The vibration (a) and directivity (b) pattern of the transducer at 218 kHz.

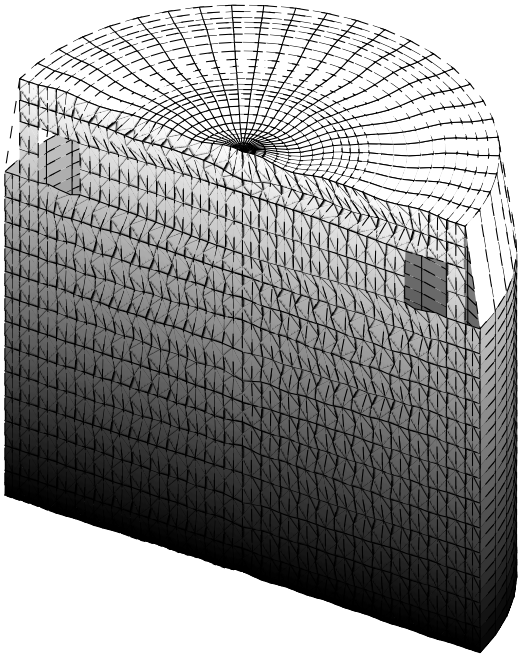

(a)

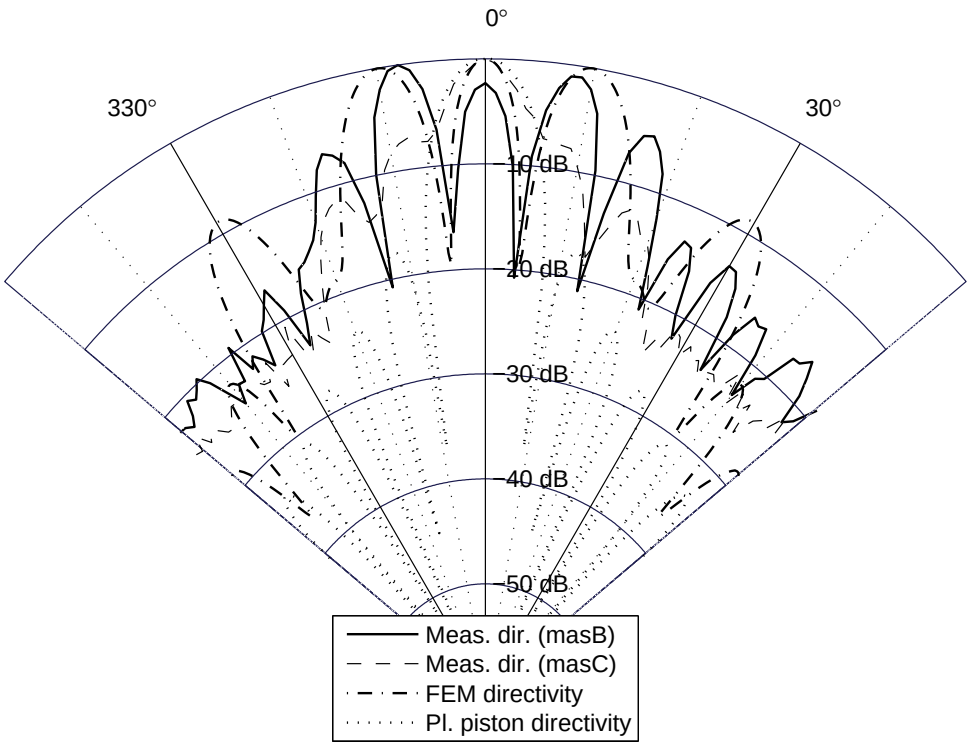

(b)

Figure 7.13: The vibration (a) and directivity (b) pattern of the transducer at 300 kHz.

7.6.1 Diffraction correction versus frequency

Consider the magnitude and phase of the diffraction correction, shown in Figs. 7.14a and 7.14b, respectively. The plane piston diffraction correction calculations were performed using the effective source transducer radius, a_{eff}, which has been estimated experimentally [26] to 4.25 mm (evaluated for the present transducer at 218 kHz).

It has been found that in the low frequency limit, say below 10 kHz, both the FEM and piston directivity tend to be very broad; this leads to a quite close agreement between the two diffraction correction models, both with respect to magnitude and phase (as the receiver becomes relatively small).

In the frequency range 10 – 150 kHz, various strong deviations between the two diffraction correction models are observed, both with respect to magnitude and phase. These are most distinct at 25, 50, 99 and 115 kHz. The cause of these deviations is discussed in Sec. 7.7.

In the frequency range 150 – 270 kHz, the two diffraction correction models agree to within 1.4 dB and 2.8° with respect to magnitude and phase correction, respectively.

In the 270 – 300 kHz range, the discrepancy between the diffraction correction models increases, cf. Sec. 7.7.

7.6.2 Diffraction correction versus distance

In Fig. 7.15, the FEM and plane piston diffraction correction model results are plotted as a function of distance, at the operational frequency 218 kHz, given the radius a_{eff}. Attention is paid to the distance 15 cm, which is considered relevant for the precision sound velocity cell for gas [26, 27, 28, 29], and which—at least in the context of diffraction correction—is located in the transition zone between the near field and the far field.
Both for the magnitude and phase of the diffraction correction, a significant deviation

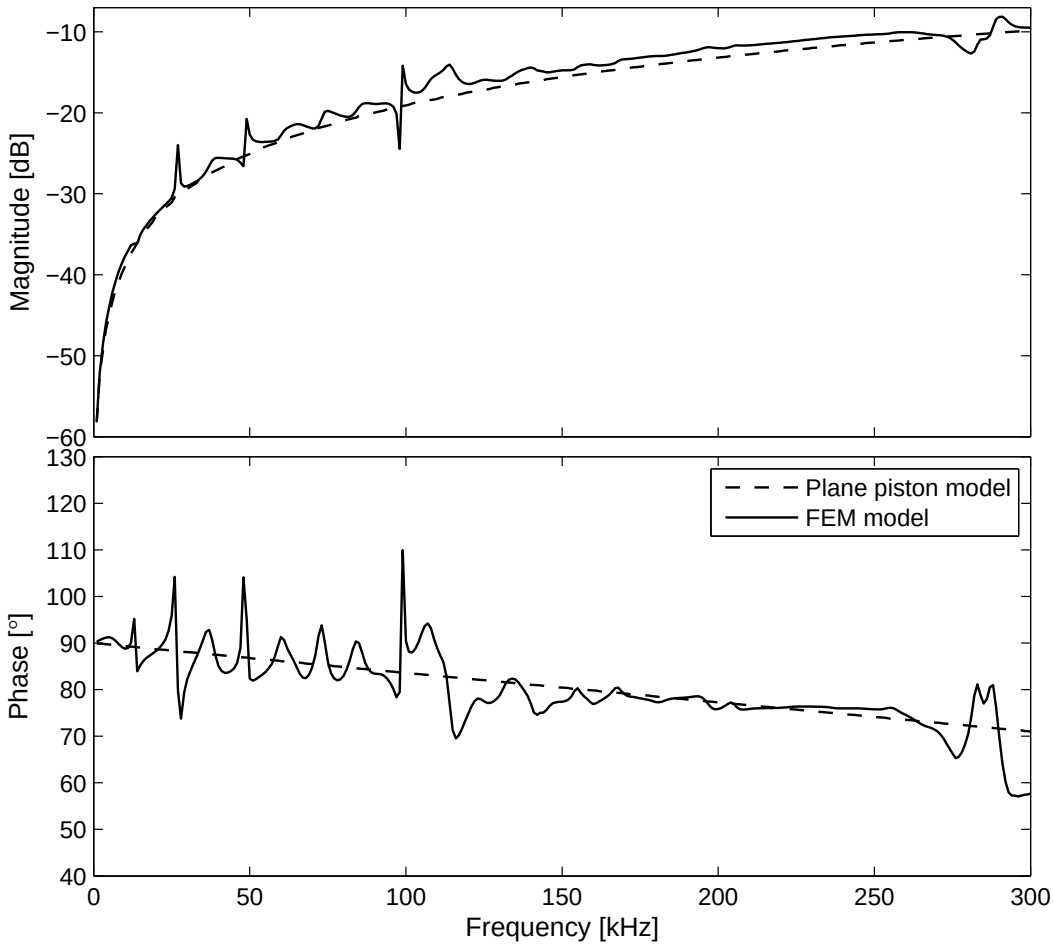

Figure 7.14: Magnitude (a) and phase (b) of the diffraction correction as a function of frequency for a sound velocity of 340 m/s and receiver distance of 15 cm. The plane piston radius is 4.25 mm.

between the FEM and plane piston models is observed in the near field, say for $z < 3$ cm, or $S < 2.6$. This issue is addressed in Sec. 7.7.

In the transition zone between the near field and the far field, the two diffraction correction models are in close agreement, both with respect to magnitude and phase. At the distance of particular interest, $z = 15$ cm, agreement to within 0.1 dB and 0.13° is found for the magnitude and phase of the correction, respectively.

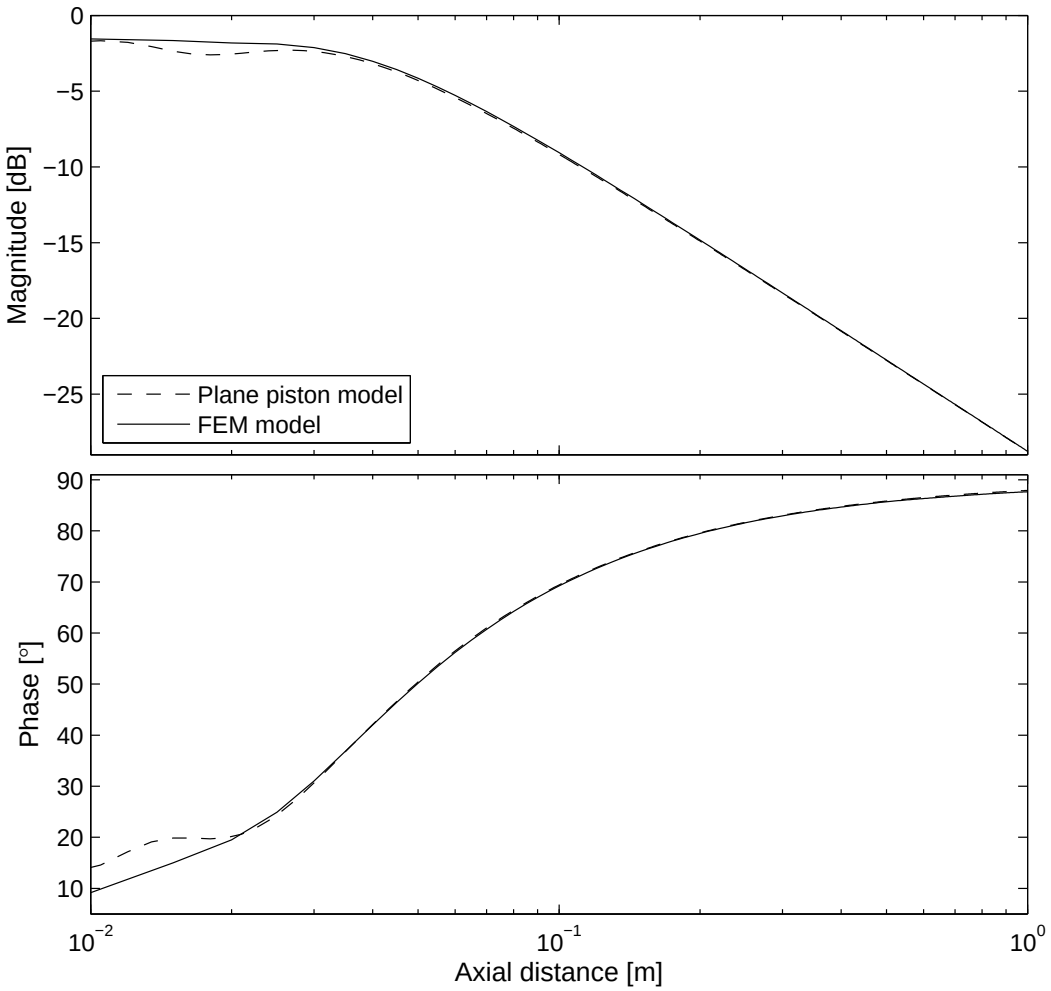

Figure 7.15: Magnitude (a) and phase (b) of the diffraction correction as a function of logarithmic distance. The sound velocity is 340 m/s, the frequency is 218 kHz, and the plane piston radius is 4.25 mm.

At very long ranges, i.e. in the far field, the agreement between the two diffraction correction models is of course close, as they have actually been matched in the far field, at the distance $z_{ff} = 1000$ m.

7.7 Discussion

In spite of difficulties in relation to precise comparisons with measurements, cf. Section 7.1, the qualitative FEM description of the transducer has proved to be useful for evaluating the plane piston diffraction correction model used in [26, 27, 28, 29] for the

transducer analyzed here. This is so especially in the vicinity of the frequency at which the transducer is operated, 218 kHz.

In a frequency band around 218 kHz, say 150 to 270 kHz, a reasonably good agreement has been found between the FEM and plane piston diffraction correction model results, when using the effective source transducer radius, a_{eff}. In this range the deviations are within 1.4 dB and 2.8° for the magnitude and phase of the diffraction correction, respectively, at an axial source-receiver distance of 15 cm (cf. Fig. 7.14). At 218 kHz, the deviations are respectively 0.1 dB and 0.13° at the same distance of 15 cm (cf. Fig. 7.15).

Such relatively good agreement for the diffraction correction is found in spite of the non-piston-like vibration pattern of the transducer at these frequencies, cf. Figs. 7.9a – 7.12a. This agreement is ascribed to a relatively good match between the FEM and plane piston model directivities over the central part of the main lobe, cf. Figs. 7.9b – 7.12b. At a distance of 15 cm, in the transition zone between the near and far fields, the receiver is relatively small compared to the beam. That is, a total beam angle of only 3.4° is sufficient to cover the receiver, which represents a relatively small portion of the main lobes shown in Figs. 7.9b – 7.12b.

With respect to the side lobes, a poorer agreement between the FEM and the plane piston model is found. However, at the distance 15 cm, this is not expected to influence the diffraction correction results significantly for the ka numbers in question here, since in this region, the receiving transducer aperture is essentially covered by the main lobe.

In the near field, the deviations between the FEM and plane piston diffraction correction model results are larger, which may probably be ascribed to larger influence from the non-piston-like vibration pattern of the transducer at close ranges.

A reasonable quantitative agreement between the FEM calculated and the measured main

lobes at the frequencies 163, 180, 198 and 218 kHz (Figs. 7.9b – 7.12b), in addition to a reasonable qualitative agreement for the FEM calculated and the measured voltage source sensitivity in this range (Fig. 7.5), indicate that the FEM approach, using a tentative model for the transducer construction, provides a reasonable description of the transducer in a band around the operating frequency, 218 kHz. It is expected that by improved knowledge on the transducer construction details and the materials and material data involved, a significantly better qua ntitative agreement with the measurements could be achieved.

Thus, the results indicate that,—in spite of the fact that the transducer's vibration pattern at and around the operating frequency 218 kHz is relatively different from that of a uniformly vibrating piston, the plane piston diffraction correction model may be a relevant and useful model at and in a band around this frequency, 218 kHz, for the receiver in the transition zone between the near field and far field.

The present findings thus support the approach used in [26, 27, 28, 29], where the plane piston diffraction correction model has been used at the operating frequency of the transducer, 218 kHz, at a source-receiver distance of 15 cm.

Outside the frequency range 150 – 270 kHz, the situation is somewhat different. Basically, the trends of the diffraction correction models are in qualitative, but not quantitative agreement, cf. Fig. 7.14.

Several dips are apparent in the FEM diffraction correction magnitude results at particular frequencies, especially in the 0 – 150 kHz range. The phase of the FEM diffraction correction "oscillates" around the corresponding plane piston model results, with significant deviations at some frequencies. Inspection of the source sensitivity (Fig. 7.5) reveals distinct dips e.g. at the frequencies 49, 74 and 99 kHz, corresponding to dips in the directivity in the axial direction (not shown here for 49 kHz and 74 kHz). Accordingly,

the FEM diffraction correction model exhibits strong deviations from the plane piston diffraction correction model at these frequencies.

Strong peaks appear in the FEM simulated source sensitivity e.g. at the frequencies 69, 95 and 110 kHz. However, these do not affect the diffraction correction equally much (Fig. 7.14) as the dips mentioned above (at e.g. 49, 74 and 99 kHz).

At 300 kHz, a considerable deviation is found for the phase of the diffraction correction, but not for the magnitude, cf. Fig. 7.14.

Understanding the causes of the deviations between the FEM and plane piston diffraction correction models outside the 150 – 270 kHz band is of course an important issue in itself, for the general understanding of diffraction correction. It is expected that at least large parts of the deviations can be explained by the different directivities predicted by the two models, for the various transducer modes in question, cf. e.g. Fig. 7.8. For example, in Fig. 7.14 significant deviation between the two diffraction correction models is observed at 99 kHz, both for the magnitude and phase. Figure 7.8b shows a significant axial dip in the FEM calculated directivity at the same frequency, and that the calculated source sensitivity dip observed in Fig. 7.5 at this frequency is actually caused by the axial dip in the directivity. For a receiver in the far field (very long ranges), the receiver will appear as a point on the axis, in the bottom of the dip, and the sound pressure will be practically constant over the receiver. At such ranges there is perfect agreement between the two diffraction correction models, as they are actually matched in the far field, at $z_{ff} = 1000$ m. However, as the receiver is moved to shorter ranges, into the transition zone, the receiver will gradually cover more of the dip, and the sound pressure will vary more rapidly across the receiver aperture. That is, one begins to see near field effects even at relatively large distances, and such effects seem to cause the deviation between the two diffraction correction models. However, the precise reasons for the deviations in the various frequency ranges have not been sufficiently revealed, and further work is

needed to explain these effects more thoroughly, and relate the m to measured effects for a real transducer.

It should be noted that at very long ranges, such as approaching $z = 1000$ m, the "anomalies" observed in the FEM diffraction correction (Fig. 7.14) disappear; this follows from the approach described in Sec. 7.2.2, that the two diffraction correction models are matched to coincide in the far field, at $z_{ff} = 1000$ m.

There is an unresolved question related to this analysis, namely that a dip such as e.g. at 99 kHz in the FEM calculations (the axial dip in the directivity, causing the source sensitivity dip) has not been found in the measurement results, cf. Figs. 7.5 and 7.8b. There is the possibility that such a dip actually may have been smeared out by the microphone measurements, due to the finite aperture of the 1/8" microphone. Also effects of the transducer holder, which have been neglected in the simulations, may possibly have contributed to smear out such a dip. This question is here left to future investigations.

As pointed out in Sec. 7.1, it is also important to be aware that although the FEM diffraction correction model used here [24, 30, 31] is considered to represent a significant improvement relative to the more traditional descriptions of diffraction correction, with respect to the description and effects of the transmitting transducer, it still represents a simplification, building on Khimunin's [13, 14] definition of the diffraction correction at the receiving side, cf. Sec. 7.1.

7.8 Conclusions

Diffraction correction has been investigated for a commercial transducer being used initially in [26, 27, 28, 29] as part of development of a sound velocity cell for gas. In this work, transducer diffraction effects and accurate correction for such effects appear to be among the most critical factors in order to realize a high precision measurement cell.

Through comparison with electrical and acoustical measurements, the FEM approach—although suffering from unknown constructional details of the transducer, and thus representing a tentative construction model only—is found to provide a reasonable qualitative representation of the transducer. That is, the FEM diffraction correction model proposed in [24, 30, 31] is considered to provide a more realistic description of the transducer used in [26, 27, 28, 29] than the plane piston diffraction correction model.

Measurements and FEM calculations show that the transducer under investigation does not in general vibrate and radiate as a plane piston. However, at the operational frequency of the transducer, 218 kHz, and at a distance of 15 cm, a relatively good agreement has been achieved between the piston model directivity and the FEM directivity at the central part of the main lobe by using an effective radius for the piston model, in spite of the non-piston-like vibration pattern of the transducer at this frequency. Also, the plane piston diffraction correction model agrees quite well with the FEM diffraction correction model at this frequency by using the effective piston radius. These results indicate that,—in spite of the general poor ability of the plane piston model to describe the transducer, the plane piston diffraction correction model used in the sound velocity measurements described in [26, 27, 28, 29] may still provide a reasonably accurate description for the transducer in question, at the operational frequency and distance used in the sound velocity measurements, when the effective piston radius approach is used.

Outside the operational frequency band of the transducer, there are several relatively large deviations between the FEM and plane piston diffraction correction models. For transducer vibration modes possessing more complicated vibration patterns and directivities, better and more controlled investigations are feasible and necessary to precisely explain the deviations between the two diffraction correction models, and relate them to measured effects for real transducers.

Acknowledgment

The present work is done as a part of a PhD fellowship for the first author, under the 4-year strategic institute programme "Ultrasonic technology for improved exploitation of petroleum resources" (2003-2006), supported by The Research Council of Norway (NFR), Statoil ASA and Gassco AS, and carried out in a cooperation between CMR and the University of Bergen (UoB), Dept. of Physics and Technology. The authors wish to thank assoc. prof. Magne Vestrheim, UoB, for valuable comments and contributions to the work, and Remi A. Kippersund and Kjetil Daae Lohne, both CMR, for valuable advice and assistance in connection with operation of the FEMP model, and experimental measurements of transducer properties in air.

Bibliography

[1] A. O. Williams Jr., "The piston source at high frequency," *J. Acoust. Soc. Am.*, vol. 23, pp. 1–6, 1951.

[2] H. Seki, A. Granato, and R. Truell, "Diffraction effects in the ultrasonic field of a piston source and their importance in the accurate measurement of attenuation," *J. Acoust. Soc. Am.*, vol. 28, pp. 230–238, 1956.

[3] R. Bass, "Diffraction effects in the ultrasonic field of a piston source," *J. Acoust. Soc. Am.*, vol. 30, pp. 602–605, 1958.

[4] E. P. Papadakis, "Correction for diffraction losses in the ultrasonic field of a piston source," *J. Acoust. Soc. Am.*, vol. 31, pp. 150–152, 1959.

[5] H. J. McSkimin, "Empirical study of the effect of diffraction on velocity of propagation of high-frequency ultrasonic waves," *J. Acoust. Soc. Am.*, vol. 32, pp. 1401–1404, 1960.

[6] A. E. Lord Jr., "Changes in velocity of an elastic pulse owing to geometrical diffraction," *J. Acoust. Soc. Am.*, vol. 40, pp. 163–169, 1966.

[7] E. P. Papadakis, "Ultrasonic phase velocity by the pulse-eho-overlap method incorporating diffraction phase corrections," *J. Acoust. Soc. Am.*, vol. 42, pp. 1045–1051, 1967.

[8] R. C. Williamson, "Echo phase-comparison technique and measurement of sound velocity in water," *J. Acoust. Soc. Am.*, vol. 45, pp. 1251–1257, 1969.

[9] M. B. Gitis and A. S. Khimunin, "Diffraction effects in ultrasonic measurements (review)," *Sov. Phys. Acoust.*, vol. 14, pp. 413–431, 1969.

[10] A. O. Williams Jr., "Integrated signal on circular piston receiver centered in a piston beam," *J. Acoust. Soc. Am.*, vol. 48, pp. 285–289, 1970.

[11] E. P. Papadakis, "Effects of input profile upon diffraction loss and phase change in a pulse-echo system," *J. Acoust. Soc. Am.*, vol. 49, pp. 166–168, 1971.

[12] ——, "Absolute accuracy of the pulse-echo overlap method and the pulse-superposition method for ultrasonic velocity," *J. Acoust. Soc. Am.*, vol. 52, pp. 843–846, 1972.

[13] A. S. Khimunin, "Numerical calculation of the diffraction corrections for the precise measurement of ultrasound absorption," *Acustica*, vol. 27, pp. 173–181, 1972.

[14] ——, "Numerical calculation of the diffraction corrections for the precise measurement of ultrasound phase velocity," *Acustica*, vol. 32, pp. 192–200, 1975.

[15] M. Sedlacek and A. Asenbaum, "Simultaneous measurement of sound velocity and sound attenuation in liquids by a correlation method," *J. Acoust. Soc. Am.*, vol. 62, pp. 1420–1423, 1977.

[16] R. A. Bacon and R. C. Chivers, "Radiation coupling of a disc to a disc: a numerical approach," *Acoustics letters*, vol. 5, pp. 22–29, 1981.

[17] K. Beissner, "Exact integral expression for the diffraction loss of a circular piston source," *Acoustica*, vol. 49, pp. 212–217, 1981.

[18] T. Imamura, "Deformation of ultrasonic pulse with diffraction," *Ultrasonics*, vol. 37, pp. 71–78, 1999.

[19] L. E. Kinsler, A. R. Frey, A. B. Coppens, and J. V. Sanders, *Fundamentals of acoustics*, 4th ed. New York, USA: John Wiley and sons, Inc., 2000.

[20] P. Lunde, K.-E. Frøysa, and M. Vestrheim, Eds., *GERG project on ultrasonic gas flow meters, Phase II.* GERG Technical monograph GERG TM11, Groupe Européen de Recherches Gazières, VDI Verlag, Düsseldorf, 2000, ISBN 3-18-385408-2.

[21] P. Lunde, K.-E. Frøysa, and M. Vestrheim, "Challenges for improved accuracy and traceability in ultrasonic fiscal flow metering," in *Proc. of the 18th North Sea Flow Measurement Workshop*, Gleneagles, Scotland, Oct. 2000.

[22] P. Lunde and K.-E. Frøysa, *Handbook of uncertainty calculations – Ultrasonic fiscal gas metering stations*, Norwegian Petroleum Directorate, Norwegian Society for Oil and Gas Measurement (NFOGM), 2001, ISBN 82-566-1009-3. Free download from www.nfogm.no.

[23] P. Lunde, K.-E. Frøysa, and M. Vestrheim, "Transient diffraction effects in ultrasonic flow meters for gas and liquid," in *Proc.* 26th *Scandinavian Symposium on Physical Acoustics*, Ustaoset, Norway, Jan. 2003, Scientific/Technical Report No. 420304 (CD Issue only).

[24] P. Lunde, K.-E. Frøysa, R. A. Kippersund, and M. Vestrheim, "Transient diffraction effects in ultrasonic meters for volumetric, mass and energy flow measurement of natural gas," in *Proc. 21st Intern. North Sea Flow Measurement Workshop*, Tønsberg, Norway, Oct. 2003, pp. 33–59.

[25] P. Lunde and M. Vestrheim, "Precision sound velocity cell for natural gas at high pressures. Phase 1—feasibility study." CMR, Bergen, Norway, Tech. Rep. CMR-98-F10039 (Confidential), Dec. 1998.

[26] P. Norli, P. Lunde, and M. Vestrheim, "Methods for precision sound velocity measurements in pressure cells for gas characterization," in *Proc.* 27th *Scandinavian Symposium on Physical Acoustics*, Ustaoset, Norway, Jan. 2004, CD issue only, ISBN 82-8123-000-2.

[27] P. Norli, "Comparison of three methods for precision sound velocity measurement of gases," in *Proc. 28th Scandinavian Symposium on Physical Acoustics*, Ustaoset, Norway, Jan. 2005, CD Issue only ISBN: 82-8123-000-2.

[28] P. Norli, P. Lunde, and M. Vestrheim, "Investigation of precision sound velocity measurement methods as reference for ultrasonic gas flow meters," in *Proc. 2005 IEEE Ultrasonics Symposium*, Rotterdam, The Netherlands, Sept. 2005, pp. 1443–1447.

[29] P. Norli and P. Lunde, "A three-way pulse method for a precision sound velocity measurement cell," in *Proc. 2006 IEEE Ultrasonics Symposium*, Vancouver, Canada, Oct. 2006, pp. 884 – 889.

[30] P. Lunde, R. A. Kippersund, M. Vestrheim, and K.-E. Frøysa, "Transient diffraction effects in piezoelectric ultrasonic transducers using finite element modelling," in *Proc. 27th Scandinavian Symposium on Physical Acoustics*, Ustaoset, Norway, Jan. 2004, CD issue only, ISBN 82-8123-000-2.

[31] ——, "Finite element modelling of diffraction correction for non-uniformly vibrating piezoelectric ultrasonic transducers," paper in preparation.

[32] J. Kocbach, P. Lunde, and M. Vestrheim, "FE simulations of piezoceramic disks with a front layer of varying thickness," in *Proc. IEEE International Ultrasonics Symposium*, Caesars Tahoe, NV, USA, Oct. 1999, pp. 1113–1117.

[33] J. Kocbach, "Finite element modeling of ultrasonic piezoelectric transducers. Influence of geometry and material parameters on vibration, response functions and radiated field," Dr. Scient thesis. University of Bergen, Dept. of Physics, Bergen, Norway, 2000.

[34] J. Kocbach, P. Lunde, and M. Vestrheim, "Resonance frequency spectra with convergence tests of piezoceramic disks using the finite element method," *Acustica*, vol. 87, pp. 271–285, 2001.

[35] (2006, Jan.) The Massa E-188/220 transducers. Massa Corp. [Online]. Available: http://www.massa.com/datasheets/e188.html

[36] S. Vervik, "Transitt-tidsbestemmelse for ultralyd strømningsmetre. Nullstrømningsforhold," Cand. Scient thesis. University of Bergen, Dept. of Physics, Bergen, Norway, 1995, (In norwegian).

[37] "Five modern piezoelectric ceramics, bulletin 66011f," 1976, Vernitron Ltd., England; now Morgan Matroc Ltd.

[38] R. A. Kippersund, P. Lunde, and M. Vestrheim, "Finite element modelling of piezoelectric ultrasonic transducer properties in natural gas," in *Proc.* 27^{th} *Scandinavian Symposium on Physical Acoustics*, Ustaoset, Norway, Jan. 2004, CD issue only, ISBN: 82-8123-000-2.

[39] 2006, personal communication with R. A. Kippersund, CMR.

[40] "American national standard method for the calculation of the absorption of sound by the atmosphere," Acoustical Society of America, New York, U.S.A., 1978, American National Standard, ANSI SI.26-1978.

Chapter 8

Paper C

A two-way pulse echo method for a precision sound velocity measurement cell

Author:

Petter Norli

Reformatted version of the paper submitted to:

Applied acoustics. Accepted for publication, given some minor modifications, as of June 27, 2007.

Abstract

A precision sound velocity measurement cell for natural gas under pressure from 0 – 250 bar, working in the frequency range of 100 – 200 kHz, with a target experimental uncertainty of 100 – 200 ppm is under development. As part of this work, three transient methods are investigated [Proc. 2005 IEEE Ultrasonics Symposium, pp. 1443-1447, 2005], and they are seen to have several common sources of experimental uncertainty. The present paper proposes a two-way pulse echo candidate method for the sound velocity cell, reporting sound velocity measurement results obtained in a prototype cell, using air at about 1 atm and 27 °C as test gas.

The results are compared with predictions from a sound velocity model for air (including dispersion) [J. Acoust. Soc. Amer. 93 (5), pp. 2510-2516, 1993], and they indicate that the method may have potential to perform in line with the target specifications of the sound velocity cell. Use of a temperature regulated bath is expected to significantly reduce the temperature induced convection flows that presently limit the experimental accuracy, and that the measurement uncertainty may be reduced accordingly.

8.1 Introduction

Multipath ultrasonic transit time flow meters (USMs) are today commonly used in for example industrial applications like volumetric fiscal flow metering of natural gas [1, 2]. In such metering, gas is typically sold on basis of mass or energy, thus in addition to the volumetric flow rate, the density or calorific value is needed. These quantities may be measured by means of densitometers and gas chromatographs (GCs) [1].

In [1, 2], an alternative method for calculating density and calorific value from the sound velocity, temperature and pressure is proposed and used. Thus, as the USM measures the sound velocity in addition to the volumetric flow rate, it has a potential of being a mass or energy flow rate meter, given that the accuracy of the sound velocity measurement is within certain specifications [3].

To provide a reference value for the sound velocity measured by the USM, a precision sound velocity cell would be desirable, working primarily with natural gas under the same conditions as the USM [4]. These have been tentatively pointed out [4] for pressure, temperature and frequency as: 0 – 250 barg, 0 – 60 °C and 100 – 200 kHz, respectively. The uncertainty of the sound velocity measurements should be within $\pm(0.05 - 0.1)$ m/s, or $\pm(100 - 200)$ ppm [4], and the cell should preferably not involve moving parts [4].

A feasibility study on realizing such a cell was executed in 1998 [4], featuring a review of existing measurement methods, which were evaluated with respect to meet the given cell specifications. No method was identified that could fulfill every cell specification. Nor was this the case in a follow-up literature survey [5].

Outstanding measurement accuracy has been demonstrated using spherical resonator methods [6], however, operating in the audio frequency range. They may thus not account for dispersion effects which may be relevant in the 100 – 200 kHz range. Frequency scaling was considered [4], however, it seemed not feasible to maintain sufficient experimental

accuracy. Transient methods have been used at elevated pressures up to 20000 bar [7], and operated typically in the MHz range, generally performing with significantly poorer accuracy than required, though.

Three transient methods have been investigated, aiming to realize the sound velocity cell [5, 8, 9, 10, 11], of which two are considered as promising candidates: 1) a *three-way pulse method*, proposed in [4] and realized and tested experimentally in [10], and 2) the *two-way pulse echo method* (2PEM) currently described and tested experimentally.

The 2PEM is based on a transient method described in a patent article [12], intended to be used for sound velocity measurements on gas, liquid or solid. A similar method, intended for measuring e.g. acoustic impedance and density has been identified in [13]. The method in [12], which—to the author's knowledge—merely has been described theoretically, has here been modified by among others including correction terms such as diffraction correction. Moreover, the method has here been realized experimentally in a prototype sound velocity cell, reporting measurement results for atmospheric air at about 27 °C and a relative humidity of about 30%.

8.2 Theory

8.2.1 The two-way pulse echo method

A transient pulse echo method for sound velocity measurements was suggested in [12], in which two acoustic transducers both act as transmitter and receiver, and are separated from the medium by buffer rods. The present paper describes a modified version of the method in [12], in the sense that the buffer rods have been removed, besides that correction terms, such as diffraction and thermal and viscous boundary layer correction have been introduced. The present measurement principle, shown in Fig. 8.1, is explained in the following.

Measurement principle

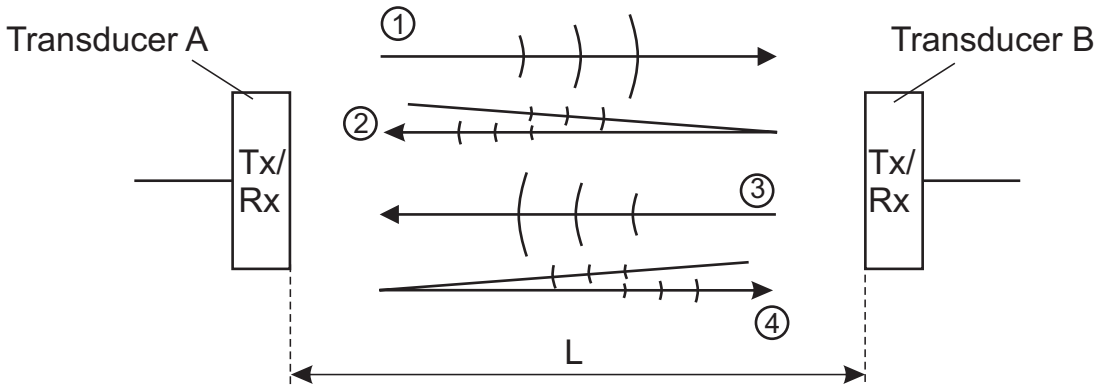

Figure 8.1: The measurement principle of the two-way pulse echo method.

Now pulse ① is transmitted from acoustic transducer A (TrA) across the axial transducer separation L, partly propagating into the opposite transducer B (TrB), and the associated pulse transit time, t_1, is measured. Pulse ① is partly reflected at TrB, giving rise to echo ② which is received at TrA, so that the associated transit time, t_2, can be measured.

The process is repeated from the opposite side at the subsequent trigging event, using TrB as transmitter, so as to obtain transit times t_3 and t_4 from pulse ③ and echo ④, respectively.

Measurement model

To facilitate the measurement sequence described above, the measurement system shown in Fig. 8.4 was used. It is here somewhat simplified, based on the approach in [12], to model and account for the system time delays, cf. Fig. 8.2. The measurement system is assumed to be stationary throughout the measurement.

Now, from Figs. 8.1 and 8.2, the measured transit times, t_1 to t_4, can be written as

$$\begin{aligned} t_1 = t_{gen}^{TrA} + t_{SB} + t_{CA}^{TrA} + t_{TrA}^{Tx} + t_1^{gas} + t_1^{corr} \\ + t_{TrB}^{Rx} + t_{CB}^{rec} + t_{SC} + t_{rec}^{TrB}, \end{aligned} \tag{8.1}$$

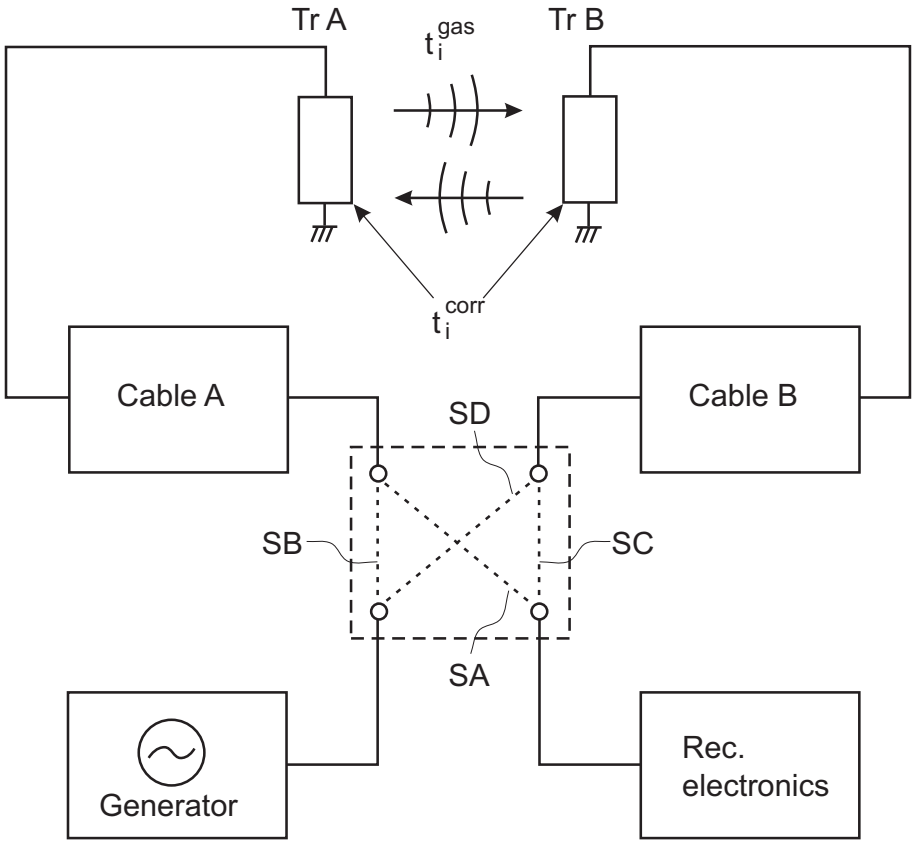

Figure 8.2: Functional diagram of the measurement system.

$$t_2 = t_{gen}^{TrA} + t_{SB} + t_{CA}^{TrA} + t_{TrA}^{Tx} + t_2^{gas} + t_2^{corr} + t_{TrA}^{Rx} + t_{CA}^{rec} + t_{SA} + t_{rec}^{TrA}, \tag{8.2}$$

$$t_3 = t_{gen}^{TrB} + t_{SD} + t_{CB}^{TrB} + t_{TrB}^{Tx} + t_3^{gas} + t_3^{corr} + t_{TrA}^{Rx} + t_{CA}^{rec} + t_{SA} + t_{rec}^{TrA}, \tag{8.3}$$

$$t_4 = t_{gen}^{TrB} + t_{SD} + t_{CB}^{TrB} + t_{TrB}^{Tx} + t_4^{gas} + t_4^{corr} + t_{TrB}^{Rx} + t_{CB}^{rec} + t_{SC} + t_{rec}^{TrB}, \tag{8.4}$$

in which the notation is defined in Table 8.1. Now, by taking $t_2 - t_1 + t_4 - t_3$, we obtain

$$t_2 - t_1 + t_4 - t_3 = t_2^{gas} - t_1^{gas} + t_4^{gas} - t_3^{gas} + t_2^{corr} - t_1^{corr} + t_4^{corr} - t_3^{corr}, \tag{8.5}$$

and from Fig. 8.1 we note that in a stationary fluid, $t_2^{gas} = t_4^{gas} \equiv 2L/c$, and $t_1^{gas} = t_3^{gas} \equiv L/c$. By inserting these relations, we obtain the sound velocity c as

$$c = \frac{2L}{\Delta t - t^{corr}}, \tag{8.6}$$

where

$$\Delta t \equiv t_2 - t_1 + t_4 - t_3, \tag{8.7}$$

and

$$t^{corr} \equiv t_2^{corr} - t_1^{corr} + t_4^{corr} - t_3^{corr}. \tag{8.8}$$

To account for thermal expansion in the *measurement unit* (cf. Sec. 8.3.1), $L = K_T L_0$ is introduced, where K_T is the thermal expansion coefficient, and L_0 is the reference transducer separation, measured at the reference temperature T_0. The quantity K_T was modelled by a linear relationship, $K_T = 1 + \alpha(\overline{T} - T_0)$, where $\alpha = 11.1 \cdot 10^{-6}$ K^{-1} is the thermal expansion coefficient for the material of the measurement unit, *steel AISI 316* [14], and $\overline{T}$ is the measurement temperature in Kelvin, cf. Sec. 8.3.1.

Pressure expansion/contraction [4] of the measurement unit is not considered to be relevant here, as the measurements were carried out in atmospheric air. Hence we have

$$c = \frac{2K_T L_0}{\Delta t - t^{corr}}. \tag{8.9}$$

The measurement of L_0 and Δt are described in Secs. 8.3.2 and 8.3.3, respectively, and the modelling of the correction term t^{corr} is described in Sec. 8.2.2. A major advantage with the current method is the canceling of the delay times of the transmitting and receiving electronics and transducers, which also should hold for different transducers.

8.2.2 Correction terms

The identified effects to be corrected in the 2PEM are: phase shift due to transducer diffraction, phase shift due to thermal and viscous boundary layers upon reflection from

Table 8.1: Explanation of the notation in Eqs. (8.1)–(8.4). Superscript $j = \{TrA, TrB\}$ denotes that transducer A and B are terminations, respectively.

t^j_{gen}	Voltage – voltage generator travel time
t^{TrA}_{CA}, t^{rec}_{CA}	Voltage – voltage travel time of cable A with TrA and the receiving electronics as terminations, respectively
t^{TrB}_{CB}, t^{rec}_{CB}	Voltage – voltage travel time of cable B with TrB and the receiving electronics as terminations, respectively
t_{SA}, t_{SB}, t_{SC}, t_{SD}	Voltage – voltage travel times of switches A, B, C and D, respectively
t^{Tx}_{TrA}, t^{Tx}_{TrB}	Voltage – plane wave pressure travel time for TrA and TrB when transmitting, respectively
t^{gas}_i	Plane wave pressure travel time in the gas for respective signal $i = 1, \ldots, 4$, in absence of the receiving transducer
t^{corr}_i	Correction terms for respective signal $i = 1, \ldots, 4$. Cf. Sec. 8.2.2
t^{Rx}_{TrA}, t^{Rx}_{TrB}	Plane wave pressure – voltage travel time for TrA and TrB when receiving, respectively
t^j_{rec}	Voltage – voltage travel time in the receiving electronics

the transducer front, and phase shift due to interference with echoes from the transducer interior upon reflection from the transducer front. However, the findings in [11] suggest that effects of interference with echoes from the transducer interior be included in the experimental uncertainty budget rather than as a correction term, cf. Sec. 8.4.2. This was thus done.

Let the terms on the righthand side of Eq. (8.8) be given as

$$t^{corr}_i \equiv t^{dif}_i + t^{tv}_i, \quad i = 1, \ldots, 4, \tag{8.10}$$

where t^{dif}_i and t^{tv}_i are associated with diffraction correction and thermal and viscous

boundary layers, respectively. However, as thermal and viscous boundary layer effects are associated with reflection at the transducer front, we put $t_1^{tv} = t_3^{tv} = 0$. Furthermore, it has been found [15] that the *Massa E-188/220* air transducers used here [16], henceforth abbreviated *mas*, produce quite similar beam patterns. Hence it is assumed that $t_1^{dif} = t_3^{dif}$ and $t_2^{dif} = t_4^{dif}$.

The plane piston diffraction correction model

To account for transducer diffraction effects, the model which may be referred to as *the plane piston diffraction correction model* [17, 18, 19] has been used. It represents and accounts for diffraction effects caused by a plane circular piston of radius a, seated in an infinite rigid planar baffle and vibrating with uniform velocity. The source transmits sound waves to a coaxial circular receiver of equal diameter (in absence of the receiver), having uniform sensitivity across the aperture.

To determine how adequately the plane piston model can describe transducer diffraction effects caused by the mas transducer, an investigation was carried out by use of a finite element model (FEM) for diffraction correction [15, 20, 21]. It was indicated that the plane piston diffraction correction model may be used with little error at the operating frequency, $f_0 = 218kHz$, in atmospheric air at room temperature, and with a receiver distance of less than 1 m.

A diffraction correction function H^{dif} is given by [17, 18, 19]

$$H^{dif} = 1 - \frac{4}{\pi} \int_0^{\pi/2} e^{\imath kz\left[1-\sqrt{1+\left(\frac{2a}{z}\cos\theta\right)^2}\right]} \sin^2\theta \, \mathrm{d}\theta, \tag{8.11}$$

where θ is an integration variable, $k = 2\pi/\lambda$ is the loss-free wave number, $\lambda = c/f_0$ is the acoustic wavelength, z is the source-receiver distance, and $\omega_0 = 2\pi f_0$ is the angular burst

center frequency. Now, the diffraction time correction is given by

$$t^{dif} = \angle H^{dif}/\omega_0. \tag{8.12}$$

Due to assumptions made in the next section, t_1^{dif} will in fact be canceled in the present work. Yet t_2^{dif} is to be evaluated.

Diffraction correction for pulse echo operation

The plane piston diffraction correction model is primarily intended for direct wave transmission, such as for pulse ① (and ③), cf. Fig. 8.1. To evaluate diffraction correction for an echo like ② (and ④), consider the following approach.

If the reflecting front face of the transducer is small compared to the incoming beam, so that the incident sound wave may be assumed to have uniform phase and amplitude across the reflector, it may be reasonable to treat the reflector as a new plane piston source, having uniform vibration across the front face [22, p. 91]. The mas transducer has a total beam angle $2\theta_{-3dB} = 10°$, insonifying a circle of diameter approximately 26 mm at $z = L = 151$ mm, presumably exceeding the transducer front face diameter of 12 mm sufficiently to comply with the given premise.

It is consequently possible to decompose the diffraction correction for echo ②, t_2^{dif}, in two parts; one due to reflection at the opposite transducer TrB, and another due to reception at TrA, and apply the plane piston diffraction correction for each of them. We hence define

$$t_2^{dif} \equiv t^{dif,p} + t^{dif,e}, \tag{8.13}$$

where superscripts p and e denote diffraction correction due to pulse and echo propagation, respectively.

Here, $t^{dif,p}$ is calculated using Eqs. (8.11) and (8.12), replacing a with the effective radi-

ating radius of the transducer [5], $a_{eff} = 4.25$ mm. It is thus assumed that the radius of the reflecting transducer front face, a_{fr}, is a_{eff} instead of $a_{fr} = 6$ mm, which actually leads to $t^{dif,p} = t_1^{dif}$. The term $t^{dif,e}$ is also calculated by use of Eqs. (8.11) and (8.12), now input with the radius of the reflecting transducer front face, a_{fr}. Hence, the receiver is also assumed to have the radius a_{fr} rather than e.g. an effective receiving radius.

Thermal and viscous boundary layers

Due to the incidence of ② and ④ upon reflection at the transducer front, thermal and viscous boundary layers are generated in a thin fluid layer adjacent to the transducer front [23, 24], which to some extent shifts ② and ④ in phase (and magnitude).

In our case, we shall assume that the sound wave is plane and falls perpendicularly into the transducer front. This enables that a complex reflection coefficient, given as the ratio of reflected and incident pressure, may be calculated to account for the phase shift caused by the boundary layers. The theory given in [23, p. 529] was utilized for atmospheric *dry* air at 27 °C, which is roughly the measurement temperature. A phase correction of about 0.009 rad was obtained for $f_0 = 218$ kHz, corresponding to $t_2^{tv} = t_4^{tv} = 6.5$ ns, i.e. about 8 ppm relative to Δt. It is thus assumed that $t_2^{tv} = t_4^{tv}$.

Assembly of the correction terms

By combining Eqs. (8.8) and (8.10) and using the assumptions above, we have

$$t^{corr} = 2(t_2^{dif} - t_1^{dif} + t_2^{tv}). \tag{8.14}$$

Insertion of t_2^{dif} yields

$$t^{corr} = 2(t^{dif,p} + t^{dif,e} - t_1^{dif} + t_2^{tv}). \tag{8.15}$$

But recognizing that $t^{dif,p}$ is calculated using the plane piston diffraction correction model above input with a_{eff} as radius, just like t_1^{dif} (and all the other parameters are equal),

Eq. (8.15) turns into

$$t^{corr} = 2(t^{dif,e} + t_2^{tv}). \tag{8.16}$$

The value of t^{corr} used in the present work is about -1606 ns, i.e. -1855 ppm relative to Δt, in which t_2^{tv} relative to $t^{dif,e}$ is only about 0.4%.

8.2.3 A sound velocity model for humid air

A sound velocity model for standard air [25] around atmospheric pressure was used for comparison, for which the input parameters are temperature, pressure, relative humidity and CO_2 concentration. It was chosen due to its realistic foundation, accounting for non-ideal gas effects by a truncated virial equation of state, but also because of its extensive empirical support [26, Table II].

In this work, the CO_2 concentration of outdoor air is used, 382 ppm [27], a value which may be somewhat low for indoor air. To indicate the significance of this simplification, an increase in the CO_2 concentration of, say 200 ppm, would decrease the predicted c with about 50 ppm.

The following relation was utilized to account for dispersion in the air medium [25, 28]

$$\frac{1}{c_0} - \frac{1}{c} = \frac{\alpha_{vN}}{2\pi f_{rN}} + \frac{\alpha_{vO}}{2\pi f_{rO}}, \tag{8.17}$$

where c is the sound phase velocity at 218 kHz, c_0 is the sound velocity in the zero frequency limit, α_{vN} and α_{vO} are the plane-wave sound attenuation coefficients due to vibrational relaxation of nitrogen and oxygen, respectively, and f_{rN} and f_{rO} are the relaxation frequencies for nitrogen and oxygen, respectively.

The dispersion, $c - c_0$, was in the current experiments typically calculated to about 0.15 m/s, or ~ 435 ppm relative to c. Due to lacking knowledge about the uncertainty of the dispersion model at 218 kHz, it was not accounted for here. The overall model uncertainty

is thus taken to be that exclusive dispersion correction, ±300 ppm (confidence level not specified) [25].

8.3 Experimental

8.3.1 Experimental setup

The sound velocity cell

As a step towards the precision sound velocity measurement cell, a prototype apparatus for low pressure (< 13 bara) has been devised, cf. Fig. 8.3. The cell has also been used with a different measurement method described elsewhere [10], using a slightly different measurement system. Note that *Measurement unit* denotes the core of the measurement cell, comprising among others parts **1**, **2**, **3** and **11**, enabling a well defined transducer alignment.

Initially, using different materials for different parts of the cell was considered in order to reduce thermal expansion and acoustical cross-talk. However, this would probably degrade the angular alignment of the transducers and increase the uncertainty in the thermal expansion coefficient K_T, and was thus not done. The prototype measurement cell was fabricated in *steel AISI 316*, and the cell design has evolved from considerations described in Sec. 8.3.4 and [4]. The dimensional rationale is given in [11], and the dimensions are as follows (cf. Fig. 8.3): $L_0 = 151$ mm, $L_{pen} = 49.7$ mm and r_{cw} is, as the measurement unit is placed off the axis, in the range 101.5 to 109.5 mm. The reason for placing the measurement unit non-concentric with the cell walls was to minimize possible coherent echoes from the cell walls.

The ultrasonic transducers **1** and holders **2** are described in Sec. 8.3.1. The spacer rods **3** are designed as slim as possible (with diameter 8 mm) and grooved, with depth 0.5 mm and pitch 1 mm, to reduce possible reflections.

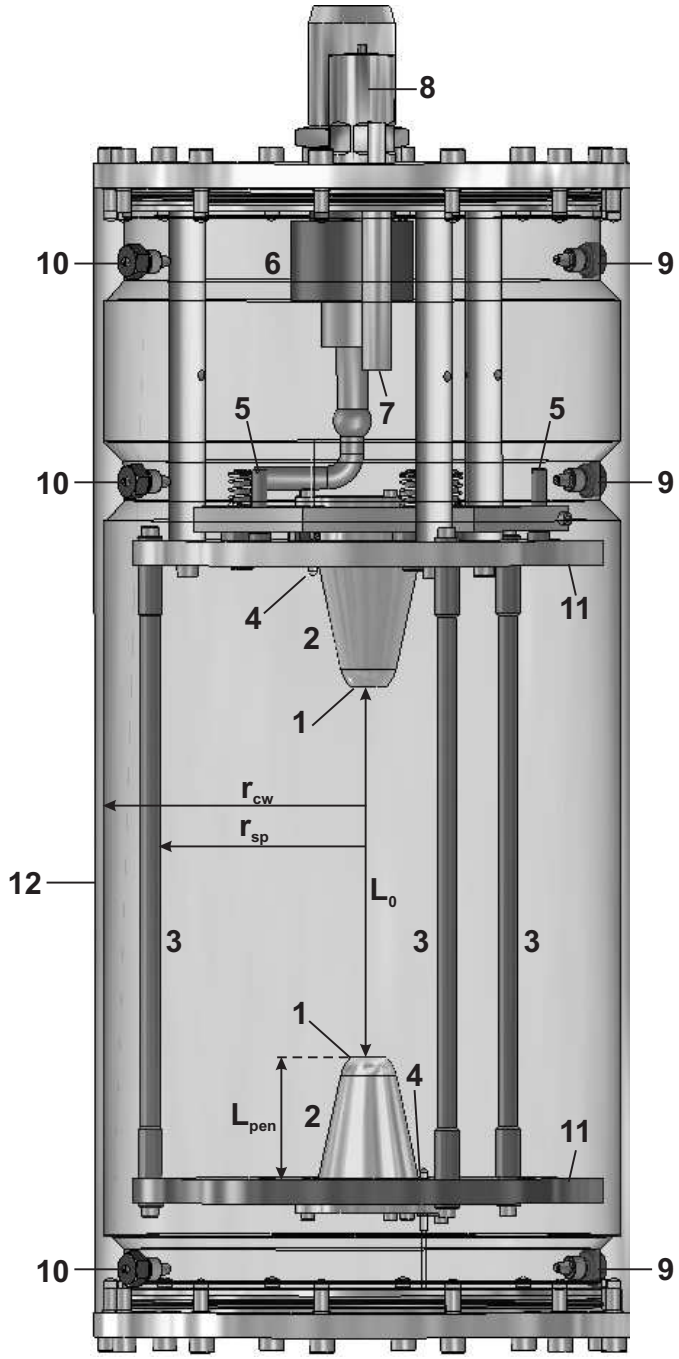

Figure 8.3: Cut-through design sketch of the prototype sound velocity measurement cell. The parts are labeled as follows. **1** ultrasonic transducers; **2** transducer holders; **3** transducer spacer rods; **4** *Pt-100* thermocouples; **5** parallelity adjustment screws; **6** cable feedthrough connector; **7** humidity sensor; **8** safety valve; **9** gas inlet ports; **10** gas outlet ports; **11** end faces, and **12** cell wall. Note that the wall was covered with a rugged, soft clothing (not shown) to spread and absorb possible wall echoes.

The Pt-100 thermocouples **4**, denoted by A and B, are mounted diagonally and symmetrically about 36 mm from the axis, so that the measurement temperature can be taken as the mean value of probe A and B, namely $\overline{T} \equiv (T_A + T_B)/2$. Let the temperature difference be defined by $\Delta T \equiv T_A - T_B$.

The parallelity adjustment screws **5** enable angular adjustment of the upper transducer; the cable feedthrough connector **6** leads the electrical signals through the cell top lid; the humidity sensor **7** gives a measurement of the relative humidity. Three gas inlet **9** and outlet **10** ports, placed diametrically opposite to eachother, are distributed along the wall to yield homogeneous flushing and prevent gas trapping in inaccessible cavities of the cell.

Ultrasonic transducers and holders

The mas transducer [29, 15] was primarily chosen due to its narrow total beam angle of 10° (-3 dB), which is advantageous to minimize diffraction correction. Also, it has a relatively broad bandwidth of 25 kHz, which is advantageous to minimize the transient regime of the burst pulse. The sound field produced and further details on the transducer may be found in [15]. The effective source radius a_{eff} was estimated [5] to 4.25 mm at the operating frequency, 218 kHz, and the outer front face radius a_{fr} is 6 mm [15].

The transducer holders **2** (cf. Fig. 8.3) were, to reduce their influence upon reflection, designed so as to minimize the surrounding transducer area. A conical design was chosen, yielding a ring of width 0.3 mm around the transducer front face. There is a circular gap of width 1 mm between the transducer front and holder, which was filled with cotton to dampen possible echoes from this gap.

Of reasons given in Sec. 8.3.4, the transducer was suspended in the holder by one o-ring, which is unfortunate with respect to angular alignment. To optimize the alignment, the transducer was immersed into the holder by pushing it backwards through the o-ring with

a plane object, until the object was obstructed by the front of the holder. To prevent that the o-ring, which is quite resilient, recoiled the transducer out of position, the o-ring was lubricated with grease. The skewness of the transducer fronts are estimated to be no worse than $\lambda/10$, which is assumed to give negligible error in Δt.

Another issue with the present transducer was its rather soft front layer, which is somewhat unfortunate with respect to planarity, and compression upon measurement using the micrometer, cf. Sec. 8.3.2.

Measurement system

A functional diagram of the measurement system, whose model was outlined in Fig. 8.2, is shown in Fig. 8.4. The components of the system are briefly described below.

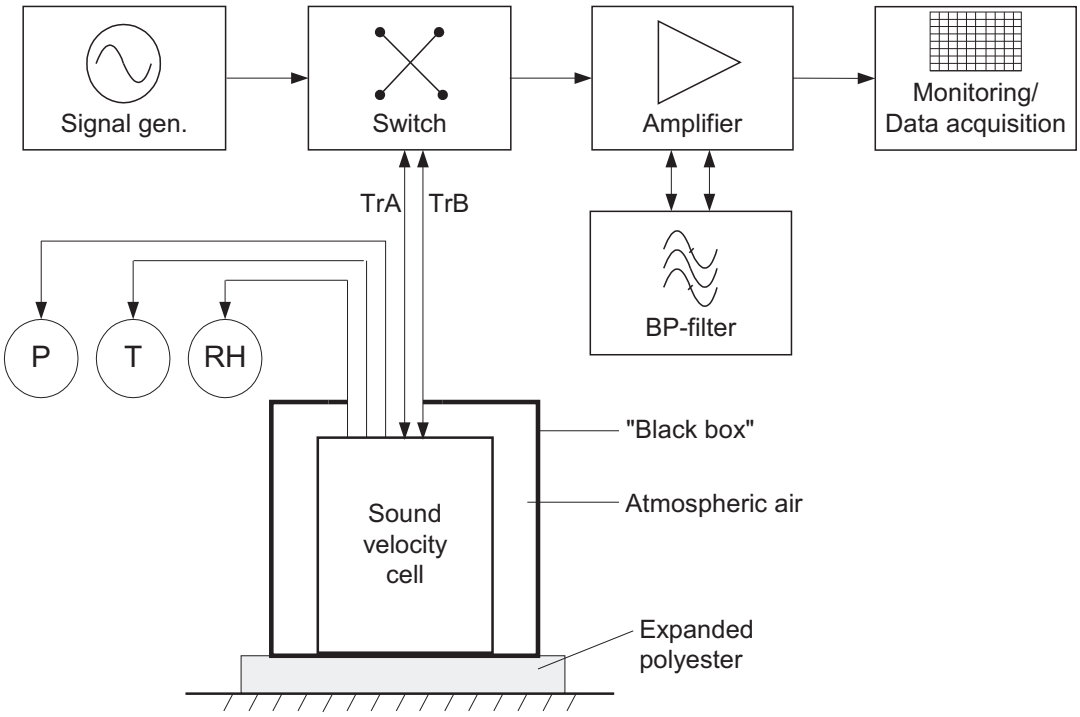

Figure 8.4: Functional diagram of the measurement system.

The signal generator was of type *HP33120A*, set with a burst carrier frequency of 218 kHz, 35 burst periods and repetition rate 30 Hz. The switch circuit was custom design [11],

based on analog swiches of type *Analog Devices ADG453*, providing swiching times below 70 ns, and on-resistance below 4 Ω. The amplifier of type *Brüel & Kjær Measuring Amplifier 2610* was set with 20 dB input gain, whereas the bandpass (BP) filter, denoted *Krohn-Hite 3940*, was set in Butterworth mode with 20 dB gain and lower and upper cut-off frequencies of 80 and 330 kHz, respectively. Data acquisition was carried out using a *GageScope CS1250* PC-oscilloscope, with an estimated effective bit resolution of 8.4,[1] and a sampling frequency of 10 MHz.

The component marked 'P' represents the atmospheric pressure measurement, performed with a *Brüel & Kjær UZ0003* barometer, with an estimated measurement uncertainty of 600 Pa (95% conf. level). The component marked 'T' represents the temperature measurement (cf. Sec. 8.3.1) performed by thermocouples A and B connected to a precision thermometer, *ASL F250*. The combined measurement uncertainty of the probes and instrument is 13 mK (95% conf. level). The component marked 'RH' represents the relative humidity instrument, *Vaisala HMT330 humidity transmitter*, with a stated measurement uncertainty of 1.25% (around 27 °C; confidence level not specified).

8.3.2 Measurement procedure

The sound velocity measurements were carried out over several days using air at approximately 1010 mbar, with a temperature and relative humidity of about 27 °C and 30%, respectively. To evaluate the repeatability, *measurement series* comprising of 5 measurement points were carried out during time spans over which the temperature $\overline{T}$ was stable to within 14 mK.

The transducer separation L_0 (cf. Eq. (8.9) and Fig. 8.3) was obtained from the average value of 5 measurements of the transducer separation, taken at the center of the transducer fronts, using a micrometer screw. To avoid compression of the rather soft transducer fronts due to weight load of the micrometer, the measurement unit was lying

[1] the nominal vertical bit resolution was stated to be 12.

horizontally while measuring. The value of L_0 was (150.786 ± 0.01) mm at the reference temperature $T_0 = 297.45$ K. The uncertainty in L_0, 10 μm (95% conf. level), was obtained by incoherent combination of the two standard deviation of the measurement series with the measurement uncertainty of the micrometer screw, 8.2 μm.

The measurement of Δt and modelling of t^{corr} (cf. Eq. (8.9)) are described in Secs. 8.3.3 and 8.2.2, respectively.

8.3.3 Signal processing and time detection

Two representative measurement signals, coherently averaged from 15 burst pulses each, are shown in Fig. 8.5.
Referring to Fig. 8.5, the rectangular time windows indicate the region in which zero crossing transit times are calculated. The time windows are automatically detected using a treshold proportional to the maximum of the burst pulses.[2] The zero crossings are determined using linear interpolation between the samples points around zero.

Now, by subtracting the zero crossing times within the rectangle in ① from the corresponding in rectangle in ②, we obtain a vector of values for $t_2 - t_1$, denoted t'_{21}. The same approach is executed for ③ and ④ so as to obtain a vector of values for $t_4 - t_3$, denoted t'_{43}. By adding t'_{21} and t'_{43} we have a $\Delta t'$ vector which is illustrated in Fig. 8.6. Finally Δt is taken to be the average value of zero crossings 15 to 40 (15 refers to zero crossing no. 15 from the beginning of the rectangle) in $\Delta t'$.

8.3.4 Challenges

During the development work on the sound velocity cell, some particular challenges influencing the measurement uncertainty were encountered, 1) switching noise, 2) transducer ringing, 3) convection currents in the measurement medium and 4) non-planarity of the

[2] note that although the envelope of the bursts within the rectangles are not stationary, Δt is obtained from a stationary region.

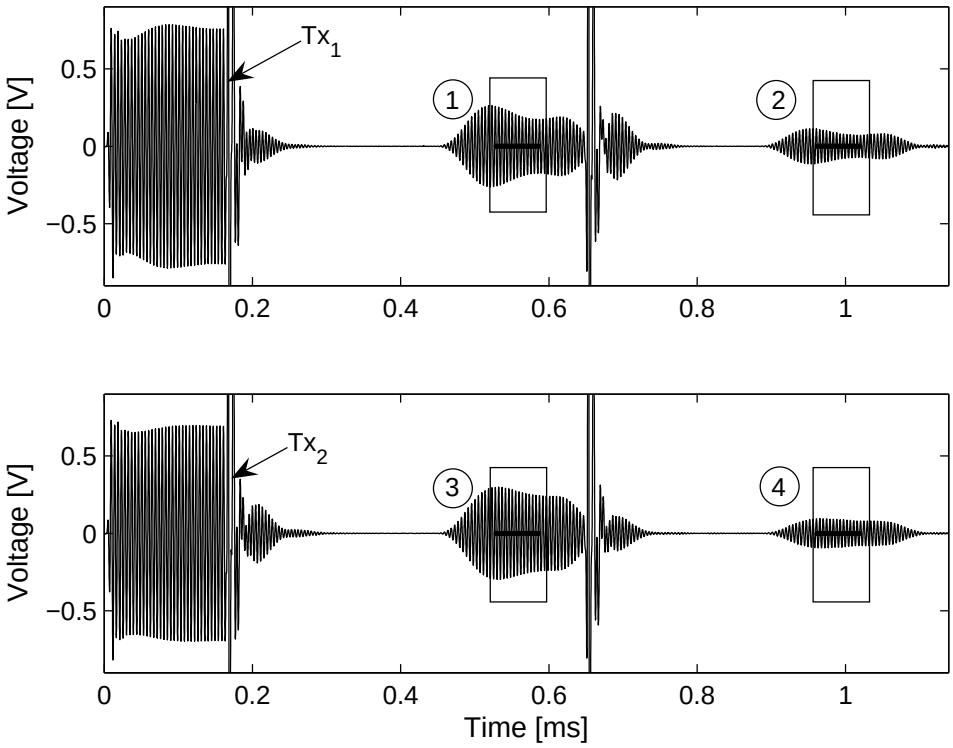

Figure 8.5: Upper subfigure shows the averaged signal trace obtained from the burst pulses launched at, say odd trig signals; lower subfigure shows the averaged signal trace obtained from the burst pulses launched at even trig signals. Tx_1 and Tx_2 denote transmitted burst signals. Note that the spikes at the trailing edges of Tx_1, Tx_2, ① and ③ are due to switching noise.

transducer front.

1. The switching of the transducer to receiving mode shortly after transmission generates a charge injection/noise spike on the signal line, cf. Fig. 8.5. Previously this noise saturated the oscilloscope, causing a bias in the transit times t_2 and t_4. The problem was omitted by modifying the electrical switching circuit, coupling shunt resistors to the transducers [11]. Also, the bandpass filters were tuned to cut the highest frequency components of the spikes, reducing their level significantly.

2. Due to the short time elapsing from the transducer acts as source until it is a receiver, transducer ringing noise interfers with the received echoes, ② and ④. In the initial version of the transducer holder, there were direct contact with the

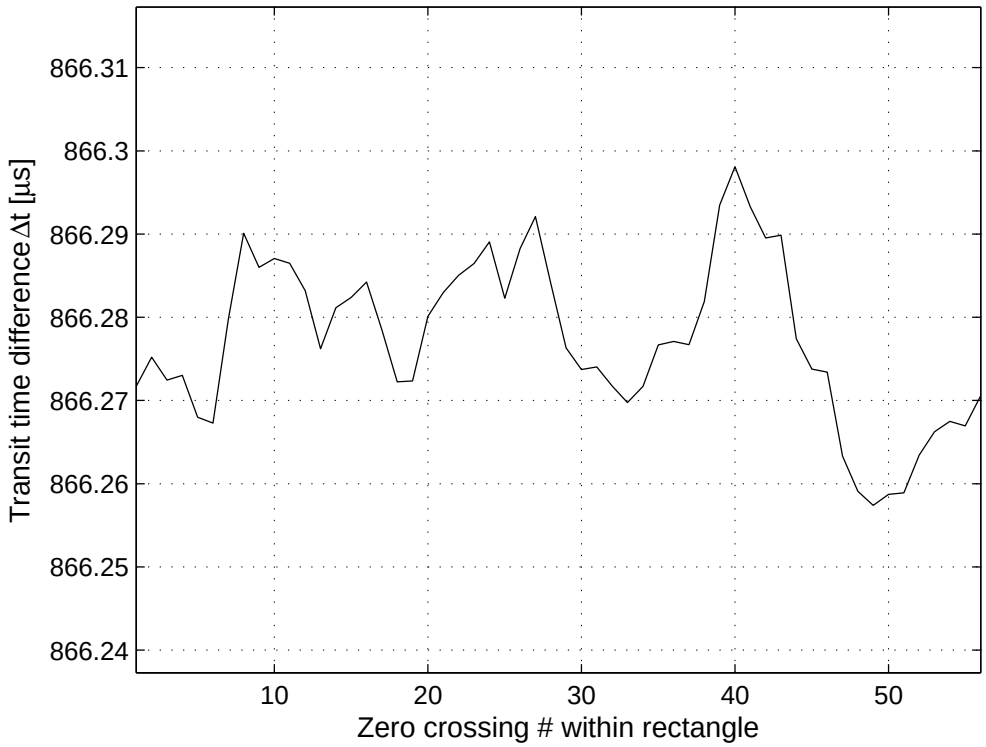

Figure 8.6: The $\Delta t'$ vector versus zero crossing number within the rectangles (Fig. 8.5). The quantity Δt is the average value of zero crossing 15 to 40, a region in which the span is typically about 20 ns, and the standard uncertainty is typically about 8 ns.

transducer, leading to relatively strong ringing effects. The associated SNR was in the worst case about 25 dB, yielding a shift in Δt of about 100 ppm. With the present holder and transducer suspension, the corresponding worst case SNR was about 34 dB, yielding a transit time shift of about 15 ns (per echo), which is about 35 ppm relative to Δt. This effect may presumably be reduced, using a transducer with a broader bandwidth.

3. The transducer separation L_0 is measured from center to center of the transducer fronts. Since non-planarity may be significant across of the transducer fronts (cf. Sec. 8.3.2), the uncertainty in L_0 may be underestimated. Moreover, this may cause undesired phase shift of the echoes upon reflection.

4. Medium convection currents may disturb the transit time considerably [8, 30]. Pre-

vious sound velocity measurements using the present measurement unit immersed in a measurement chamber [8], resulted in a spread of the measured sound velocity relative to the model of about 500 ppm. To minimize such effects, measurements were not conducted if ΔT was greater than 40 mK.[3] The present result spread is however still significant, amounting to about 200 ppm, cf. Sec. 8.5.

8.4 Results

8.4.1 Sound velocity

The sound velocity measurement results are outlined in Table 8.2, including temperature, relative humidity and sound velocity model predictions. The sound velocity results relative to the model are also plotted in Fig. 8.7.

Firstly, it is seen that the measurement repeatability is very good for each series, as the maximum two standard deviation spread relative to the model amounts to only 17 ppm (series #3). Secondly, the model deviation varies relatively much between the series—a phenomenon that will be adressed in Sec. 8.5. Thirdly, all measurement results are well within the tentative model uncertainty of at least 300 ppm [25], with a mean deviation of -57 ppm.

8.4.2 Experimental uncertainty

The relative experimental uncertainty was estimated according to [31], and calculated by

$$\frac{U(c)}{c} \approx 2\sqrt{\left(\frac{u(K_T)}{K_T}\right)^2 + \left(\frac{u(L_0)}{L_0}\right)^2 + \left(\frac{u(\Delta t)}{\Delta t}\right)^2 + \left(\frac{u(t^{corr})}{\Delta t}\right)^2}, \qquad (8.18)$$

where $u(\bullet)$ denotes standard uncertainty of the respective quantity and $U(c)$ denotes the expanded uncertainty of c ($k = 2$), cf. Table 8.3. Equation (8.18) states that the quantities in Eq. (8.9) are assumed to be uncorrelated, which represents a worst case scenario.

[3] to prevent possible heating from the thermocouples (contributing with only 0.1 mW each), they were turned off whenever possible.

Table 8.2: The sound velocity measurement and model (abbreviated *mod.*) results, obtained for air at about 1010 mbar, with $\overline{T}$ and RH about 27 °C and 30%, respectively.

Series #	Meas. #	$\overline{T}$ [°C]	RH%	Meas. c [m/s]	Mod. c [m/s]	Dev. [ppm]
1	1	25.882	30.4	347.484	347.479	15
	2	25.8805	30.4	347.486	347.478	23
	3	25.8805	30.4	347.487	347.478	25
	4	25.8795	30.4	347.488	347.478	30
	5	25.8805	30.4	347.488	347.478	29
2	6	27.701	29.9	348.540	348.593	-151
	7	27.6995	30	348.541	348.594	-152
	8	27.6985	29.9	348.539	348.591	-151
	9	27.696	29.9	348.538	348.590	-148
	10	27.6935	29.9	348.537	348.588	-148
3	11	27.718	31.7	348.572	348.632	-172
	12	27.712	31.7	348.571	348.628	-164
	13	27.709	31.7	348.571	348.627	-159
	14	27.7075	31.7	348.570	348.626	-159
	15	27.7045	31.7	348.570	348.624	-155
4	16	27.0215	31.5	348.197	348.203	-19
	17	27.02	31.5	348.195	348.202	-21
	18	27.019	31.5	348.195	348.202	-20
	19	27.0185	31.5	348.193	348.201	-24
	20	27.02	31.5	348.192	348.202	-28
5	21	25.9305	31.8	347.553	347.544	24
	22	25.9295	31.8	347.550	347.544	17
	23	25.9275	31.8	347.552	347.542	28
	24	25.929	31.8	347.552	347.543	25
	25	25.9295	31.8	347.550	347.544	20

The experimental uncertainty budget given in Table 8.3, is due to reasons given below regarded as preliminary.

Referring to Table 8.3, the uncertainty of K_T is so small and insignificant due to the

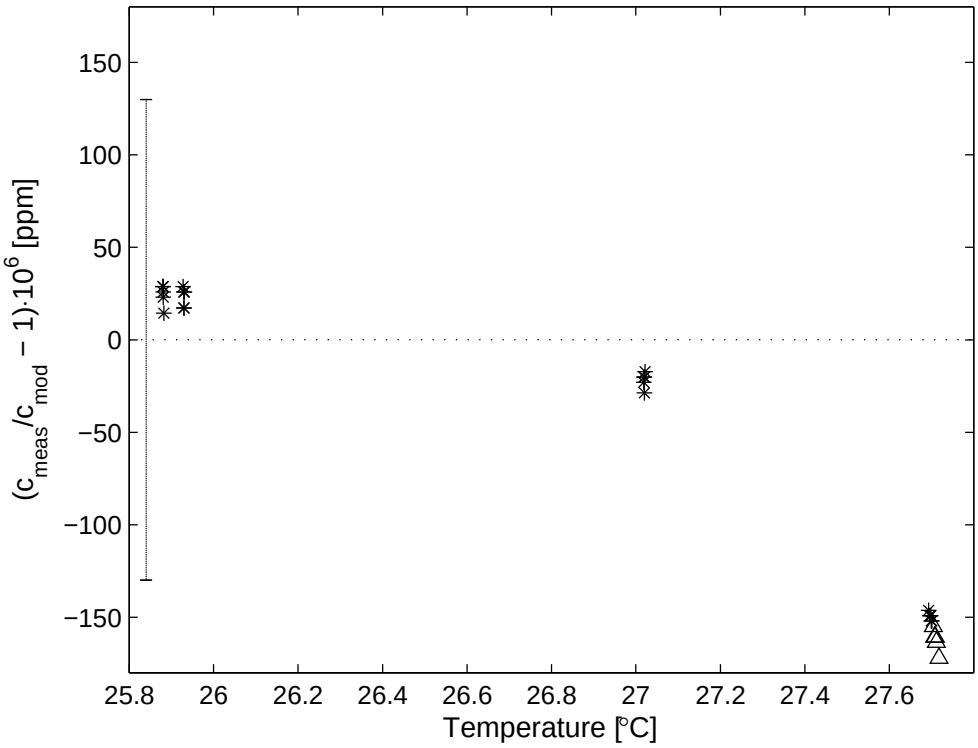

Figure 8.7: Sound velocity measurement results relative to the model. The horizontal and vertical part of the error bar (shown to the left) indicate the measurement uncertainty in temperature and sound velocity, respectively. The '△' symbol refers to series 3, and serves simply to distinguish series 2 and 3. Notice the good measurement repeatability for all series.

present relatively narrow temperature range.

The uncertainty in L_0 of about 10 μm is dominated by the uncertainty of the micrometer screw, stated by the manufacturer to 8.2 μm, cf. [32, Eq. (8.2.1)]. Possible non-planarity of the transducer front is not accounted for here, moreover, the resilient transducer front may give an excessive measured value of L_0, as the micrometer screw to some extent compresses the transducer front upon measurement. Hence, $u(L_0)/L_0$ in Table 8.3 must be regarded as a preliminary estimate.

The standard uncertainty of Δt, $u(\Delta t)$, is by far dominated by effects of medium convec-

Table 8.3: Preliminary experimental uncertainty budget.

Relative standard uncertainty	Value [ppm]
$u(K_T)/K_T$	1
$u(L_0)/L_0$	36
$u(\Delta t)/\Delta t$	54
$u(t^{corr})/\Delta t$	-
Relative combined standard uncertainty, $u(c)/c$	65
Relative expanded uncertainty, $U(c)/c$ (95% conf. level)	130

tion currents, cf. Sec. 8.3.4. Their contribution to $u(\Delta t)$ was estimated in the following way. It is assumed that the sound velocity deviation from the model would be approximately constant if convection currents were absent, as the temperature, relative humidity and pressure ranges are relatively narrow. Thus, the contribution due to convection currents may be estimated directly from the span of the deviation from the model; assuming that the span of 202 ppm represents 95% confidence level (cf. Fig. 8.7), the standard uncertainty contribution of c will be $202/4 = 50.5$ ppm, corresponding to an uncertainty contribution of 45 ns relative to Δt. Further arguments that these variations are due to temperature induced convection currents are given in Sec. 8.5. As mentioned in Sec. 8.3.4, transducer ringing disturbed the signals significantly, i.e. with about 15 ns perturbation in Δt. This is however a negligible contribution relative to the convection current effects. The uncertainty in the transit time detection method has been estimated elsewhere [9, 11], and found to be of insignificant importance.

The uncertainty in t^{corr} is presumably predominated by the uncertainty in diffraction correction, as the influence of thermo-viscous boundary layer correction relative to diffraction correction is only 0.4%. The quantity $u(t^{corr})$ is unfortunately highly challenging to estimate properly, and is therefore omitted in the present uncertainty budget. As an example of its influence, $u(t^{corr})/t^{corr}$ becomes predominant in the uncertainty budget at a level of about 5% (i.e. for $u(t^{corr}) \approx 80$ ns), which illustrates the major impact of t^{corr}.

8.5 Discussion

In Sec. 8.4.1, good agreement between measured and modeled sound velocity was demonstrated. We must however bear in mind the significant uncertainty of the sound velocity model of at least ±300 ppm [25]. Moreover, alternative models exist [99], predicting a sound velocity that deviates by about 515 ppm from the model used here.

The estimated experimental uncertainty of 130 ppm (95% conf. level) should be regarded as preliminary, due to the tentative estimate of the uncertainty in L_0 and the omission of the uncertainty in t^{corr}. Also, effects of angular misalignment and non-planarity of the transducer fronts may contribute (cf. Sec. 8.3.1), and have unfortunately not been accounted for. Nonetheless, the experimental uncertainty budget is valuable for comparing the importance of the uncertainty contributions relative to eachother.

As emerging from Fig. 8.7 there is a significantly varying deviation from the model between the measurement series. It was noted in Sec. 8.3.4 that convection currents disturb the measurements of Δt relatively much. Now each measurement series is taken at different time of day, so the temperature conditions will vary.

We now define $\overline{T}_{5m-4}$ and $\overline{T}_{5m}$ as the first and fifth measurement temperature of corresponding measurement series $m = 1, \ldots, 5$, respectively. Consider Fig. 8.8 which outlines the *mean deviation* from the model for each measurement series vs. change in temperature, $(\overline{T}_{5m} - \overline{T}_{5m-4})$.[4] A very high correlation of 0.996 is found between the mean deviation from the sound velocity model and change in temperature over the series, leaving little doubt that the cause of this spread is convection currents in the medium. This underlines the importance of stabilizing the temperature and avoiding temperature gradients across the cell body.

[4] taking this difference is reasonable, because the temperature basically changes monotonically over each measurement series.

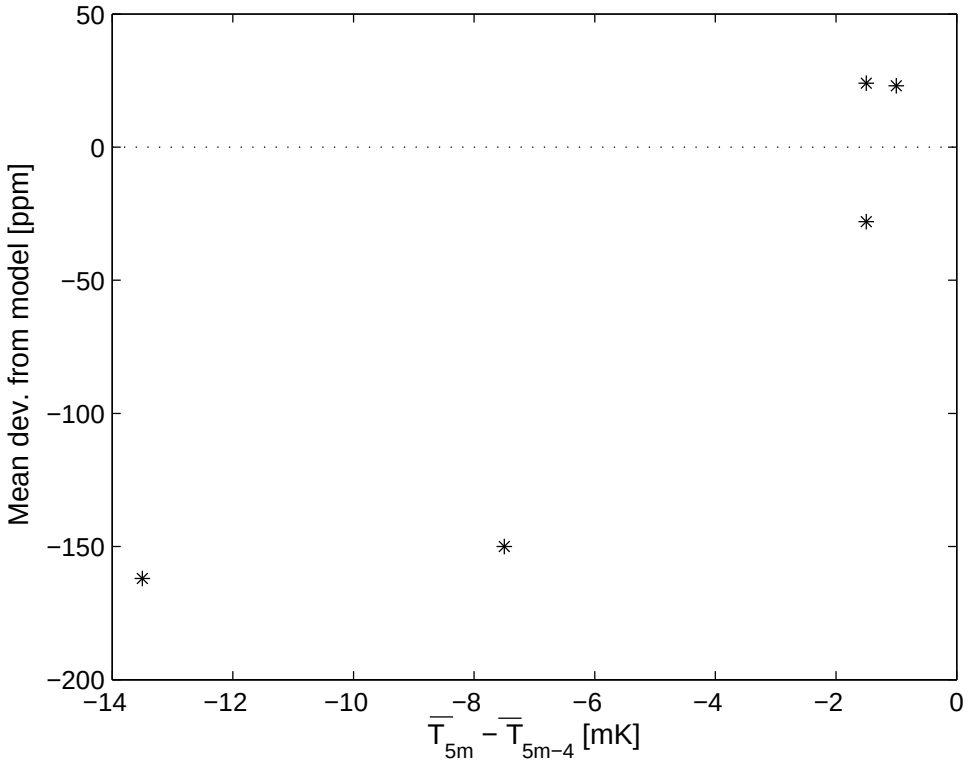

Figure 8.8: Mean sound velocity deviation from the model versus change in temperature for the five measurement series.

It was noted in Sec. 8.3.4 that previous sound velocity measurements performed using the measurement unit immersed in a measurement chamber [9] of much greater volume and temperature differences (ΔT) than in the present cell, the sound velocity result spread was more than twofold the present. Convection currents should be further reduced by immersing the sound velocity cell into a properly regulated thermostat liquid with stirrer.

8.6 Conclusions and perspectives

The 2PEM method has been investigated experimentally with respect to its potential for realization in a high-precision sound velocity cell for natural gas at high pressures. Atmospheric air at room temperature was used as test gas, and sound velocity measurement results have been compared with output from a sound velocity model. A preliminary

measurement uncertainty budget was given.

The results indicate that the 2PEM may be promising with respect to achieve a measurement uncertainty in line with the target specifications of the sound velocity cell, 100 – 200 ppm, in the frequency range of USMs, 100 – 200 kHz. It is expected that immersing the cell in a temperature regulated liquid bath will reduce the temperature induced convection currents significantly, and thus reduce the measurement uncertainty accordingly. Moreover, the uncertainty in the time correction should be properly established, so as to enable a better estimate of the experimental uncertainty of the 2PEM. Further work is desirable to attain traceability in the experimental uncertainty, using a more well suited test gas such as e.g. argon.

Acknowledgments

The present work is done as a part of a PhD fellowship for the author under the 4-year strategic institute programme "Ultrasonic technology for improved exploitation of petroleum resources" (2003-2006), supported by The Research Council of Norway (NFR), Statoil ASA and Gassco AS, and carried out in a cooperation between CMR and the University of Bergen (UiB), Dept. of Physics and Technology.

Reidar Bø with CMR is greatfully acknowledged for designing and manufacturing the switching circuit, Stig Heggstad with CMR is acknowledged for designing the prototype measurement cell, and the supervisors, Magne Vestrheim (UiB) and Per Lunde (CMR), are acknowledged for fruitful inputs and discussions concerning the present paper.

Bibliography

[1] K.-E. Frøysa and P. Lunde, "Density and calorific value measurement in natural gas using ultrasonic flow meters," in *Proc. 23rd International North Sea Flow Measurement Workshop*, Tønsberg, Norway, Oct. 2005.

[2] K.-E. Frøysa, P. Lunde, A. Paulsen, and E. Jacobsen, "Density and calorific value measurement in natural gas using ultrasonic flow meters. Results from testing on various north sea gas field data," in *Proc.* 24^{th} *International North Sea Flow Measurement Workshop*, St. Andrews, Scotland, Oct. 2006.

[3] P. Lunde and K.-E. Frøysa, "Mass and energy measurement of gas using ultrasonic flow meters," in *Proc.* 25^{th} *Scandinavian Symposium on Physical Acoustics*, Ustaoset, Norway, Jan. 2002.

[4] P. Lunde and M. Vestrheim, "Precision sound velocity cell for natural gas at high pressures. Phase 1—feasibility study," Christian Michelsen Research AS, Bergen, Norway, Tech. Rep. CMR-98-F10039 (Confidential), Dec. 1998.

[5] P. Norli, P. Lunde, and M. Vestrheim, "Methods for precision sound velocity measurements in pressure cells for gas characterization," in *Proc.* 27^{th} *Scandinavian Symposium on Physical Acoustics*, Ustaoset, Norway, Jan. 2004, CD issue only, ISBN: 82-8123-000-2.

[6] M. R. Moldover, J. P. M. Trusler, T. J. Edwards, J. B. Mehl, and R. S. Davis, "Measurement of the universal gas constant R using a spherical acoustic resonator," *J. Res. Natl. Bur. Stand.*, vol. 93, pp. 85 – 144, 1988.

[7] Y. Hanayama, "Velocity of ultrasound wave in mixed gases at high pressures," *J. Phys. Soc. Japan*, vol. 46, pp. 328 – 333, 1979.

[8] P. Norli, "Comparison of three methods for precision sound velocity measurement of gases," in *Proc.* 28^{th} *Scandinavian Symposium on Physical Acoustics, Ustaoset, Norway*, Ustaoset, Norway, Jan. 2005, CD issue only, ISBN: 82-8123-000-2.

[9] P. Norli, P. Lunde, and M. Vestrheim, "Investigation of precision sound velocity measurement methods as reference for ultrasonic gas flow meters," in *Proc. 2005 IEEE International Ultrasonics Symposium*, Rotterdam, The Netherlands, Sept. 2005, pp. 1443 – 1447.

[10] P. Norli and P. Lunde, "A three-way pulse method for a precision sound velocity measurement cell," in *Proc. 2006 IEEE International Ultrasonics Symposium*, Vancouver, Canada, Oct. 2006.

[11] P. Norli, "Sound velocity cell for gas characterization," Ph.D. dissertation, University of Bergen, Dept. of Physics and technology, Bergen, Norway, 2007, in preparation.

[12] H. Suzuki, H. Tanaka, and H. Hachisuka, "Method and apparatus for ultrasonic wave measurement," US Patent No. 6.094.987, Aug. 2000.

[13] M. L. Sanderson and A. R. Guilbert, "Acoustic measurement of fluid properties," UK Patent No. 2.321.705, Aug. 1998.

[14] R. Wilhelmsen and J. Aashamar, *Tekniske regnetabeller*, 3rd ed. Norway: Cappelen, 1977.

[15] P. Norli and P. Lunde, "Diffraction correction for a piezoelectric ultrasonic gas transducer using finite element modelling, ," 2007, manuscript to be submitted to a peer refereed journal.

[16] (2006, Sept.) Massa Corp., USA: Fundamentals of electroacoustics. [Online]. Available: http://www.massa.com/fundamentals.htm

[17] A. O. Williams, "The piston source at high frequencies," *J. Acoust. Soc. Am.*, vol. 23, pp. 1 – 6, 1951.

[18] A. S. Khimunin, "Numerical calculation of the diffraction corrections for the precise measurement of ultrasound absorption," *Acustica*, vol. 27, pp. 173 – 181, 1972.

[19] ——, "Numerical calculation of the diffraction corrections for the precise measurement of ultrasound phase velocity," *Acustica*, vol. 32, pp. 192 – 200, 1975.

[20] P. Lunde, R. A. Kippersund, M. Vestrheim, and K.-E. Frøysa, "Finite element modelling of diffraction correction for non-uniformly vibrating piezoelectric ultrasonic transducers„" Manuscript to be submitted to a peer refereed journal.

[21] ——, "Transient diffraction effects in piezoelectric ultrasonic transducers using finite element modelling," in *Proc.* 27^{th} *Scandinavian Symposium on Physical Acoustics*, Ustaoset, Norway, Jan. 2004, CD issue only, ISBN: 82-8123-000-2.

[22] J. Krautkrämer and H. Krautkrämer, *Ultrasonic testing of materials*, 2nd ed. Berlin, Germany: Springer-Verlag, 1977.

[23] A. D. Pierce, *Acoustics. An introduction to its physical principles and applications.* USA: McGraw-Hill, 1981.

[24] J. P. M. Trusler, *Physical Acoustics and Metrology of Fluids.* Bristol, England: Adam Hilger, 1991.

[25] O. Cramer, "The variation of the specific heat ratio and the speed of sound in air with the temperature, pressure, humidity and CO_2 concentration," *J. Acoust. Soc. Am.*, vol. 93, pp. 2510 – 2516, 1993.

[26] G. S. K. Wong, "Speed of sound in standard air," *J. Acoust. Soc. Amer.*, vol. 79, pp. 1359 – 1366, 1986.

[27] (2006, June) National oceanic and atmospheric administration. [Online]. Available: http://www.cmdl.noaa.gov/ccgg/trends/

[28] G. P. Howell and C. L. Morfey, "Frequency dependence of the speed of sound in air," *J. Acoust. Soc. Amer.*, vol. 82, pp. 375 – 377, 1987.

[29] (2006, Jan.) Massa E-188/220 transducers. ÍMassa Corporation, USA. [Online]. Available: http://www.massa.com/datasheets/e188.html

[30] S. Vervik, "Methods for characterization of gas–coupled ultrasonic sender-receiver measurement systems," Dr. Scient thesis, University of Bergen, Dept. of Physics, Bergen, Norway, 2000.

[31] "Guide to the expression of uncertainty in measurement," 1st Edition, International Organization for Standardization, Geneva, Switzerland, 1995, ISBN: 92-67-10188-9.

[32] S. Vervik, "Transitt–tidsbestemmelse for ultralyd strømningsmetre. Nullstrømningsforhold," Cand. Scient. thesis, University of Bergen, Dept. of Physics, Bergen, Norway, 1995, (In norwegian).

[33] G. S. K. Wong, "Variation of the speed of sound in air with humidity and temperature," *J. Acoust. Soc. Amer.*, vol. 77, pp. 1710 – 1712, 1985.

Chapter 9

Paper D

A three-way pulse method for a precision sound velocity measurement cell

Authors:

Petter Norli and Per Lunde

Reformatted version of the paper originally published in:

Proceedings of the 2006 IEEE Ultrasonics symposium, Vancouver, Canada, October 3 – 6, 2006, pp. 884 – 889.[1]

[1] In Sec. 9.2.2 below, it is stated that "A more rigorous diffraction correction approach is described in [17] ..." [i.e. in this thesis]. This is however not the case, as limited utility emerged from such an elaboration.

Abstract

Ultrasonic gas flow meters for volumetric flow rate fiscal metering of natural gas (USMs) may possibly also be used for mass and energy flow rate measurement, partially based on sound velocity measurement. To establish the accuracy of the sound velocity measurements given by the USM, and for traceability purposes, an independent high-accuracy sound velocity measurement cell may serve as reference. To include dispersion effects, the cell should preferably work in the operational frequency range of USMs, i.e. 100 – 200 kHz, with natural gas under high pressure. Highly accurate sound velocity cells are available in the audio frequency range, however, less work have demonstrated sufficient accuracy in the 100 – 200 kHz range.

Three transient methods are investigated as part of the sound velocity cell development [Proc. 2005 IEEE Ultrasonics Symposium, pp. 1443-1447, 2005]; the methods are seen to have several common sources of experimental uncertainty. In the present work, a three-way pulse method (3PM) is considered as a candidate for the sound velocity cell, and sound velocity results obtained in a prototype cell, containing air at about 1 atm and 27 °C are presented.

The results are compared with output from a sound velocity model for air, including dispersion [J. Acoust. Soc. Amer. 93 (5), pp. 2510-2516, 1993]. The results indicate that the 3PM may have potentials to perform in line with the target specifications of the sound velocity cell, i.e. 100-200 ppm, in the frequency range of USMs, 100-200 kHz. Use of a temperature regulated bath is expected to significantly reduce the temperature induced convection flows presently limiting the accuracy of the cell, and to reduce the measurement uncertainty accordingly.

9.1 Introduction

Multipath ultrasonic transit time flow meters (USMs) are today extensively used in industry for volumetric flow metering of natural gas, for fiscal measurement (e.g. sales and allocation metering), check metering, etc. As natural gas is typically sold on basis of mass or energy, the density and/or gross calorific value (GCV) of the gas is measured in addition, by separate instruments [1].

As USMs also give a measurement of the sound velocity in the gas, there is an increasing interest in exploiting the potentials of USMs for direct mass and energy measurement, using their volumetric flow rate measurement in combination with their measured sound velocity [1].

For such applications, documentation is needed for the uncertainty of the sound velocity given by the USM [2]. Provided traceable measurements can be done, this may be achieved by using a self-standing high precision sound velocity cell, working under the same conditions as the USM, and in the same frequency range, 100 – 200 kHz (to account for dispersion effects) [2].

Tentative technical cell specifications were put forward in [2]: natural gas at pressures in the range 0 – 250 barg, temperatures in the range 0 to 60 °C, and sound velocity measurement uncertainty in the range $\pm(0.05 - 0.1)$ m/s, i.e. about (100 – 200 ppm) at a 95 % confidence level.

As of today, no such cell with sufficient accuracy operating in this frequency range has been identified in the literature. Cells with outstanding accuracy are available in the audio frequency range (cf. e.g. [3]), but scaling of such existing cells to the desired frequency band and still meeting the specifications has not been considered feasible [2]. Alternative measurement methods and cells have therefore been considered [2, 4, 5, 6, 7].

Three transient methods have been investigated, aiming to realize the sound velocity cell [4, 5, 6, 7], of which two are considered possible candidates: *The two-way pulse echo method* [7], and the present *three-way pulse method* (3PM), proposed in [2]. A similar method for measurements on solids was described in 1958 [8], claiming that the sound velocity may be determined to within 100 ppm. More recently (2004), a similar method, also intended for solids, was presented [9], differing from the present by having buffer rods between the acoustic transducers and the measurement medium.

The present paper describes the 3PM and investigates its potential for precision sound velocity measurements in gas. Theory and experimental details for a prototype measurement cell for low pressures are given. Sound velocity measurement results are presented and compared with a theoretical model, using atmospheric air as measurement medium.

9.2 Theory

The theory briefly described in Secs. 9.2.1 and 9.2.2 is based on [2], and extended in Sec. 9.2.2.

9.2.1 The three-way pulse method

Consider the measurement principle of the 3PM, illustrated in Fig. 9.1. A pulse ① is transmitted from the acoustic source to the acoustic receiver, and the associated transit time t_1 is measured. A part of ① is reflected at the receiver front, giving rise to echo ② which travels back to the source—being partly reflected again—travelling forth to be received, and the associated transit time t_2 is measured.

Under the assumption that the medium is stationary over the measurement period (30 averaged signal traces, lasting about 1 sec.) the two measured transit times are written as (cf. Fig. 9.2)

$$t_i = t_T^{eltr} + t_{i,pl}^{gas} + t_i^{corr} + t_R^{eltr}, \quad i = \{1, 2\}\,, \tag{9.1}$$

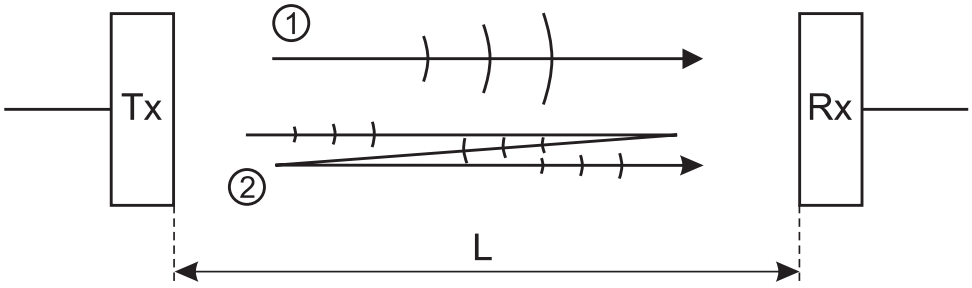

Figure 9.1: The acoustical measurement principle of the 3PM. Tx and Rx denote the transmitting and receiving transducers, respectively, and L is the transducer separation.

where t_T^{eltr} denotes the voltage-to-plane-wave pressure travel time in the transmitting electronics, cable and transducer; $t_{i,pl}^{gas}$ denotes the pressure-to-pressure plane-wave travel time in the gas; t_i^{corr} accounts for non-ideal effects such as non-plane wave propagation, i.e. diffraction time shift, t_i^{dif}, and other possible contributions (cf. Sec. 9.2.2); and t_R^{eltr} denotes the free-field averaged pressure-to-voltage travel time in the receiving transducer, electronics and cable [2].

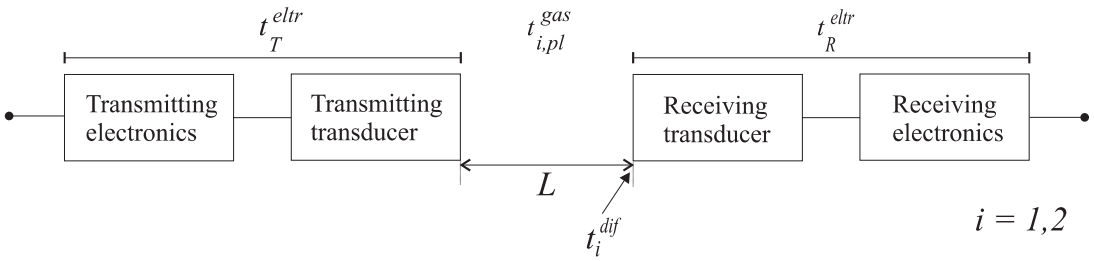

Figure 9.2: The time delay model of the measurement system. Subscript $i = 1, 2$ denotes respective pulse, ① and ②.

By inserting $t_{1,pl}^{gas} \equiv L/c$ and $t_{2,pl}^{gas} \equiv 3L/c$, where c denotes the sound velocity, and taking $t_2 - t_1$ we have

$$t_2 - t_1 = 2L/c + t_2^{corr} - t_1^{corr}, \tag{9.2}$$

or the sound velocity as [2]

$$c = \frac{2L}{\Delta t - t^{corr}}, \tag{9.3}$$

where $\Delta t \equiv t_2 - t_1$ and $t^{corr} \equiv t_2^{corr} - t_1^{corr}$. Note that the simplifying assumption that

t_R^{eltr} is equal for ① and ② has been used here, leading to a cancelling of the system delay times, t_T^{eltr} and t_R^{eltr}.

The axial transducer separation, L, is fixed to about 150 mm in the prototype measurement cell, cf. Fig. 9.3. To account for thermal expansion in L, a linear relationship has been assumed, i.e. $L = K_T L_0$ [2], where L_0 is the transducer separation, measured at a reference temperature. Here $K_T = 1 + \alpha \Delta T$, where α is the thermal expansion coefficient for the steel material [10], and ΔT is the deviation from the reference temperature in Kelvin.

9.2.2 Correction terms

Time corrections investigated in the present work are due to diffraction correction (t_i^{dif}), thermal and viscous boundary layers at the transducer fronts (t_i^{tv}), and internal transducer echoes (t_i^{int}). The correction t_i^{corr} is given as

$$t_i^{corr} = t_i^{dif} + t_i^{tv} + t_i^{int}, \quad i = 1, 2. \tag{9.4}$$

Diffraction correction

Due to diffraction effects [11], the sound waves will accumulate an increasing phase advance with distance, relative to plane waves [2]. The effect is accounted for by using the diffraction correction model [12, 13] that may be referred to as "the plane piston diffraction correction model". The present work extends the analysis in [2] by accounting for several transducer radii in the diffraction correction.

The ultrasonic transducers used here [14] consist of a piezoelectric disk with radius a_d, mechanical layers, enclosed by a metal housing. Let the outer front face radius of the transducer be denoted a_{fr}, and the effective radius, estimated from the transducer directivity, be denoted a_{eff}. It is assumed that a_{eff} is also the effective receiving radius, as the source and receiving directivity may be assumed to be reciprocal [15].

The diffraction correction for this type of transducers has been modelled and investigated [16], and it was found that for the operating frequency, $f_0 = 218$ kHz, the plane piston diffraction correction model may be used to calculate t_1^{dif} with little error. Therefore, the plane piston diffraction correction model has been used in this paper, based on some simplifications regarding t_2^{dif}. A more rigorous diffraction correction approach is described in [17], but the value found for t^{corr} in [17] coincides very well with the approximate value obtained here.

To find t_2^{dif}, the problem of diffraction correction associated with reflection from the transducer front must be resolved. By assuming that the reflecting transducer front is uniformly insonified by the incoming beam, so that all points of the reflector area can be considered elementary sources with equal phase and magnitude, the reflector may be regarded a new plane piston oscillator [18, 2]. Since the -3 dB beamwidth covers a diameter about twice the diameter of the receiving transducer, this may be a reasonable approximation.

This approach enables a decomposition of t_2^{dif} into

$$t_2^{dif} \equiv t^{dif,p} + t^{dif,eb} + t^{dif,e}, \tag{9.5}$$

where superscripts p, eb and e denote, respectively, time shift due to diffraction on reflection at receiving transducer Rx, reflection at the source transducer Tx, and reception of the reflected pulse at the receiving transducer Rx.

Now the source radii associated with $t^{dif,p}$ and t_1^{dif}, namely a_{eff}, are equal, whereas the receiver radii are slightly different. It will however be assumed that $t^{dif,p} = t_1^{dif}$, calculated using a_{eff} as radius.

A similar rationale may be applied for the source radius associated with $t^{dif,e}$, a_{fr}, which

is equal to that of $t^{dif,eb}$. Hence we assume that $t^{dif,e} = t^{dif,eb}$. Now Eq. (9.5) turns into

$$t_2^{dif} \approx t_1^{dif} + 2t^{dif,eb}. \tag{9.6}$$

As $t^{dif,eb}$ is associated with equal source and reflector radius, a_{fr}, we may calculate it using the plane piston diffraction correction model [12]. Note that $t_2^{dif} - t_1^{dif}$ is the dominating part of t^{corr}.

Boundary layer correction

When a sound wave ② is reflected at the transducer front, thermal and viscous boundary layers may be generated at the front-fluid interface, imposing a phase shift on the echo [2].

A complex reflection coefficient may account for this [19, 7], and it was evaluted for atmospheric dry air at 27 °C. A phase shift of 0.009 rad was found [17] per reflection, corresponding to $t_2^{tv} = 0.009/(2\pi f_0) = 6.5$ ns in the time domain, or about 8 ppm relative to Δt.

Internal transducer echoes

Due to the layered internal transducer structure, echoes will return from the transducer interior, and to some extent perturb the phase and magnitude of ②, and thus t_2 [2].

A one-dimensional thickness mode vibration model of the transducer has been implemented to evaluate this effect [17]; a rather high sensitivity to the front layer thickness was found, however, the magnitude was relatively small. As the front layer is not accurately known for the transducer used here, this effect was accounted for in the experimental uncertainty budget in Table 9.3, rather than being included as a correction term (cf. Sec. 9.4.2).

Obtaining t^{corr}

It is assumed that $t_1^{corr} = t_1^{dif}$. Based on Eqs. (9.4) and (9.5), we have for t_2^{corr}

$$t_2^{corr} = 2(t^{dif,eb} + t_2^{tv}) + t_1^{dif},$$

thus

$$t^{corr} = 2(t^{dif,eb} + t_2^{tv}).$$

The value of t^{corr} used in the present work is -1606 ns, or -1855 ppm relative to Δt.

9.2.3 A sound velocity model for air

A sound velocity model for humid air described in [20] has been used for comparison with the sound velocity measurements, cf. also [6]. Model input parameters are temperature, pressure, relative humidity (RH) and CO_2 concentration. Dispersion was accounted for by using [20, Eq. (14)] at the center frequency of the burst pulse, 218 kHz. Due to lack of information, the uncertainty of the dispersion model is not accounted for here. The model uncertainty is taken to be ±300 ppm (conf. level not stated) [20].[2]

9.3 Experimental

9.3.1 Measurement cell

As part of the development of the precision sound velocity cell, a prototype cell for low pressure has been devised, cf. Fig. 9.3. For brevity, it is referred to [7] for constructional considerations and details.

9.3.2 Measurement system

A signal generator of type *HP33120A* and an amplifier of type *Brüel & Kjær Measuring Amplifier 2610* were used. Bandpass (BP) filtering was done using a *Krohn-Hite 3940*

[2] In [6], the confidence level was erroneously stated to 95%.

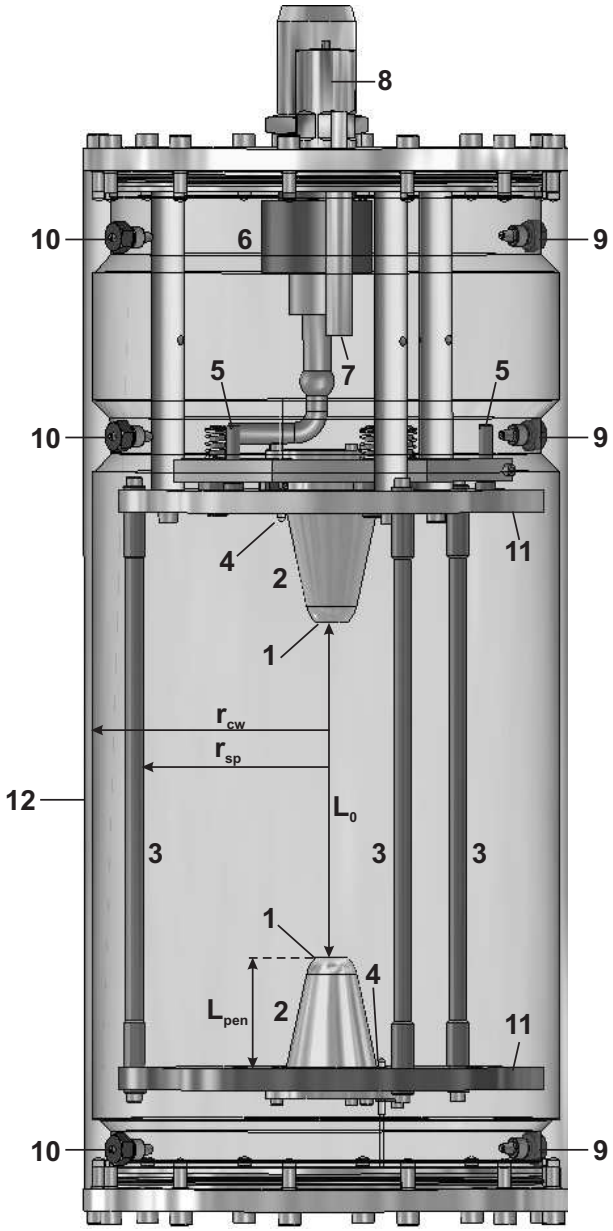

Figure 9.3: Cut-through design sketch of the prototype sound velocity cell. The numbers refer as follows. **1** ultrasonic transducers; **2** transducer holder; **3** transducer spacer rods; **4** *Pt-100* thermocouples; **5** parallelity adjustment screws; **6** cable feedthrough connector; **7** humidity sensor; **8** safety valve; **9** gas inlet ports; **10** gas outlet ports; **11** end faces, and **12** cell wall. Note that the wall was covered with a thin rugged, soft clothing (not shown) to spread and absorb possible wall echoes.

filter, and data acquisition was done with a *GageScope CS1250* PC-oscilloscope.

Temperature, pressure and RH were measured with respective uncertainties 13 mK (95%

conf. level), 600 Pa (95% conf. level) and 1.25% (conf. level not stated). The CO_2 concentration is taken to be that of outdoor air, 382 ppm [21], a value which may be somewhat low for indoor air. As an example, to illustrate the importance of this, an increase in the CO_2 concentration of, say 200 ppm, would decrease the predicted c with about 50 ppm.

As shown in Fig. 9.3, the measurement temperature is the average of the readings of probes A and B, denoted by $\overline{T} = (T_A + T_B)/2$. Let the temperature difference be denoted $\Delta T = T_A - T_B$. The most relevant system settings are given in Table 9.1.

Table 9.1: Settings of the measurement system.

Parameter	Value
Center frequency, f_0 [kHz]	218
Burst wave form	Sine
Generator peak drive level [V]	3.5
Number of burst periods	37
Burst repetition rate [Hz]	30
Sampling frequency [MHz]	10
Estimated vertical bit resolution	8.4

9.3.3 Measurement procedure

The measurement cell was surrounded by atmospheric air, enclosed by a black box. To reduce the influence of convection currents due to temperature effects, measurements were only carried out whenever ΔT was less than 40 mK. Also, to prevent possible heating from the temperature probes (contributing with 0.1 mW each), they were kept in off-mode whenever possible.

Transducer separation L_0

The transducer separation L_0 (Fig. 9.3) was measured at a reference temperature, $T_0 =$ 24.3 °C, with a micrometer screw to (150.786 ± 0.01) mm. The standard measurement uncertainty (10 μm) was obtained by combining the standard deviation of the measurement series with the measurement uncertainty of the micrometer, 8.2 μm. Possible non-planarity of the transducer front may however not have been sufficiently estimated here, hence, the uncertainty in L_0 may in practice be somewhat greater than the 10 μm used here.

Measuring Δt

For each Δt measurement, thirty burst pulses excited the source transducer within one second, which were coherently averaged to reduce noise. An example of a signal trace used for transit time detection is shown in Fig. 9.4. In practice, the zero crossings within the rectangle of pulse ① (Fig. 9.4) are subtracted from those within the rectangle of echo ② to obtain a vector of values for the transit time difference. The stationary part of this vector is then averaged to constitute Δt.

Notice in Fig. 9.4 the strong coherent noise in the beginning of the signal trace. It is most likely due to electrical cross-talk in the non-coaxial cable feedthrough of the measurement cell, as the noise was absent using coaxial cables. The worst case SNR due to the noise is about 37.5 dB, which affects Δt with a perturbation of 10 ns, or 12 ppm relative to Δt.

Another disfortunate effect of the noise, is the modulation of pulse ①, rendering difficulty in the utilization of a cross-correlation routine for determining corresponding zero crossings in ① and ②. This was therefore executed manually.

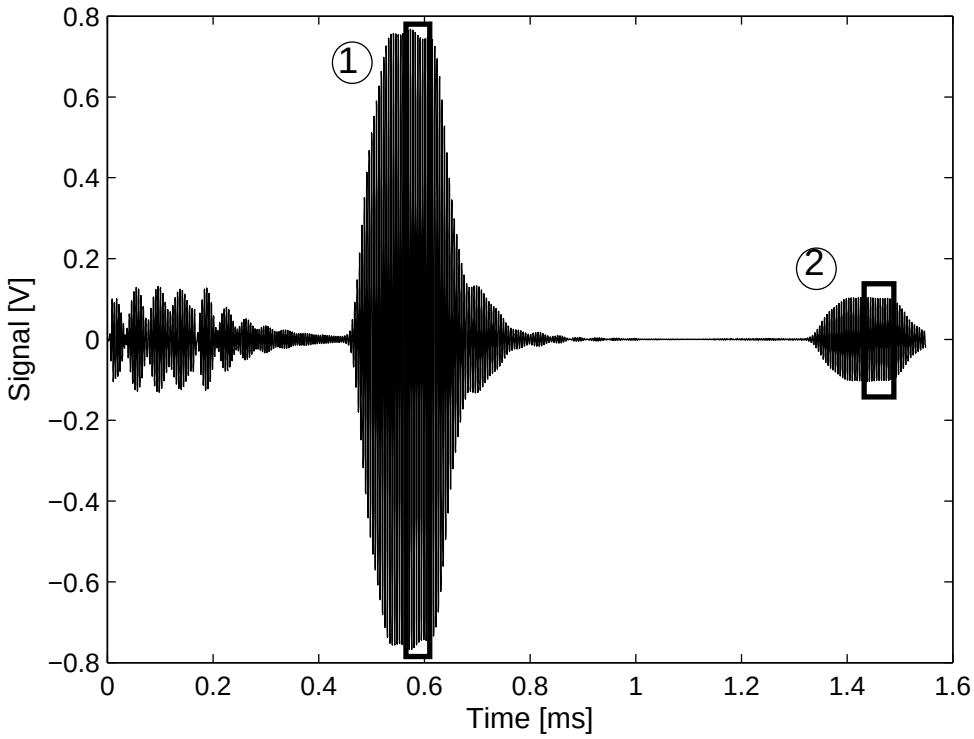

Figure 9.4: Example of an averaged signal trace. The zero crossings used for transit time detection in ① and ② are fetched from the rectangular windows.

9.4 Results

9.4.1 Sound velocity measurements

The measurement medium was atmospheric air at a pressure, temperature and RH of about 1010 mbar, 27 °C and 30%, respectively. To evaluate the measurement repeatability under approximately constant medium conditions, a measurement series was limited to a set of five measurement points, wherein the maximum change of $\delta\overline{T}$ was confined to 17 mK.

The measurement series were obtained at different times of the day, or at different days. The sound velocity results are listed in Table 9.2, and plotted in Fig. 9.5.

Table 9.2: The sound velocity results. Subscripts *ms* and *mod* abbreviate measurement and model values, respectively.

ms. #	$\overline{T}$ [°C]	RH%	c_{ms} [m/s]	c_{mod} [m/s]	Dev. [ppm]
1	25.8955	30.3	347.522	347.486	103
2	25.899	30.3	347.526	347.488	111
3	25.901	30.3	347.527	347.489	111
4	25.907	30.3	347.528	347.492	102
5	25.908	30.3	347.530	347.493	105
6	27.7295	30	348.563	348.612	-143
7	27.7245	30	348.560	348.609	-141
8	27.72	30	348.558	348.607	-139
9	27.7155	30	348.556	348.604	-138
10	27.7125	30	348.552	348.602	-144
11	27.6945	31.7	348.577	348.618	-116
12	27.688	31.7	348.576	348.614	-109
13	27.6835	31.7	348.575	348.611	-103
14	27.68	31.7	348.575	348.609	-98
15	27.021	31.5	348.220	348.203	48
16	27.0235	31.5	348.217	348.204	35
17	27.0215	31.5	348.215	348.203	33
18	27.0205	31.5	348.213	348.203	29
19	27.018	31.5	348.211	348.201	27
20	25.9325	31.8	347.572	347.546	77
21	25.932	31.8	347.573	347.545	79
22	25.9365	31.8	347.575	347.548	78
23	25.9395	31.8	347.579	347.550	83
24	25.939	31.8	347.578	347.550	83

Some comments are made on the results. Firstly, the measured sound velocity is within 144 ppm relative to the model value, with a spread of maximum 16 ppm (95% conf. level)

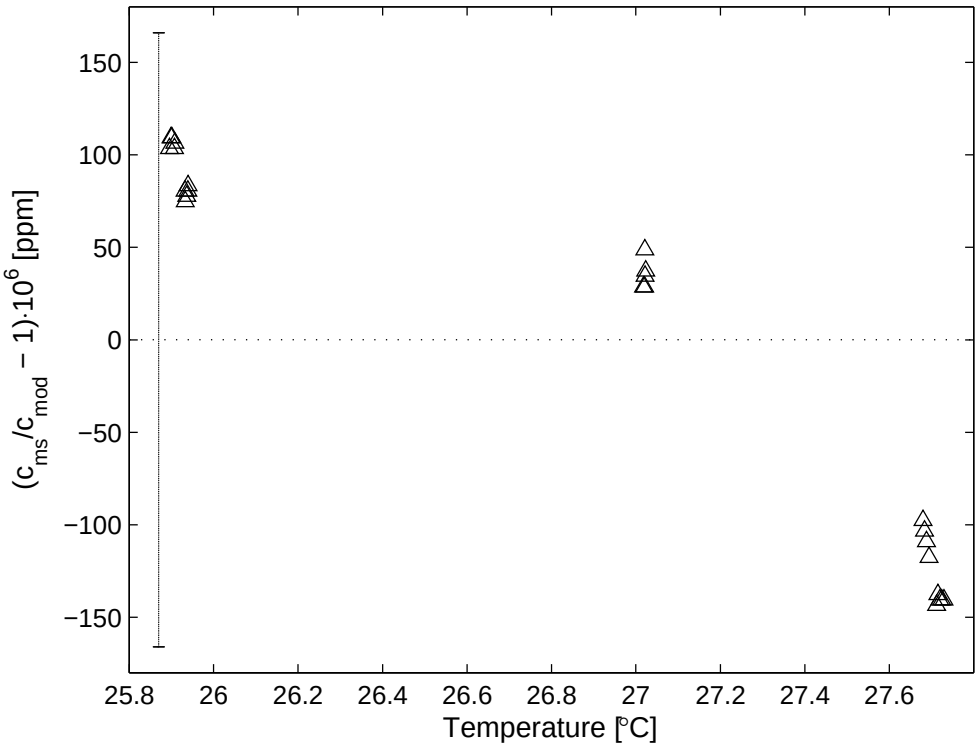

Figure 9.5: Sound velocity measurement results relative to the model. The error bar at the left indicates the measurement uncertainty in temperature (horizontal part) and sound velocity (vertical part). Notice the very good measurement repeatability for the five measurement series.

over each series. The overall mean deviation from the model is only 5 ppm; however, it must be emphasized that the model output cannot necessarily be regarded the one "true". Alternative models for air may also be relevant [22]. We notice a significant drift of the measurement results relative to the model from series to series, which cause is analyzed in Sec. 9.5.

9.4.2 Experimental uncertainty budget

The experimental uncertainty has been estimated according to guidelines described in [23]. The uncertainty contributions of Eq. (9.3) are combined as if they were uncorrelated, that is, in a square-root-sum fashion, which represents a worst case scenario. The uncertainty budget is given in Table 9.3, however, because it was not feasible to evaluate all significant

uncertainty contributions, it represents an incomplete uncertainty budget.

Notice that $u(K_T)/K_T$ makes an insignificant contribution, which is due to the narrow temperature range used. The standard uncertainty $u(L_0) \approx 10$ μm is dominated by the uncertainty of the micrometer. However, possible non-planarity of the transducer front is not accounted in this value, cf. Sec. 9.3.3.

The standard uncertainty $u(\Delta t)$ is by far dominated by effects of medium convection currents, and their contribution was estimated in the following way. It is assumed that the deviation from the model would be approximately constant if convection currents were absent. Thus, their contribution may be estimated directly from the maximum deviation from the model, taken to be 52 ppm for c, corresponding to 45 ns relative to Δt. The uncertainty in the transit time detection method has been estimated earlier [6, 17], and found to be insignificant here.

The uncertainty in t^{corr} is considered to be dominated by uncertainty in the diffraction correction, cf. Sec. 9.2.2. This uncertainty contribution is very challenging to estimate, and has thus been left out of the uncertainty budget here. However, $u(t^{corr})/t^{corr}$ would start to dominate the uncertainty budget at a level of about 5% (i.e. for $u(t^{corr}) \approx 80$ ns), which illustrates the importance of establishing the uncertainty of the diffraction correction. Other relatively weak contributions to t^{corr} were due to internal transducer reflections and electrical cross-talk, contributing with 12 and 10 ns, respectively, corresponding to about 14 and 12 ppm for c, respectively.

9.5 Discussion

The previous section demonstrated good correspondence between measured and modelled sound velocity; we must however bear in mind the uncertainty associated with the sound velocity model used for comparison (at least $\pm$300 ppm) [20], and also that alternative

Table 9.3: Experimental uncertainty budget (incomplete).

Relative standard uncertainty	Value [ppm]
$u(K_T)/K_T$	1
$u(L_0)/L_0$	36
$u(\Delta t)/\Delta t$	52
$u(t^{corr})/\Delta t$	-
Relative combined standard uncertainty, $u(c)/c$	63
Relative expanded uncertainty, $U(c)/c$ (95% conf. level)	126

methods exist [22], which deviate by about 515 ppm from the model used here.

The experimental uncertainty is estimated to 126 ppm (95% conf. level). However, due to insufficient knowledge about the planarity of the transducer front face, and the uncertainty of the diffraction correction (which is expected to dominate the budget), the experimental uncertainty budget should be regarded as somewhat preliminary, serving mainly to evaluate the relative importance of the various uncertainty contributions.

Inspecting the deviation from the model, cf. e.g. column 6, Table 9.2, a significantly varying deviation from the model is observed from series to series—an unfortunate effect that should be resolved.

As each measurement series is performed at different hours or days, the heat flux through the sound velocity cell will vary accordingly. Figure 9.6 demonstrates a very high correlation (0.996) between change in $\overline{T}$ over the measurement series, and the deviation from the sound velocity model, which is a strong indicator of convection currents set up to equalize temperature gradients in the measurement cell. Such currents may affect the transit times severely.

Also temperature gradients intrinsic in the fluid, measured by ΔT, is an important pa-

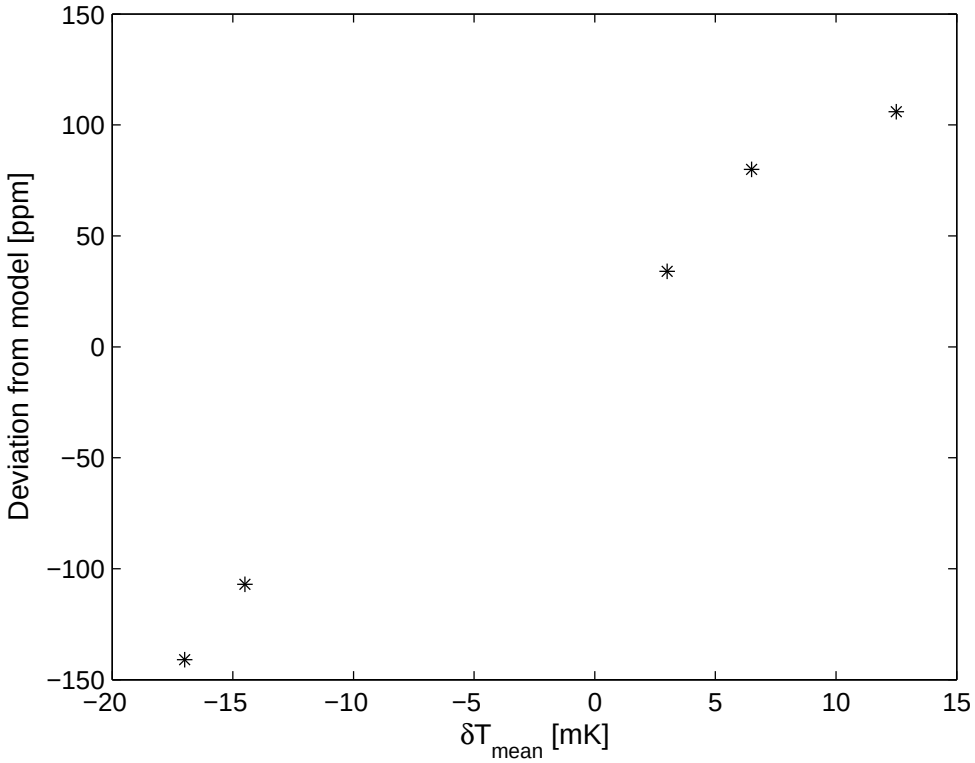

Figure 9.6: Deviation in measured sound velocity relative to the model, versus change in average temperature over the measurement series. δT_{mean} ($= \delta\overline{T}$) is the change in average temperature during a measurement series.

rameter regarding convection currents. Preliminary measurements were executed on air, using the "measurement unit" comprising parts **1** – **4** and **11** (Fig. 9.3), surrounded by an acoustically insulated chamber [6]. There, the maximum ΔT value was about twice the present value, resulting in an overall span in the deviation from the sound velocity model of about 500 ppm; nearly a factor two compared to the present value.

9.6 Conclusions and perspectives

A high-precision, traceable sound velocity measurement cell for high-pressure natural gas may serve as a useful reference cell for multipath ultrasonic flow meters used for volumetric, mass and energy flow metering of natural gas.

The potentials of the 3PM method with respect to development of such a high-precision sound velocity cell have been investigated experimentally using air at atmospheric and room temperature conditions. The measurement results are compared with predictions from a sound velocity model for air, accounting for dispersion effects, and a preliminary measurement uncertainty budget is indicated.

The results for air indicate that the 3PM method may have potentials to achieve a measurement uncertainty within the target specifications of the sound velocity cell, i.e. 100-200 ppm, in the frequency range of USMs, 100-200 kHz. Further work is required in order to enable measurements on high-pressure natural gas, argon, etc., and to achieve traceability of the cell. Use of a temperature regulated bath is expected to significantly reduce the temperature induced convection flows presently limiting the accuracy of the cell, and to reduce the measurement uncertainty accordingly.

Acknowledgment

The present work is part of a PhD project for the first author under the 4-year strategic institute programme (SIP) *Ultrasonic technology for improved exploitation of oil and gas resources* (2003 – 2006) at CMR, supported by the Research Council of Norway (NFR), Statoil ASA and Gassco AS. The SIP is carried out in cooperation with the University of Bergen, Dept. of Physics and Technology (UoB).

Magne Vestrheim with UoB and Kjell-Eivind Frøysa with CMR are acknowledged for useful discussions and advice in connection with the present work.

Bibliography

[1] K.-E. Frøysa, P. Lunde, A. Paulsen, and E. Jacobsen, "Density and calorific value measurement in natural gas using ultrasonic flow meters. results from testing on various North Sea gas field data," in *Proc.* 24^{th} *Int. North Sea Flow Measurement workshop*, Gleneagles, Scotland, Oct. 2006.

[2] P. Lunde and M. Vestrheim, "Precision sound velocity cell for natural gas at high pressures. Phase 1—feasibility study," Christian Michelsen Research AS, Bergen, Norway, Tech. Rep. CMR-98-F10039 (Confidential), Dec. 1998.

[3] M. R. Moldover, J. P. M. Trusler, T. J. Edwards, J. B. Mehl, and R. S. Davis, "Measurement of the universal gas constant R using a spherical acoustic resonator," *J. Res. Natl. Bur. Stand.*, vol. 93, pp. 85 – 144, 1988.

[4] P. Norli, P. Lunde, and M. Vestrheim, "Methods for precision sound velocity measurements in pressure cells for gas characterization," in *Proc.* 27^{th} *Scandinavian Symposium on Physical Acoustics*, Ustaoset, Norway, Jan. 2004, CD issue only, ISBN: 82-8123-000-2.

[5] P. Norli, "Comparison of three methods for precision sound velocity measurement of gases," in *Proc.* 28^{th} *Scandinavian Symposium on Physical Acoustics*, Ustaoset, Norway, Jan. 2005, CD issue only, ISBN: 82-8123-000-2.

[6] P. Norli, P. Lunde, and M. Vestrheim, "Investigation of precision sound velocity measurement methods as reference for ultrasonic gas flow meters," in *Proc. 2005*

IEEE International Ultrasonics Symposium, Rotterdam, The Netherlands, Sept. 2005, pp. 1443 – 1447.

[7] P. Norli, "The two-way pulse echo method for precision sound velocity measurement of gas," *Applied acoustics*, to be submitted.

[8] J. Williams and J. Lamb, "On the measurement of ultrasonic velocity in solids," *J. Acoust. Soc. Am.*, vol. 30, pp. 308 – 313, 1958.

[9] H. Sato, K. Ito, and Y. Aizawa, "Simultaneous velocity and attenuation measurements applicable to various solids at high pressures and temperatures up to 1200 °C," *Meas. Sci. Technol.*, vol. 15, pp. 1787 – 1793, 2004.

[10] R. Wilhelmsen and J. Aashamar, *Tekniske regnetabeller*, 3rd ed. Cappelen, 1977.

[11] M. B. Gitis and A. S. Khimunin, "Diffraction effects in ultrasonic measurements," *Soviet Physics Acoustics – USSR*, vol. 14, pp. 413 – 431, 1969.

[12] A. S. Khimunin, "Numerical calculation of the diffraction corrections for the precise measurement of ultrasound phase velocity," *Acustica*, vol. 32, pp. 192 – 200, 1975.

[13] A. O. Williams Jr., "The piston source at high frequency," *J. Acoust. Soc. Am.*, vol. 23, pp. 1 – 6, 1951.

[14] (2006, Jan.) Massa E-188/220 transducers. Massa Corporation, USA. [Online]. Available: http://www.massa.com/datasheets/e188.html

[15] (2006, Sept.) Fundamentals of elctroacoustics. Massa Corporation, USA. [Online]. Available: http://www.massa.com/fundamentals.htm

[16] P. Norli and P. Lunde, "Diffraction correction for a piezoelectric ultrasonic gas transducer using finite element modelling," *IEEE Trans. Ultrason. Ferroelect. Freq. Contr.*, 2006, to be submitted.

[17] P. Norli, "Sound velocity cell for gas characterization," Ph.D. dissertation, University of Bergen, Bergen, Norway, in preparation.

[18] J. Krautkrämer and H. Krautkrämer, *Ultrasonic testing of materials.* Springer-Verlag, 1977.

[19] A. D. Pierce, *Acoustics. An introduction to its physical principles and applications.* USA: McGraw-Hill, 1981.

[20] O. Cramer, "The variation of the specific heat ratio and the speed of sound in air with the temperature, pressure, humidity and CO_2 concentration," *J. Acoust. Soc. Am.*, vol. 93, pp. 2510 – 2516, 1993.

[21] (2006, June) National Oceanic and Atmospheric Administration, USA. [Online]. Available: http://www.cmdl.noaa.gov/ccgg/trends/

[22] G. S. K. Wong, "Variation of the speed of sound in air with humidity and temperature," *J. Acoust. Soc. Am.*, vol. 77, pp. 1710 – 1712, 1985.

[23] "Guide to the expression of uncertainty in measurement," First edition, International Organization for Standardization, Geneva, Switzerland, 1995, ISBN: 92-67-10188-9.

Appendix A

Switching circuit

The switching circuit used as part of the electronics of the 2PEM is outlined in Fig. A.1, in which analog switches of type *ADG453* [1] has been used.

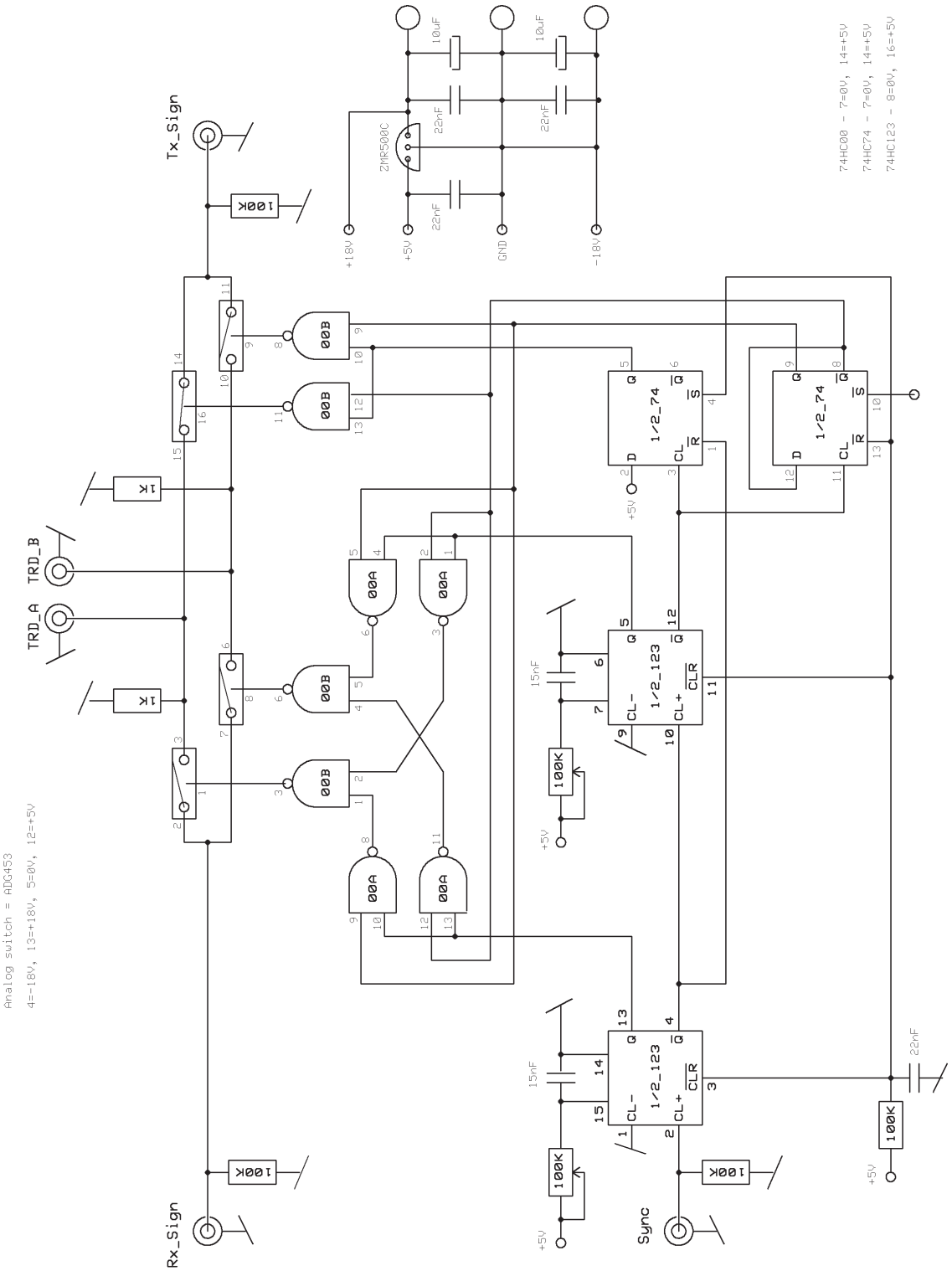

Figure A.1: The switching circuit, designed by Reidar Bø at CMR.